Modelling of Fluid Fragmentation by Molecular Dynamics

Igor A. Stepanov

Master of Philosophy

Department of Materials Science and Engineering

University of Sheffield, Sir Robert Hadfield Building

Mappin Street, Sheffield, S1 3JD, UK

January 2013

Abstract

In the present work, numerous molecular dynamics simulations of fragmentation of expanding Lennard-Jones (LJ) fluids have been performed. Two types of expansion were considered: that of Holian and Grady, and that of Blink and Hoover. Much larger systems were investigated in comparison with the previous authors (up to 0.54 million particles) and much more initial conditions. The previous authors studied systems with less than 15 000 particles. Statistical and thermal properties of fragments were investigated. The results are compared with simple fragmentation models and it is found that they often do not agree with them in the Blink-Hoover expansion but agree well with the Grady's model in the Holian-Grady expansion. In this work, the upper part of the binodal and two points on the solid – liquid branches of the phase diagram of the two-dimensional LJ-spline fluid is obtained by Gibbs ensemble Monte Carlo method. This result has been never obtained earlier. LJ-spline (spline approximated to zero) and LJ-cut fluids (with cut off potential) are studied in detail.

Acknowledgements

The author is very indebted to Dr. Karl Travis for a lot of help and thanks EPSRC for the grant.

Table of Contents

Chapters **Page No**

Chapter 3 Phase Diagram of 2-Dimensional LJ-Spline Fluid 59

List of Figures

List of Tables

Introduction

Fragmentation is an example of material failure. This is a problem with widespread applications. The fragmentation of liquids is a subset of this field but nevertheless has many applications and yet is scientifically challenging to study. A complete mathematical and physical understanding of fragmentation is currently beyond reach given the complexity involved. In many cases there is even a lack of qualitative explanations. The aim of theory is to predict the number of fragments, their size and mass distribution and shape, as well as their velocity and spatial distributions.

Fragmentation modelling is highly challenging because it involves fluid mechanics, dynamics and non-equilibrium statistical mechanics. There are many applications of these three fields which will gain from the ability to describe fluid fragmentation. Vaporisation can also be considered as expansion and fragmentation. In our project we will use Molecular Dynamics (MD) in an attempt to determine the mass and fragment size distributions comparing our simulation results to those of the many comprehensive theories.

To describe the phenomenon of destruction quantitatively one must firstly to achieve the ability to simulate the fragmentation of a fluid under homogeneous adiabatic expansion. When this task is solved one can move on to simulation of fragmentation of solids, which is a more complicated problem. A complete mathematical and physical understanding of liquid fragmentation is currently beyond reach given the complexity involved. Modelling provides the best hope for making progress in this area. There were a few successful attempts to simulate fluid fragmentation by molecular dynamics hence there is a need to perform many. MD simulation of fragmentation of liquids is the aim of our work. While this phenomenon can be modelled by both Finite Element Method and Finite Difference Method, there are inherent difficulties with these approaches.

In Chapter 1, we give a literature review of the fragmentation science. We describe its applications, and theories of fragmentation, and attempts of atomistic simulation of the process. In Chapter 2, the methodology of our work is described in detail. The Molecular Dynamics method is explained and the tricks we are using with it: boundary conditions, minimum image convention, method of integration, the potentials, temperature measurements. NPT Molecular Dynamics and Monte Carlo method are introduced as well. A particular attention is given to the Gibbs Ensemble Monte Carlo. Various cluster definitions are discussed.

Chapter 3 is devoted to phase diagrams of two-dimensional fluids. In it, the binodal of the two-dimensional LJ-spline fluid is obtained by Gibbs ensemble Monte Carlo simulations. The second and the third virial coefficients for this fluid are calculated and the pressure is calculated with them and compared with the pressure obtained by Monte Carlo method. Two points on the solid – liquid phase diagram were obtained numerically and the solid – liquid curves were drawn along them. Nobody has done it before. In Chapter 4, extensive simulations with the Holian-Grady method are performed for systems up to 541 696 particles. Earlier simulations were for maximum 4225 particles and were much less extensive. It has been confirmed that fragment sizes obey the bimodal distribution. The fragment translational, rotational, thermal and monomer temperatures are calculated. The relative shape anisotropy is obtained. A comparison with a simple Grady's model of fragmentation has been performed and a good agreement is noticed: the average cluster size depends weakly on the system size but is proportional to the expansion rate power -1.22.

In Chapter 5, extensive simulations with the Blink-Hoover method are presented for systems up to 541 696 particles. Our predecessors performed much less extensive simulations for maximum 14491 particles. We performed a comparison of our results with four simple models of fragmentation known from the literature and found that the dependence of the maximum cluster size on the system size does not agree with any model. However, for a system with the density 0.65 and temperature 0.65, this dependence is close to the model No 3. We also examined the dependence of the largest fragment size on the pressure in the system and found that this dependence decreases with the size to the one predicted by model No 3. The fragment translational, rotational, thermal and monomer temperatures are calculated. The gyration radius and relative shape anisotropy are also obtained. In Chapter 6, the numerous conclusions are presented.

Chapter 1

Literature Survey

1.1 Science of Fragmentation

1.1.1 Applications

There is a wide range of physical and engineering applications involving fragmentation: fragmentation of brittle solids (Herrmann 1995), break up of oil shale (Grady and Kipp 1980), destruction of armor, exploding munitions (Elek and Jaramaz 2008) and even fragmentation of the Universe by the Big Bang (Brown et al 1983) giving the distribution of galaxies. Other examples are fragmentation of liquids in liquid jets at the nozzle exit (Reitz and Bracco 1982) and hot nuclear matter which exhibits fragmentation (Schulz et al 1984). In geophysics is studied fragmentation of rocks due to geological processes or explosions (Grady and Kipp 1987).

1.1.2 Approaches

Fragmentation can be caused either by abrupt forces or by static ones. The difference in the mechanisms of both types of failure is still not understood. Indeed, there are many similarities in both processes. To understand the nature of fragmentation, we have to study this phenomenon both physically and statistically. Even if the object is perfectly symmetrical, its fragmentation is random and the distribution of fragments size and shape requires a statistical description. In our work we will focus mainly on the dynamic failure caused by abrupt forces.

1.2 Statistical Theories

One of the earliest papers on statistical theory of fragmentation is that of Lienau (Lienau 1936). He studied the statistical problem of random partitioning of a line and the distribution of the resulting fragment lengths. He considered a straight infinite line upon which the breaking points are distributed at random with the Poisson distribution with a density of $1/\bar{s}$ per unit length, where $\bar{s}$ is the average fragment length. A sample with the length L, large in comparison with $\bar{s}$, will have a number of fragments given by the integer approximately equal to

$$N = L/\bar{s}\,,\; N >> 1 \qquad (1.1)$$

Hence a large number N of fragments may be expected to contain ν fragments larger than a fragment size s, where ν is very nearly

$$\nu(> s) = N\exp\left(-s/\bar{s}\right),\; N >> 1 \qquad (1.2)$$

where L is the length of the sample and $\bar{s}$ is estimated from (1). The theory of Lienau was improved in (Grady and Kipp 1985, Grady 1990, Elek and Jaramaz 2008) as it is shown below.

Mott and co-worker (Mott and Linfoot 1943) extended the one-dimensional case to the random fragmentation of a two-dimensional thin shell for which the fragments retain the form of the shell, and derived his well-known distribution relating the cumulative number of fragments and the fragment mass:

$$N(a) = N_0\exp\left(-\sqrt{2N_0 a}\right) \qquad (1.3)$$

where a is a fragment area and N_0 is the number of fragments. These authors also obtained an analytic solution for an infinite area randomly fragmented by horizontal and vertical lines, Fig. 1.1:

$$N(a) = 2N_0\sqrt{N_0 a}K_1\left(2\sqrt{N_0 a}\right) \qquad (1.4)$$

Here K_1 is the modified Bessel function. However, the difference between Eqs. (1.3) and (1.4) is not that big.

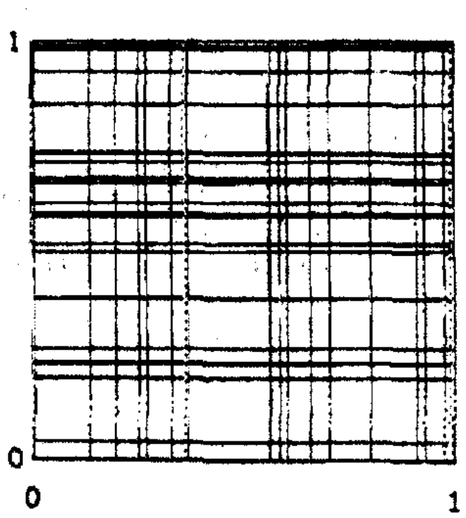

Figure 1.1. Random fragmentation of the unit square with horizontal and vertical lines.

Nowadays, attempts are made to extend the statistical theory to three dimensions and to improve one and two-dimensional descriptions (Grady and Kipp 1985, Grady 1990, Zhang et al 1999, Higley and Belmonte 2008, Elek and Jaramaz 2008). In (Grady and Kipp 1985) they consider an infinite body, in (Grady 1990) the author takes the finite size effects and discreteness of the body into account. In (Elek and Jaramaz 2008) the same problems are considered. In (Zhang et al 1999) fracture growth is introduced into equations. Higley and Belmonte (Higley and Belmonte 2008) study the effect of preferred fragment sizes. A detailed description follows.

In (Grady and Kipp 1985) they examine the one-dimensional fragmentation problem of a finite line of the length l_0 using binomial statistics and derive a formula for the cumulative fragment number per unit length:

$$N(l) = N_0\left(1-\frac{l}{l_0}\right)^{N_0 l_0} \tag{1.5}$$

where N_0 is the average number of break points per unit length, and l is the length of a fragment. They compared Eq. (1.5) with experimental data on fragmentation of thin ductile metal rings and found a rather good agreement. In the same paper they developed an alternative Poisson theory of area fragmentation. In some previous works an area was randomly fragmented by two sets of parallel lines, Fig. 1.1. However, there are many ways that straight or curvilinear lines can randomly fragment an area and it leads to different distributions. Grady and Kipp proposed a method for randomly partitioning an area which is free from this disadvantage. They view the fragment area as a scalar variable. This supposition leads to a cumulative fragment number distribution

$$N(a) = N_0\exp(-N_0a) \qquad (1.6)$$

where N_0 is the average number of fragments per unit area, and a is the fragment area. Analogously, for random fragmentation of a three-dimensional body one can write

$$N(v) = N_0\exp(-N_0v) \qquad (1.7)$$

where v is the fragment volume. The distribution (1.5) is used for description of random area fragmentation by computer and a pretty good agreement was found. It is shown that Eq. (1.7) gives good results describing inhomogeneous fragmentation modelled by computer and experimental ones through a method of Poisson mixtures.

The theory of (Grady and Kipp 1985) is applicable to continuous and infinite bodies. That is, fragment size can be arbitrarily small or arbitrarily large. In (Grady 1990) this theory is extended to discrete and finite bodies. For a discrete but infinite body a cumulative fragment distribution for mass m is

$$N(m) = N_0(1 - \delta/\mu)^{\mathrm{m}/\delta} \qquad (1.8)$$

where N_0 is the number of fragments per unit mass, δ is a minimum fragment mass, μ is the average fragment mass. For a finite continuous body this distribution is given by the formula

$$N(m) = N_0(1 - m/M)^{(\mathrm{M}/\mu)-1} \qquad (1.9)$$

where M is the mass of the body. The distribution for a discrete and finite body is much more complicated.

In (Grady 1990) the statistical theory was compared with molecular dynamics fragmentation studies performed in (Holian and Grady 1988) and compelling agreement was obtained. The theory was also applied to a nuclear fragmentation resulting from a collision of a carbon nucleus with a silver nucleus. A reasonable agreement has been obtained.

It has been also shown that the cumulative number distribution for the galaxies which are the result of the Big Bang is in a good agreement with the Grady's theory of random homogenous fragmentation.

Zhang et al (1999) used the concepts of crack propagation to show that there is a minimum fragment size. They suppose that numerous cracks will be nucleated at random but only a few of the cracks will run through the sample and break it. The authors deduce a set of equations for the size distribution curve and fragment number and extend them to two and three dimensions. The parameters in those equations are physically determined but not fitted as in the previous works. Comparison with experimental data has been done. One can conclude that the agreement is quite good and the method has a very good predictive capability.

In (Higley and Belmonte 2008) mathematical equations for modelling of fragmentation in one-dimensional brittle rods were derived. Earlier it had been supposed that the fragment distribution is scale-invariant or has only one preferred fragment size. However, in (Gladden et al 2005) it was experimentally found that in the fragmentation in thin brittle rods there are preferred fragment sizes. Higley and Belmonte try to explain this phenomenon. They supposed that the preferred sizes are due to the coherent peaks in the deformation preceding the fracture. The authors also improve the single fracture Poisson process (Grady and Kipp 1985). This process is correct if the sizes of fragments are independent of the number of fragments, however, it is not the case. The resulting formula is capable of describing both exponential and non-power distributions. The equations contain the probability of breaks along the length of the rod and produce the distribution of fragments. The simulations qualitatively match the experimental results of destruction of brittle rods after dynamic buckling.

In (Elek and Jaramaz 2008) the approach of (Lienau 1936) has been generalised to the two- and three-dimensional case through the Meijer and Bessel distributions. The Voronoi diagrams have also been applied to describe fragmentation. The authors compared a number of distributions with limited experimental results. It has been found that the modified Zhang distribution provides the best compatibility for the one-dimensional case. In the Zhang distribution (Zhang et al 1999) the average fragment length is 3.25 times larger than the minimum one; in the modified Zhang distribution it is 2.70 times larger according to the approach of (Zhou et al 2005, 2006a). The Voronoi method gives the best agreement for two dimensions, and the Mott distributions (Mott and Linfoot 1943, Mott 1947) are the best for fragment volume distribution in three dimensions. The presented models were compared also with two-dimensional numerical segmentation of a unit square given on Fig. 1.1. Eq. (1.4) describes the data excellently, Eq. (1.3) describes them not much worse but the other distributions are much worse.

1.3 Physical Theories

Among the theories which take the physics of the process into account one can mention (Mott 1947, Grady 1982, Kipp and Grady 1985, Blink and Hoover 1985, Glenn and Chudnovsky 1986, Glenn et al 1986, Ashurst and Holian 1999a, Guicheret-Retel et al 2004, Grady 2008).

Mott (Mott 1947) developed a theory of the break-up of a cylindrical bomb which consists of a number of coaxial circular rings. He considers a one-dimensional expanding ring which breaks into many pieces under rapidly applied loading, Fig. 1.2. In his model cracks randomly appear and in the crack neighbour region further fracture is forbidden. In his theory a basic assumption was made: the probability of fracture of an un-fractured specimen of unit length when the strain increases by $d\varepsilon$ increases by $dp = c\exp(\gamma\varepsilon)d\varepsilon$, where c and γ are experimentally determined constants. Mott used a graphical method to plot the probability density function of the fragments. His distribution depends on the radius and velocity of the bomb at the moment of failure, and on the mechanical properties of the material. The theory of Mott continues to influence fracture science up to the present.

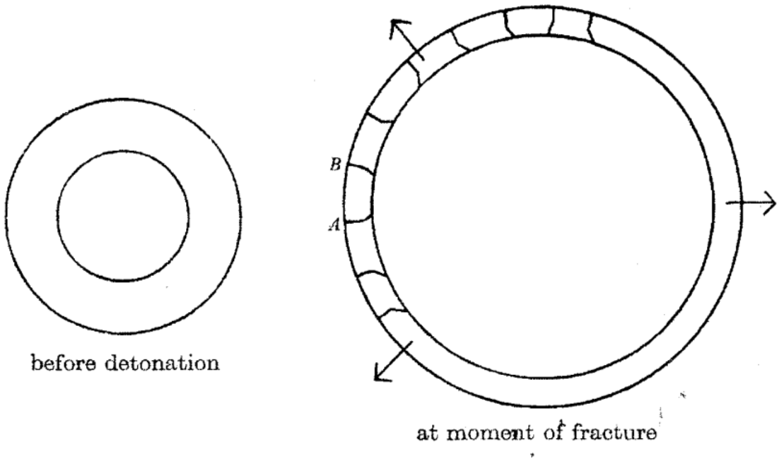

Figure 1.2. A ring from a cylindrical ring-bomb before detonation and at the moment of fracture (Mott 1947).

The models of Grady (Grady 1982, Grady 2008) balance the surface energy against the local kinetic energy of the fragments. The local kinetic energy is the kinetic energy relative to the centre of mass of the fragments. In (Grady 1982) dynamic fragmentation in a fluid medium has been considered and an equation for the equilibrium fragment surface area has been derived (the equilibrium means equality of the surface and kinetic energy):

$$A = \left(\frac{3\dot{\rho}^2}{5\rho\gamma} \right)^{1/3} \tag{1.10}$$

where ρ is density, $\dot{\rho}$ is the rate of change of density and γ is the surface energy (surface tension). Eq. (1.10) was compared with the experimental data for oil shale and steel and a reasonable agreement has been found.

In (Grady 2008) a short survey of experimental and theoretical size distributions resulting from dynamic fragmentation is given. It is concluded that the theories (Mott 1947, Grady 1982) were pretty successful in describing ductile materials. However, they are problematic when applied to brittle solids. Experimental fragment distributions for ductile materials are exponential or exponential-like, but those for brittle solids have a power law form. Grady attempted to explain the dynamic fragmentation of brittle solids. He demonstrated a very close analogy between such a fragmentation and turbulence in fluids. He proposed the following cumulative distribution function:

$$N(x) = \frac{N_0}{1+\left(\frac{x}{\lambda}\right)^{\delta}} \tag{1.11}$$

Here $N(x)$ is the number of fragments of size greater than x, N_0 is the total number of fragments, λ is the average fragment size and δ is the fractal dimension. The author tries to extend his previous energy-based theory and obtains a sensible agreement with an experiment.

Kipp and Grady (Kipp and Grady 1985) use a mechanical approach for evaluation of the fragment sizes in dynamic fragmentation of an expanding ductile ring. They extend the calculation of Mott (Mott 1947) to include energy dissipation within the fracture and obtain simple expressions for the average fragment size and fracture time. However, they do not compare the results with an experiment. They only found that the calculated minimum fragment size is in a very good agreement with the experimental value.

Glenn and Chudnovsky (Glenn and Chudnovsky 1986) modified Grady’s model to include the strain energy. Their model predicted that the stored elastic energy must play the dominating role in brittle materials destruction, however, comparison with available experimental data indicated that it is not the case at all. Therefore, this model was modified in (Glenn et al 1986) using the theory of linear elastic fracture mechanics. The new approach predicts the average fragment size as a function of the strain rate and properties of the material. It also unifies the previous theories: it yields Griffith’s result at low strain rates and Grady’s solution at high strain rates. Griffith’s theory was developed for static loading (Griffith 1921), according to it fragmentation is characterised by the balance between potential and surface energy, and the specimen fails when the largest crack reaches the critical size.

The authors of (Guicheret-Retel et al 2004) consider fuel pellets cracking in a nuclear reactor due to thermal expansion. They assume that pellets fragment into eight equal parts, which corresponds to the most likely situation. They model the fragmented state of the pellet with the aim of simulating stress and strain fields in it. Their method consists of a one-dimensional finite-element model with added parameters describing the fuel as an anisotropic damaged material. Then the parameters of the model are adjusted so that it can simulate three-dimensional pellets. The model is able to account for the opening and closing of pellet cracks. The simulations of elastic and viscoplastic material behaviours give very satisfactory results.

1.4. Atomistic Simulation

Materials fracture is an extremely complex problem involving crack nucleation, growth, and interactions, material properties, microstructure, loading conditions etc. Therefore, fragmentation models are highly simplified. However, it is possible to explore the problems microscopically by molecular dynamics. Such attempts were made, for example, in (Blink and Hoover 1985, Holian and Grady 1988, Toxvaerd 1998, Ashurst and Holian 1999ab).

In (Blink and Hoover 1985) fragmentation of a two-dimensional Lennard-Jones fluid during the expansion of this fluid into a much larger low-pressure volume was studied using molecular dynamics. 169-, 721-, 2611-, and 14 491-particle systems and five level heating (initial pressures) were used and four models of fragmentation were checked. This molecular dynamics study confirmed the Grady's model of fragmentation. His model predicts that the number of fragments is proportional to the 1/3 power of the number of particles and the −4/3 power of the initial pressure. The molecular dynamics results of Blink and Hoover agree with these predictions with high accuracy. The three other models were ruled out: the model in which the surface tension balances the initial pressure; the model in which static pressure transforms into dynamic expansion pressure; the model in which only the dilational energy of the outer shell is used in the current model. However, the fragment sizes are about ten times lower than the Grady's model prediction. Nevertheless, this is a very good result because in experiments much smaller fragments are observed than predicted by the physical theories (Lankford and Blanchard 1991, Shih et al 2000, Wang and Ramesh 2004).

The authors of (Holian and Grady 1988) consider homogeneous adiabatic expansion of a condensed Lennard-Jones - spline fluid (the potential is smoothly truncated by using spline. A detailed description of this potential is given in Chapter 2). The fluid thereby exhibits fragmentation. They also study the process by molecular dynamics. They consider a two-dimensional infinite system which consists of periodic squares. In every rectangle there are N atoms. The periodic boundary conditions are imposed. The rectangles expand linearly with time:

$$L(t) = L_0(1+\dot{\eta}t) \qquad (1.12)$$

where L_0 is the initial length and $L_0\dot{\eta}$ is the boundary velocity. Holian and Grady found that the dependence of the cumulative number of clusters on the size of the clusters is a bimodal distribution, that means it has two different modes. Its first mode is the average cluster size (excluding monomers) and the second mode is the number of monomers. It has been shown that homogeneous fragment distributions are exponential with fragment mass rather than with its diameter as has been suggested earlier (Mott and Linfoot 1943). The average fragment mass (the number of atoms in a cluster) μ is inversely proportional to $\dot{\eta}^{4/3}$. The result is in reasonable agreement with Grady's model (Grady 1982), however, the latter overestimates it by the factor of 3.

Toxvaerd (Toxvaerd 1998) applied the technique of (Holian and Grady 1988) for two- and three dimensional Lennard-Jones fluids. In the previous works a certain interparticle distance was specified as the definition of a cluster. If the distance between the particles is less than this distance then they belong to the same cluster. This method contains some arbitrariness. Toxvaerd used another criterion which has no arbitrariness, namely, the structure factor, $S(q)$, for small wave number q. He finds that the distribution of fragments is established at early times of the expansion (this is so-called nontrivial fragmentation) and the fragment sizes are exponentially distributed. He also observed nontrivial fragmentation only for expansions for which the system enters the liquid-gas region on the phase diagram. The results for three-dimensional systems differ very much from two-dimensional ones. For the three-dimensional case a non-trivial fragmentation is possible only for expansion rates for which the viscous phase separation does not take place. Viscous phase separation is separation of a fluid into two phases at compositions and temperatures where it leads to the decrease of the free energy. The rate of such separation is approximately proportional to the initial viscosity.

Ashurst and Holian (Ashurst and Holian 1999ab) extended the work (Holian and Grady 1988) by using the Lennard-Jones potentials with larger cut offs, Figs. 1.3, 1.4 and 1.5. They do not approximate it by spline but shift so that it is zero beyond the cut off. They also simulated three-dimensional systems. The authors compared the Grady's model and a strain energy one (it transforms elastic potential energy gained from the expansion of the system into the surface energy which is responsible for breaking bonds and formation of new surfaces). The latter model gives better agreement with the simulation results (the former one overestimates the results), however, both models predict that $\mu = \mathrm{const} / \dot{\eta}^{p}$ where $p = 2D/3$ and D is the dimensionality. This model and the MD study agree well with experimental results obtained from the free-jet expansion of liquid helium. In this study it is also found that the cumulative number of clusters is a bimodal distribution.

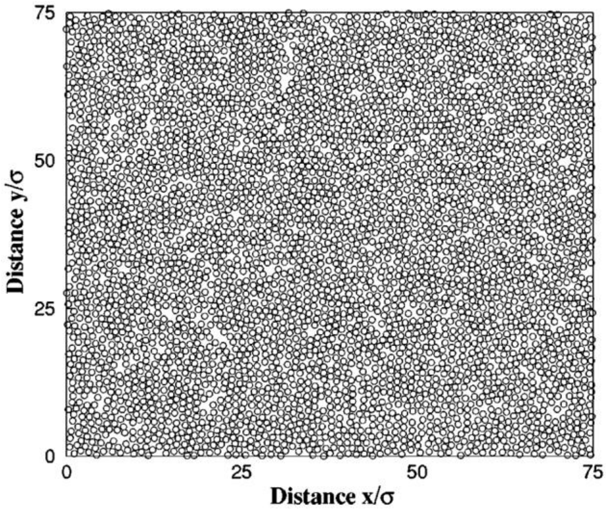

Figure 1.3. An initial two-dimensional liquid configuration with a reduced density of 0.75 and a reduced temperature of 0.6; Lennard-Jones potential (Ashurst and Holian 1999a).

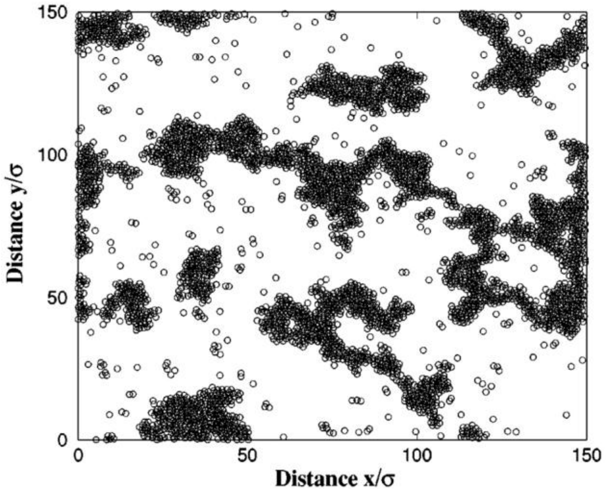

Figure 1.4. Clusters formed by expanding in two dimensions at the rate $\dot{\eta} = 0.01$ until the domain size has doubled (Ashurst and Holian 1999a).

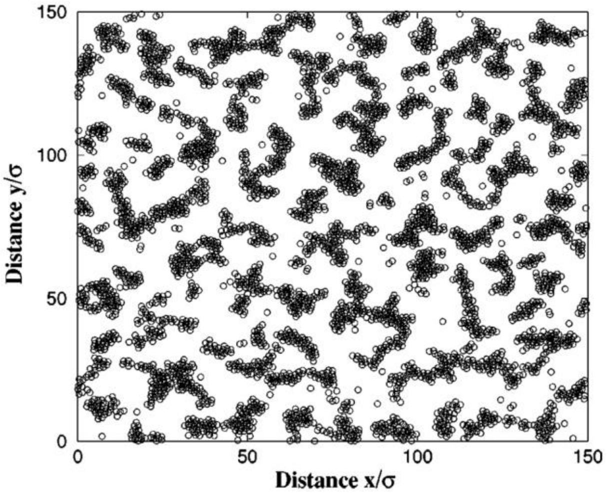

Figure 1.5. Clusters formed by expanding in two dimensions at the rate $\dot{\eta} = 0.1$ until the domain size has doubled (Ashurst and Holian 1999a).

1.5. Numerical Theories

Some authors applied numerical approaches (Zhou et al 2005, Zhou et al 2006ab, Gold and Baker 2008). Physical theories consider materials failure as an instantaneous event although it is a time-dependent process. Also, as it was mentioned above, fragmentation models are highly simplified. The time-dependence is inherent to numerical models. They also include complicated mechanics and physics of the process.

In (Zhou et al 2005) a one-dimensional modelling of brittle ceramic fragmentation has been carried out. The approach takes into account many mechanisms: elastic wave interaction, cohesive crack opening and closing, dynamic crack nucleation, local strength distribution, etc. It has been shown that the average fragment size and the fragment size distribution (variance) decreases with the strain rate. At low strain rates the fragment size is twice larger than that of (Glenn and Chudnovsky 1986). At very high strain rates it is about four times less than that of (Grady 1982). The theory can predict the number of fragments and the sizes of these fragments can be estimated. The authors also investigate the influence of initial defects on the fragmentation and fragment size distribution. It was found that the cumulative fragment number function depends on the strain rate.

Zhou and co-workers (Zhou et al 2006a) studied Mott's problem numerically for brittle materials (fragmentation of a one-dimensional expanding ring). The authors use a numerical approach which takes into account crack initiation, growth, and interactions, and the material's properties. Based on the results of the simulation they propose an empirical formula for the average fragment size and an empirical expression for the cumulative distribution function:

$$N(>s) = N_0 \exp\left[-\left(\frac{s-s_{\min}}{s_0}\right)^2\right]. \tag{1.13}$$

Here s is a fragment size, N_0 is the total number of fragments, $s_{\min}$ is the minimum fragment size and s_0 is the scaling parameter. For small strain rates the calculated average fragment size is about twice greater than the Glenn-Chudnovsky result. For high strain rates the calculated average fragment size is smaller than that given by the Glenn-Chudnovsky and Grady's models. It is interesting that $s_{\min}/\langle s\rangle = 0.37$ for all strain rates. The distribution Eq. (1.11) agrees with experiment better than other proposed distributions. Both empirical formulae have a good predictive capability.

In (Zhou et al 2006b) the approach of (Zhou et al 2005) is extended to a circular ring which is dynamically expanded. Two regimes were investigated: free expansion and constant velocity expansion. The following major results have been obtained:

1. Fragmentation of a ring with constant velocity expansion is identical to the fragmentation of a one-dimensional bar.

2. The average fragment size decreases with the increase of the strain rate; the minimum and maximum sizes also decrease.

3. The fragment sizes distribution can be described by a Rayleigh function with a good accuracy. The ratio of the average fragment size to minimum size is almost independent of the strain rate. The ratio of the maximum fragment size to average size increases linearly with the logarithm of strain rate.

4. The fragment size is independent of the ring size in an expansion with a constant velocity (given the same strain rate).

The fragment size calculated by this model for low strain rates is 2 – 3 times larger than Glenn and Chudnovsky’s estimate. For higher strain rates it is 1/3 – 1/4 smaller. It is smaller than Grady’s estimate for all strain rates. Also are investigated the effects of ring size and the material properties.

In (Gold and Baker 2008) the Mott’s theory (Mott 1947) of explosion of cylindrical ring-bombs is introduced into the CALE computer program (Tipton 1991). According to his theory, in these bombs the average length of the circumferential fragments is a function of the radius and velocity of the ring at the moment of disintegration, and the mechanical properties of the material. CALE is a program for solving two-dimensional and three-dimensional axial symmetric high-rate problems by the finite difference method. It uses arbitrary Lagrangian–Eulerian formulation of the main equations. The authors simulated the performance of fragmentation munitions and got an excellent accuracy for fragment sizes, the number of fragments, fragment velocity distribution etc. They proved that their method has a very good predictive capability. Experiments using flash radiography, high-speed photography, and sawdust fragment recovery were also carried out in their work.

Chapter 2

Simulation Methodology

2.1 Molecular Dynamics

Molecular dynamics (MD) is an atomistic simulation method closely linked to Boltzmann's formulation of statistical mechanics. The motion of a set of particles is evolved by solving classical equations of motion using a finite difference integration scheme. Once a potential energy function has been specified, MD is essentially exact. Thermodynamic properties are obtained as time averages of certain instantaneous functions of the positions and momenta of the atoms (phase functions). Basic MD can employ Newton's equations of motion but a more useful choice is to use Hamilton's coupled set of first order motion equations:

$$\begin{aligned} \dot{\mathbf{p}}_j &= -\frac{\partial H}{\partial \mathbf{q}_j} \\ \dot{\mathbf{q}}_j &= \frac{\partial H}{\partial \mathbf{p}_j} \end{aligned} \qquad (2.1)$$

where $\mathbf{p}_j$ are the generalised momenta and $\mathbf{q}_j$ are the generalised coordinates, and H is the Hamiltonian function, $H = \frac{1}{2}\sum_{i=1}^{N} \frac{\mathbf{p}_i^2}{m_i} + U(\mathbf{q})$ where $U(\mathbf{q})$ is the potential energy function.

2.1.1 Initial conditions

To evolve trajectories, one must specify the initial state of the system. For the positions, any convenient set of atomic positions will do if the object of study is a liquid. Typically, a lattice starting structure is used. The momenta are typically sampled from a Maxwell-Boltzmann distribution whose width (variance) is related to the temperature of interest. The manner in which this is achieved is described below.

(i) First, random numbers are generated from a uniform distribution on the interval (0, 1).

(ii) These random numbers are then transformed into random numbers sampled from a normal distribution with zero mean and unit variance – the Box-Muller method (Allen and Tildesley 1991).

Suppose ξ_1 and ξ_2 are two uniform random variables sampled at (0, 1). Then ζ_1 and ζ_2 are now normally distributed: $\zeta_1 = (-2\ln\xi_1)^{1/2}\cos 2\pi\xi_2$ and $\zeta_2 = (-2\ln\xi_1)^{1/2}\sin 2\pi\xi_2$

(iii) Finally these values are scaled by a factor σ (σ is the standard deviation of velocity). Then the Box-Muller distribution of the velocity components is $\rho(v_i) = \frac{1}{\sqrt{2\pi}\sigma} exp\left(-\frac{\zeta_i^2}{2\sigma^2}\right)$, $i = 1$, 2, and thus the variance is σ^2.

One then zeroes the total momentum and finally one should rescale the momenta to give the desired temperature, which will have changed as a result of the zeroing.

2.1.2 Boundary conditions

MD, involving the solution of differential equations requires boundary conditions. The boundary conditions can be of different types. The most common choice for modelling bulk materials is to employ periodic boundary conditions (PBCs) (Allen and Tildesley 1991). In this method the system is modelled as a grid of periodically repeated cells. Each cell contains N particles. When a molecule passes through one side of the cell, it appears on the opposite side with the same velocity. Thus a periodic system in two dimensions is an infinite checkerboard of identical systems, Fig. 2.1. The PBCs are useful for simulating a bulk environment to avoid the influence of surfaces because in small systems atoms in the surface layer constitute a significant portion of the population.

Other types of boundary conditions used in MD simulations include: free boundaries, rigid boundaries and mirror boundaries (Hoover 2006). Mirror boundaries are useful in situations where the substance to be modelled is not homogeneous, for example a fluid in a gravitational field or the interface between a fluid and a thermal reservoir. The idea of the mirror boundary condition is that particles near a mirror boundary have reflected images across the “mirror” and thus may interact with them. The image particles may be static or they may move with a finite velocity (dynamic mirrors). The mirror boundaries allow the fluid properties to be continuous across an interface and may even be used to facilitate heat flow, for example. Rigid and mirror choices are good for boundaries fixed in space. A convenient way to model the rigid boundary is to use a steep repulsive potential to prevent material from crossing an interface.

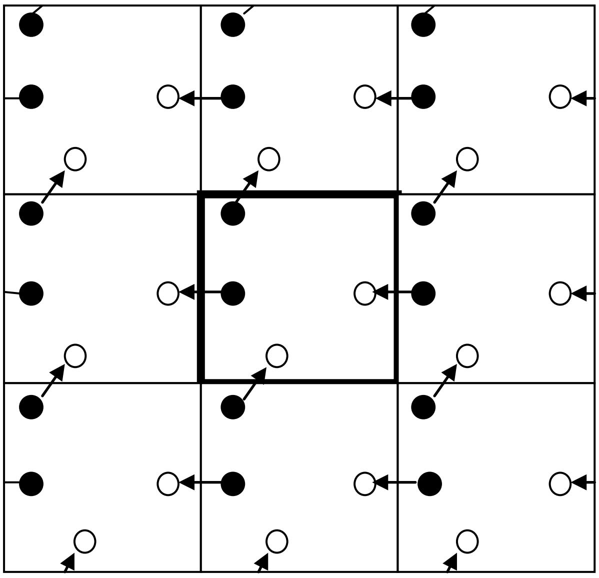

Figure 2.1. Periodic boundary conditions. Filled circles, initial positions of atoms, open circles, their positions after displacement.

2.1.3 Integration scheme

There are a number of methods for numerical integration in MD simulations. Let us mention some of them. The Verlet method is widely used for integration of Newton’s equations of motion in MD simulations [Verlet 1967]. In this method, the acceleration of a particle is approximated as a centred difference quotient:

$$\mathbf{a}(t) \approx \frac{\mathbf{r}(t+\mathrm{d}t) - 2\mathbf{r}(t) + \mathbf{r}(t-dt)}{\mathrm{d}t^2} \qquad (2.2)$$

where d*t* is the increment in time, $\mathbf{a} = \mathbf{F}/m$ and $\mathbf{F} = -\partial U / \partial \mathbf{r}$. The new coordinate $\mathbf{r}(t + \mathrm{d}t)$ can, therefore, be defined from the coordinates at times $t - \mathrm{d}t$ and t, and from the acceleration at the time t:

$$\mathbf{r}(t+\mathrm{d}t) \approx 2\mathbf{r}(t) - \mathbf{r}(t-dt) + \mathbf{a}(t)\mathrm{d}t^2 \qquad (2.3)$$

This method is simple, offers a good stability and is time reversible. This method has an accuracy of $O(\mathrm{d}t^2)$ which is not that high. It is not self-starting, however this is not a problem because only one point has to be estimated at the beginning of the simulation and the error of that estimation is negligible over a large number of steps. Another disadvantage is that velocities are not explicitly calculated.

In Gear's method, one considers the differential equation $\dot{\mathbf{r}} = f(\mathbf{r},t)$ or $\ddot{\mathbf{r}} = f(\mathbf{r},t)$. Positions, velocities, accelerations etc. at time $t + \mathrm{d}t$ can be estimated by Taylor expansion:

$$\mathbf{r}^{\mathrm{p}}(t+\mathrm{d}t) \approx \mathbf{r}(t) + \mathbf{v}(t)\mathrm{d}t + \frac{\mathbf{a}(t)\mathrm{d}t^2}{2} + \frac{\mathbf{b}(t)\mathrm{d}t^3}{6}$$

$$\mathbf{v}^{\mathrm{p}}(t+\mathrm{d}t) \approx \mathbf{v}(t) + \mathbf{a}(t)\mathrm{d}t + \frac{\mathbf{b}(t)\mathrm{d}t^2}{2}$$

$$\mathbf{a}^{\mathrm{p}}(t+\mathrm{d}t) \approx \mathbf{a}(t) + \mathbf{b}(t)\mathrm{d}t \qquad (2.4)$$

The superscript "p" means predicted value. One can calculate from the predicted positions $\mathbf{r}^{\mathrm{p}}$ the correct accelerations $\mathbf{a}^{\mathrm{c}}(t + \mathrm{d}t)$ (from the equations of motion). One can obtain the difference between the predicted and correct accelerations:

$$\Delta\mathbf{a}(t+\mathrm{d}t) = \mathbf{a}^{\mathrm{c}}(t+\mathrm{d}t) - \mathbf{a}^{\mathrm{p}}(t+\mathrm{d}t) \qquad (2.5)$$

Then a corrector step is made:

$$\mathbf{r}^{\mathrm{c}}(t+\mathrm{d}t) = \mathbf{r}^{\mathrm{p}}(t+\mathrm{d}t) + c_0\Delta\mathbf{a}(t+\mathrm{d}t)$$

$$\mathbf{v}^{\mathrm{c}}(t+\mathrm{d}t) = \mathbf{v}^{\mathrm{p}}(t+\mathrm{d}t) + c_1\Delta\mathbf{a}(t+\mathrm{d}t)$$

$$\mathbf{a}^{\mathrm{c}}(t+\mathrm{d}t) = \mathbf{a}^{\mathrm{p}}(t+\mathrm{d}t) + c_2\Delta\mathbf{a}(t+\mathrm{d}t) \qquad (2.6)$$

The resulting $\mathbf{r}^{\mathrm{c}}(t+\mathrm{d}t)$ etc. are better approximations to the true values. The coefficients c_{i} are tabulated (Allen and Tildesley 1991). The process may be iterated: new accelerations are calculated from the corrected positions $\mathbf{r}^{\mathrm{c}}$ and positions, velocities and accelerations are refined through Eq. (2.6).

This method has an error of $O\,(\mathrm{d}t^3)$. It achieves a very good accuracy and also has an excellent stability. However, it is not self-starting and requires two starting points to produce a solution. These points are generated with a first order approximation. This increases the complexity of programs and the memory for the code.

Another simple second order method is Leapfrog algorithm. It integrates equations of the form

$$\ddot{\mathbf{r}} = f(\mathbf{r}) \tag{2.7}$$

The Verlet method has a weakness: the velocities are not part of the finite difference scheme. In the Leapfrog algorithm, one solves the following equations for coordinates and velocities:

$$\mathbf{r}_n = \mathbf{r}_{n-1} + \mathbf{v}_{n-1/2}\mathrm{d}t \tag{2.8}$$

$$\mathbf{a}_n = f(\mathbf{r}_n) \tag{2.9}$$

$$\mathbf{v}_{n+1/2} = \mathbf{v}_{n-1/2} + \mathbf{a}_n\mathrm{d}t \tag{2.10}$$

They involve half step velocities which are then advanced ahead of the positions, hence the name ‘leapfrog’. There are two strengths to this method. The first one is the time-reversibility. The second one is that it conserves the energy of dynamical systems, i.e. it is symplectic. This method has an accuracy of $O\,(\mathrm{d}t^3)$. It is not self-starting.

In our work we use a fourth-order Runge-Kutta scheme. It is typically employed to integrate the MD equations of motion. This method has a local truncation error of $O(\mathrm{d}t^5)$. It involves four ‘force’ evaluations per time step but the numerical effort is worth it for the increased energy conservation. The method *is* self-starting, and it solves very well problems with Lyapunov instability.

Runge-Kutta method of the order *n* is designed to reproduce the first *n* terms in a Taylor series expansion. Again, one considers the differential equation $\dot{\mathbf{r}} = f(\mathbf{r}, t)$ with the initial condition $\mathbf{r}(t = 0) = \mathbf{r}_0$. The fourth order Runge-Kutta method gives the following solution:

$$\mathbf{r}_{n+1} = \mathbf{r}_n + \frac{1}{6}\left(b_1 + 2b_2 + 2b_3 + b_4\right) \tag{2.11}$$

where

$$b_1 = f(\mathbf{r}_n, t_n)\mathrm{d}t \tag{2.12}$$

$$b_2 = f(\mathbf{r}_n + \frac{1}{2}b_1, t_n + \frac{1}{2}\mathrm{d}t)\mathrm{d}t \tag{2.13}$$

$$b_3 = f(\mathbf{r}_n + \frac{1}{2}b_2, t_n + \frac{1}{2}\mathrm{d}t)\mathrm{d}t \tag{2.14}$$

$$b_4 = f(\mathbf{r}_n + b_3, t_n + \mathrm{d}t)\mathrm{d}t \tag{2.15}$$

The expression for velocities is analogous. Thus, the new coordinates and velocities at time *t* + d*t* are estimated from the known values ***r***(*t*) and ***v***(*t*) as the weighted averages of four intermediate coordinates.

It is worth noting that the harmonic oscillator problem can be solved exactly with the fourth-order Runge-Kutta scheme (Hoover 1991). This is useful for debugging purposes.

2.1.4 Potentials

The potential energy of a system of particles can be written as a sum of one-body, two-body, three-body terms etc:

$$U(\mathbf{r}) = \sum_i U_1(\mathbf{r}_i) + \sum_i \sum_{j>i} U_2(\mathbf{r}_i, \mathbf{r}_j) + \sum_i \sum_{j>i} \sum_{k>j>i} U_3(\mathbf{r}_i, \mathbf{r}_j, \mathbf{r}_k) + \ldots \tag{2.16}$$

Successive terms represent the contribution of single atoms, interaction of pairs of atoms, interactions of triplets of atoms etc. Single atoms contribute the role of the external fields, for example, influence of the walls. Three-body interactions play an important role at liquid densities (they constitute about 10% of the potential energy) but higher order interactions are not significant. It is difficult to take three- and higher order interactions explicitly in the calculations hence one often uses an effective two-body potential with adjusted parameters. The material described by such an effective potential reproduces experimental data with a good accuracy.

In MD and Monte Carlo simulations, it is common to use the pair-additive Lennard-Jones (LJ) potential:

$$U(r) = 4\varepsilon\left[\left(\frac{\sigma}{r}\right)^{12} - \left(\frac{\sigma}{r}\right)^{6}\right] \tag{2.18}$$

where r is the distance between the atoms, ε is the inter-atomic potential well depth and σ is the atom diameter (the distance at which the inter-atom potential is zero). Its plot is given in Fig. 2.2. Holian and Grady (1988) used the Lennard-Jones potential truncated at $R_{\mathrm{cut}} \approx 1.74\sigma$ and smoothly extrapolated to zero by a cubic spline from the point of inflection $R_{\mathrm{cut2}} \approx 1.24\sigma$, Fig. 2.2. We consider a two-dimensional fluid with a LJ potential truncated and smoothly extrapolated by a cubic spline with the same R_{cut} and R_{cut2}:

$$\begin{aligned} U(r) &= 4\varepsilon\left[\left(\frac{\sigma}{r}\right)^{12} - \left(\frac{\sigma}{r}\right)^{6}\right], && r \le R_{\mathrm{cut2}} \\ &= A(r - R_{\mathrm{cut}})^2 + B(r - R_{\mathrm{cut}})^3, && R_{\mathrm{cut2}} < r < R_{\mathrm{cut}} \\ &= 0, && r > R_{\mathrm{cut}} \end{aligned} \tag{2.19}$$

where $R_{\mathrm{cut}} = 1.737051855$, $R_{\mathrm{cut2}} = 1.24445506$, $A = -4.864890083$ and $B = -3.2920028$ are the coefficients.

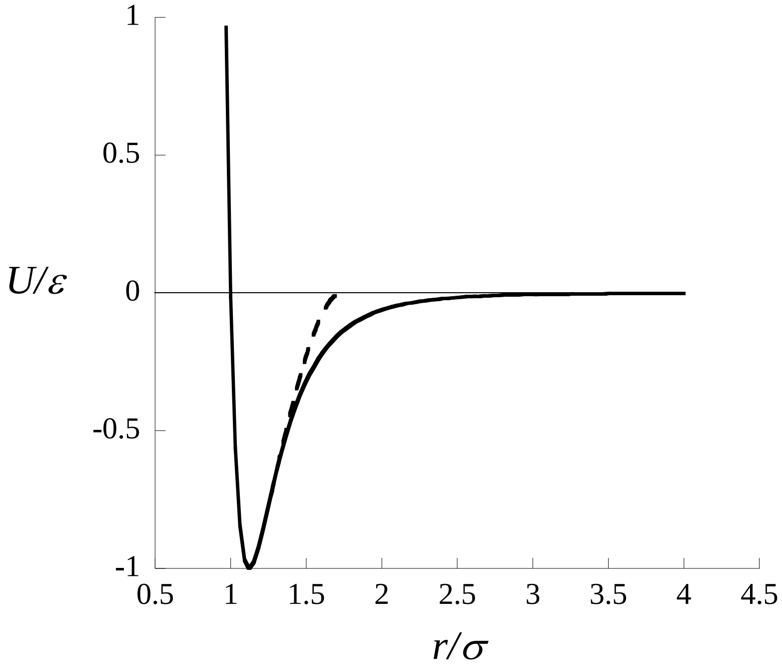

Figure 2.2. Lennard-Jones pair potential, solid line. Spline interpolated Lennard-Jones potential with zero slope at $U(r) = 0$ (Holian and Grady 1988), dashed line.

2.1.5 Potential truncation and minimum imaging

It is difficult to take into account the interactions between all molecules of the system. To reduce the amount of calculations the minimum image convention is used (also in our work) (Allen and Tildesley 1991). In the infinite lattice with the periodic boundary conditions, interactions only in one cell are considered. Every atom in the cell interacts with all other atoms in the cell. If the distance between the former atom and the latter one is greater that between the former atom and the nearest image of the latter one, then the interaction with the shortest distance is taken. The number of such interactions is $N(N-1)/2$. It still requires a substantial calculation and potential truncation is also applied. In three-dimensional simulations it is usual to truncate a potential spherically. It means, the potential $\phi(r)$ is set to zero if r is greater that a certain cut off distance r_{cut}. This approximation works well for short-range forces. In two dimensions this is replaced by a circular cutoff.

2.1.6 Temperature measurement

The simplest temperature is the gas kinetic temperature. This can be obtained through the equipartition theorem:

$$\frac{DN}{2}k_B T = \left\langle \frac{1}{2}\sum_i \frac{\mathbf{p}_i \cdot \mathbf{p}_i}{m} \right\rangle \qquad (2.19)$$

where D is the physical dimension of the system. In practice, performing MD in the centre of mass frame of reference removes D degrees of freedom, so left hand side of Eq. (2.19) becomes $\frac{D(N-1)}{2}k_B T$. The temperature is thus obtained from the time averaged mean kinetic energy per particle. In two dimensions it is correct to $O(1/N)$.

Another measure of temperature is based on the thermodynamic temperature, defined through $\frac{1}{T} = \left.\frac{\partial S}{\partial E}\right|_V$, where E is the internal energy and S is the entropy. In recent years various authors have popularized another related temperature – the configurational temperature, Eq. (2.20), which is independent of the momenta. This temperature is less convenient than the kinetic temperature but it was justified on the grounds of its perceived usefulness in non-equilibrium MD (NEMD) simulations since one avoids the difficulty of needing to estimate the thermal contribution to the velocity of atoms (Butler *et al* 1998), (Delhommelle and Evans 2001), (Braga and Travis 2005).

$$kT_{\mathrm{conf}} = \frac{|\nabla U|^2}{\nabla^2 U} \qquad (2.20)$$

The configurational temperature is also a useful diagnostic tool in the MC simulation of a many particle system because it tracks the temperature of the system even when it is not in global thermodynamic equilibrium. One does not have any momenta in MC but on can calculate the configurational temperature and estimate the thermal temperature.

2.1.7 Thermostats

Standard molecular dynamics probes the microcanonical ensemble (strictly, a subset of the microcanonical ensemble since the total linear momentum is conserved by Newton's equations in which the Hamiltonian is a constant of motion (total energy)). In laboratory experiments it is easier to control the temperature than the energy. MD can also be performed at constant temperature. To maintain the system at a constant temperature, a simple temperature rescaling is sufficient at every step: $v' = v\sqrt{\frac{kT_{\mathrm{req}}}{E_{\mathrm{kin}}}}$. Here v is the velocity of a particle, T_{req} is the required temperature and E_{kin} is the actual kinetic energy of the system. There are more sophisticated methods, for example, in the Andersen's method the velocities of particles after a collision are taken from the Maxwell-Boltzmann distribution for the desired temperature (Frenkel and Smit 2002). Despite being simple, neither of these schemes generates the correct statistical mechanical ensemble. To do this, other methods of temperature control need to be considered.

a) Gaussian thermostat

For the isokinetic ensemble one can use a Gaussian thermostat. In this scheme, the system is coupled to a heat bath. Application of the Gauss' principle of least constraint (Landau and Lifshitz 1960) leads to the following equations of motion:

$$\dot{\mathbf{r}}_{\mathbf{i}} = \frac{\mathbf{p}_{\mathbf{i}}}{m} \qquad (2.21)$$

$$\dot{\mathbf{p}}_{\mathbf{i}} = \mathbf{F}_{\mathbf{i}} - \alpha(\mathbf{r},\mathbf{p})\mathbf{p}_{\mathbf{i}} \qquad (2.22)$$

(Hoover etc 1982; Evans 1983). The quantity $\alpha(\mathbf{r},\mathbf{p})$ plays the role of a friction coefficient (though unlike friction in mechanics, can take plus or minus sign) which reduces the temperature to a constant value. It is chosen so as to satisfy Gauss's principle of least constraint (Evans et al 1983). This principle states that the actual trajectories of particles in systems with constraints deviate as little as possible (in a least-squares sense) from the Newtonian trajectories in unconstrained systems. The quantity α becomes a Lagrange multiplier which minimises the difference between the trajectories, and the resulting expression for it is:

$$\alpha = \frac{\sum_i \mathbf{p_i} \cdot \mathbf{F_i}}{\sum_i |\mathbf{p_i}|^2} \tag{2.23}$$

Gauss' principle is very fruitful in non-equilibrium molecular-dynamics of irreversible phenomena. A Gaussian thermostat does not generate the canonical ensemble, it generates the isokinetic one. However, the canonical distribution of momenta is quickly established.

b) Nosé–Hoover thermostat

There is another method to control temperature while probing the *NVT* ensemble. The Nosé–Hoover approach uses an extended Lagrangian of a *N*-body system that contains an additional coordinate *s*, and an effective mass, *Q*, linked to *s*:

$$L_{Nose} = \sum_{i=1}^{N} \frac{m_i}{2} s^2 \mathbf{r}_i^2 - U(\mathbf{r}^N) + \frac{Q}{2}\dot{s}^2 - \frac{3N}{\beta} \ln s \tag{2.24}$$

(Frenkel and Smit 2002). From this Lagrangian the following equations of motion result:

$$\dot{\mathbf{r}}_i = \frac{\mathbf{p}_i}{m_i} \tag{2.25}$$

$$\dot{\mathbf{p}} = -\frac{\partial U(\mathbf{r}^N)}{\partial \mathbf{r}_i} - \xi \mathbf{p}_i \tag{2.26}$$

$$\dot{\xi} = \frac{\sum_i \frac{\mathbf{p}_i^{\ 2}}{m_i} - \frac{3N}{\beta}}{Q} \tag{2.27}$$

Here ξ is the thermodynamic friction coefficient. Hoover proved that Eqs. (2.25) – (2.27) are unique, that is, there are no other equations of the same form which lead to *NVT* distribution. The larger *Q* results in smaller temperature fluctuations; large *Q* correspond to high inertia of the heat bath. The Nosé–Hoover method provides a way to control the temperature more smoothly than Andersen's method where the velocities are stochastically changed, and has the advantage of generating the canonical distribution of momenta. The disadvantage is the introduction of an adjustable parameter (*Q*), though this can be an advantage in certain applications.

2.1.8 NPT Molecular Dynamics

The majority of natural phenomena occur at constant pressure. It is important, therefore, to have a means of performing constant pressure MD simulations. Many methods have been developed and all of them change the volume. For example, Berendsen *et al.* (1984) described coupling to a pressure bath. They add the pressure equation to the equations of motion:

$$\frac{dP}{dt} = \frac{(P_0 - P)}{t_P} \tag{2.28}$$

Here P_0 is the desirable pressure and t_P is the time constant. At each step, the volume of the system is multiplied by a factor χ and the coordinates of centre of mass by factor $\chi^{1/3}$. This is equivalent to the temperature scaling previously described. It is given by the equation

$$\chi = 1 - \beta_T \frac{\Delta t}{t_P}(P_0 - P) \tag{2.29}$$

Here β_T is the isothermal compressibility and Δt is the time step. The knowledge of the compressibility is not necessary since it can be included in t_P.

However, this scheme does not generate the *NPT* ensemble. Hoover has developed a scheme based on Nosé’s mechanics that does this (Hoover 1985, 1986). His equations of motion are

$$\dot{\mathbf{r}} = \frac{\mathbf{p}}{mV^{1/D}} \tag{2.30}$$

$$\dot{\mathbf{p}} = \mathbf{F} - (\xi + \dot{\varepsilon})\mathbf{p} \tag{2.31}$$

$$\dot{\xi} = \frac{2(K - K_0)}{Q} \tag{2.32}$$

$$\dot{V} = DV\dot{\varepsilon} \tag{2.33}$$

$$\ddot{\varepsilon} = \frac{(P - P_0)V}{kT\tau^2} \tag{2.34}$$

Here D is the dimensionality, $\mathbf{F}$ is the force, ξ is the thermodynamic friction coefficient, ε is strain, K is the kinetic energy, K_0 and P_0 are specified mean kinetic energy and pressure, respectively, Q is an effective mass from Eq. (2.24), and τ is the relaxation time.

2.2 Metropolis Monte Carlo Method

Monte Carlo methods are a class of numerical tools involving random numbers. Basic Monte Carlo methods find wide utility in estimating certain integrals (quadrature). They work by generating random values of the integrand etc (Allen and Tildesley 1991; Frenkel and Smit 2002). The same approach cannot be used to estimate partition functions because many states in an ensemble give a small contribution to the averaged value because their Boltzmann factor is very small. The Metropolis scheme is a method of finding states with high probability from a canonical ensemble, which give a significant contribution. During a Monte Carlo simulation, one takes successive states, i.e. generates a Markov chain. If the potential energy of the successive state is less than that of the former one, then the new state is accepted. If it is greater, then the new state is accepted with the probability $\exp(-\beta\Delta U)$, where $\Delta U > 0$ is the energy difference between the states. A random number is generated and if it is less than $\exp(-\beta\Delta U)$ the move is accepted.

2.2.1 Monte Carlo in the *NVT* and *NPT* Ensembles

NVT (canonical) ensemble is a conventional one used in Monte Carlo simulations. The probability density of states for this ensemble is proportional to $\exp(-\beta H(\mathbf{r},\mathbf{p}))$ and its partition function is

$$Q_{NVT} = \frac{1}{N!\,h^{3N}} \int \exp(-\beta H(\mathbf{r},\mathbf{p}))\mathrm{d}\mathbf{\Gamma} \qquad (2.35)$$

Here $\mathrm{d}\mathbf{\Gamma} = \mathrm{d}\mathbf{r}\mathrm{d}\mathbf{p} = \mathrm{d}\mathbf{r}^N\mathrm{d}\mathbf{p}^N$ is an element of phase space, a $6N$-dimensional vector in that space. The thermodynamic function in this case is the Helmholtz energy A:

$$\beta A = -\ln Q_{NVT} \qquad (2.36)$$

The average value of a function f in this ensemble is given by

$$< f >= \frac{\int f(\mathbf{\Gamma})\rho(\mathbf{\Gamma})\mathrm{d}\mathbf{\Gamma}}{Q_{NVT}} \tag{2.37}$$

The partition function can be expressible as a product of the ideal gas and potential parts:

$$Q_{NVT} = \frac{1}{N!h^{3N}} \int \exp\left(-\beta \mathrm{K}(\mathbf{p})\right)\mathrm{d}\mathbf{p} \int \exp\left(-\beta U(\mathbf{r})\right)\mathrm{d}\mathbf{r} = Q_{NVT}^{\mathrm{id}} Q_{NVT}^{\mathrm{pot}} \tag{2.38}$$

Here $K(\mathbf{p})$ is the kinetic energy of the ideal gas and $Q_{NVT}^{\mathrm{id}} = \frac{V^N}{N!\,\Lambda^{3N}}$, where Λ is the thermal de Broglie wave length. The potential part is

$$Q_{NVT}^{\mathrm{pot}} = \frac{1}{V^N} \int \exp\left(-\beta U(\mathbf{r})\right)\mathrm{d}\mathbf{r} \tag{2.39}$$

Instead of Q_{NVT}^{pot}, the configurational integral $Z_{NVT} = V^N Q_{NVT}^{\mathrm{pot}}$ is often used. As it is easy to calculate ideal gas properties, Monte Carlo methods focus on exploration of the configurational part of phase space. The average value of a configurational function *f* in the *NVT* ensemble will be

$$< f >= \frac{\int f(\mathbf{r})\rho(\mathbf{r})\mathrm{d}\mathbf{r}}{Z_{NVT}} \tag{2.40}$$

At each MC step, an attempt is made to move a single particle (chosen randomly) by a small random displacement. *N* attempted ‘moves’ can be considered as equivalent to a single MD timestep. The random number generator produces the displacement of a particle in the *x*, *y*, and *z* directions. The magnitude of the displacement along every axis is limited to $r_{\max}$ which is found empirically though $r_{\max}$ should never exceed half the box length. The Metropolis scheme is applied to accept or reject the move.

Another widely used ensemble is the isothermal-isobaric one. It is of importance because most real experiments are carried out under constant pressure. In it, the pressure, temperature and the number of particles are kept constant but the volume fluctuates. The probability density of states for the *NPT* ensemble is proportional to $\exp\left(-\beta\left(H + PV\right)\right)$ and its partition function is

$$Q_{NPT} = \frac{1}{N!\,h^{3N} V_0} \iint exp\left(-\beta\left(H + PV\right)\right)\mathrm{d}V\mathrm{d}\mathbf{\Gamma} \tag{2.41}$$

Here V_0 is the chosen value of volume to keep Q_{NPT} dimensionless. Its choice is not important. The thermodynamic function for this ensemble is the Gibbs energy G:

$$\beta G = -\ln Q_{NPT} \tag{2.42}$$

The configurational integral for this ensemble is:

$$Z_{NPT} = \int \exp(-\beta PV)\mathrm{d}V \int \exp(-\beta U(\mathbf{r}))\mathrm{d}\mathbf{r} \tag{2.43}$$

and the average value of a configurational function is

$$< f >= \frac{\int_0^\infty V^N \exp(-\beta PV)\mathrm{d}V \int f(\mathbf{s}) \exp(-\beta U(\mathbf{s}))\mathrm{d}\mathbf{s}}{Z_{NPT}} \tag{2.44}$$

In this equation, $\mathbf{s} = \mathbf{r}/L$ are scaled coordinates, L is the side of the cube (the system is a cube), and V^N appears as the result of scaling. The probability density of states becomes proportional to $\exp(-\beta(U(\mathbf{s}) + PV) + N \ln V)$. Again, the Metropolis scheme is applied but for two moves: particle displacement and volume displacement.

Some authors (Eppenga and Frenkel 1984) found that it may be more convenient to change $\ln V$ in the simulation, rather than V. This has the advantage that all possible values of V_1 in configuration space can be achieved in the random walk. Also, the average step size in $\ln V$ is much less sensitive to the density. To adopt this method, the acceptance rule has to be slightly modified.

2.2.2 Gibbs ensemble Monte Carlo method

The Gibbs ensemble method of Panagiotopoulos (Panagiotopoulos *et al.* 1987, 1988) simulates fluid phase equilibria without an explicit interface when the temperature, pressure and chemical potentials of the coexisting phases are equal. Although the chemical potentials are equal, their absolute values are undetermined. (They can be easily computed in Grand Canonical MC by looking at the accept/reject rates for insertions and averaging $\exp(-\Delta U_+)$ from the insertion steps). It is the reason why this method can work. If these values were determined the system would not change, three parameters define the state unequivocally. The great benefit of the Gibbs method over the other ones is that, in it, the system spontaneously determines the parameters of the coexisting phases (pressure, densities and compositions). Many other methods of construction the coexistence line involve tedious work of computation the chemical potentials as a function of pressure for different compositions. The Gibbs ensemble Monte Carlo method is deficient when simulating dense phases of strongly interacting liquids and solids because of the poor performance of the insertion/deletion steps. Secondly, it is difficult to implement on parallel computers.

For direct simulation of first-order phase coexistence the Panagiotopoulos scheme can be taken (Frenkel and Smit 2002; Allen and Tildesley 1991) in which the total volume of the two adjacent boxes and the total number of particles in them remain constant, Fig. 2.3. That means, the total system is an *NVT* one. In this scheme, three types of trial moves are considered:

1. Random selection of a particle and its displacement.
2. Change of the volume of a box by ΔV and the volume of a box by $-\Delta V$.
3. Random selection of a particle and its transfer to another box.

Particle displacement

Assume that state *new* is obtained from state *old* via the displacement of a randomly selected particle in box 1. This is done using the following scheme:

1. Calculate the energy of the initial configuration U(old).
2. Select a particle at random and give it a random displacement. The value of the maximum displacement should be chosen such that the sampling is optimal. Consider a configuration with n_1 particles in box 1 with volume V_1 and positions $\mathbf{r}_1^{n_1}$.

Here the Metropolis acceptance rule is

$$\mathrm{acc}(\mathrm{old} \rightarrow \mathrm{new}) = \min\left(1, \exp\left\{-\beta[U(\boldsymbol{s}_{new}^{n_1}) - U(\boldsymbol{s}_{old}^{n_1})]\right\}\right). \qquad (2.45)$$

If the move is rejected, the old state is kept.

Volume Change

Here, as in *NPT* case, scaled positions are introduced: $\mathbf{s}^{n_1} = \frac{r_1^{n_1}}{V_1^{1/3}}$. For a change of the volume of the first box by an amount Δ*V*, $V_1 = V_1^{\text{old}} + \Delta V$, an acceptance rule is

$$\text{acc(old} \rightarrow \text{new) = min } \left\{1, \frac{(V_1)^{n_1}(V - V_1)^{N-n_1}}{(V_1^{\text{old}})^{n_1}(V - V_1^{\text{old}})^{N-n_1}} \exp\{-\beta[U(\mathbf{s}_{new}^N) - U(\mathbf{s}_{old}^N)]\}\right\} \qquad (2.46)$$

(Panagiotopoulos *et al.*, 1987, 1988). A better choice for generating a new configuration at this stage is to make a random change of $\ln[V_1/(V - V_1)]$ instead of in V_1 [Frenkel and Smit 2002]. Again, this has the advantage that the ergodicity of the process is improved in the random walk and the step size in ln*V* is much less sensitive to the density. The acceptance rule has to be slightly modified.

Particle Exchange

We remove a particle from box 1 and insert it in box 2. Thereby configuration *new* is generated from configuration *old.* An acceptance rule in this case is (there are n_1 particles in box 1)

$$\text{acc(old} \rightarrow \text{new) = min} \left\{1, \frac{n_1(V - V_1)}{(N - n_1 + 1)V_1} \exp\left\{-\beta[U(\mathbf{s}_{\text{new}}^N) - U(\mathbf{s}_{\text{old}}^N)]\right\}\right\} \qquad (2.47)$$

The implementation of particle displacement and volume change in Gibbs ensemble method is very similar to that in a normal *NVT* or *NPT* Monte Carlo simulation.

Simulation is performed in cycles. Every cycle consists of N_{part} (on average) attempts to displace randomly chosen particles in one of the randomly selected boxes, N_{vol} tries to change the volume of the boxes, and N_{swap} tries to swap particles between the liquid and gas boxes. The condition of microscopic reversibility must be fulfilled at each step of the simulation.

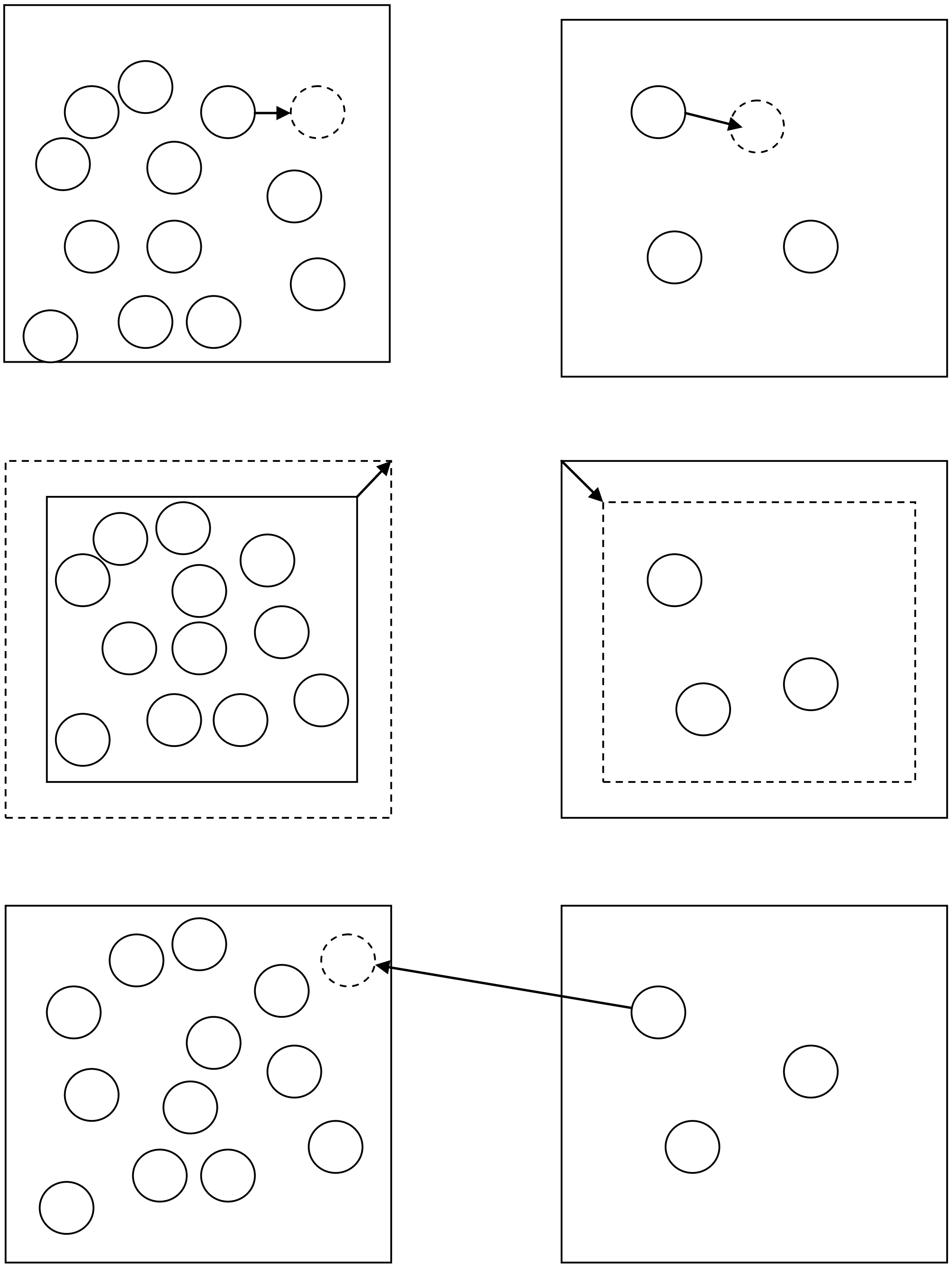

Figure 2.3. Monte Carlo trial moves in the Gibbs ensemble method: particle displacement, top, volume change, middle, and particle exchange, bottom.

As mentioned above, Gibbs ensemble MC also has a number of problems. Close to the critical point, the surface tension vanishes, so there is no penalty to form two phases in one box. The Gibbs ensemble MC is also not very accurate but its accuracy can be improved by building histograms $P(\rho)$ close to the critical point, and performing the simulations in μVT ensemble. Another problem is that close to the critical point the critical correlations (the density-density correlation length) become larger than the box length.

2.3 Cluster Counting

Clusters are intensively studied in phenomena where nucleation takes place, for example, condensation (Wedekind and Reguera 2007 and references therein). There are various definitions of a cluster. The most simple and intuitive one is due to Stillinger: a cluster is a group of atoms which fall within the range of r_0 from the central atom (Stillinger 1963). That definition of cluster has a disadvantage: moving atoms which approach a cluster closer than r_0 are taken as belonging to that cluster. This method can lead to a serious overestimation of the cluster size. ten Wolde and Frenkel modified the definition of Stillinger cluster (ten Wolde and Frenkel 1998; Wedekind and Reguera 2007). They supposed that in a liquid, a cluster has not less than five neighbours. They reject clusters with lesser number of neighbours with the usual Stillinger procedure and then apply that procedure to the remaining liquid clusters. This principle removes gas molecules which surround the cluster but neglects some particles at the surface of the cluster.

In literature, there are many definitions of a cluster but they are specific to phase transitions and not valid for fragmentation (Ellerby et al 1991; Senger et al 1999; Wedekind and Reguera 2007; and references therein). Fragmentation science is the study of fragments (clusters) and it is necessary to find an appropriate definition of them. Fragmentation process differs from phase transition. For example, there are many large fragments which consist of two or even three phases. Therefore, for description of a fragment it is naturally to accept the Stillinger definition of a cluster, although it is also not an ideal solution. In (Lee et al 1973) it was shown that the Helmholtz energy of Lennard-Jones cluster is almost independent on its definition at sufficiently low temperatures and provided that the definition is reasonable. The ten Wolde and Frenkel definition of a cluster could be of interest in the fragmentation theory for high temperatures when gases have low density and the gas molecules surrounding a liquid cluster can be counted as not belonging to the cluster.

Holian and Grady took the cluster bond length equal to the point of inflexion of the LJ potential. In that point, $d^2U/d^2r = 0$ and $r_0 = (26/7)^{1/6} \approx 1.244\sigma$. They used the Lindemann law as the criterion: when mean distance between the atoms at high temperatures becomes a few percent higher than that at normal temperatures, a solid melts. It was noted that use of that choice yields results which depend little on the potential truncation distance, whereas using r_0 equal to the potential cut off yields results which depend on it (Ashurst and Holian 1999). However, that dependence of the cluster behaviour is small. Ashurst and Holian found out that dependence truncating the LJ potential at 2, 2.5, and 4σ, and using the spline-approximated potential.

MD configurations can be sorted into clusters via the following computational algorithm:

- Initially every atom is considered as a cluster consisting of one atom.
- For each atom, a list of its neighbours is then made which contains atoms enclosed in a sphere of the radius r_0 centred on this atom.
- For each pair atom and its neighbour, one finds the maximum atom number and replaces it by the smaller number of this pair. That largest atom number is replaced by the smaller number also in other spheres.

Examples of clusters are given in Fig. 2.4.

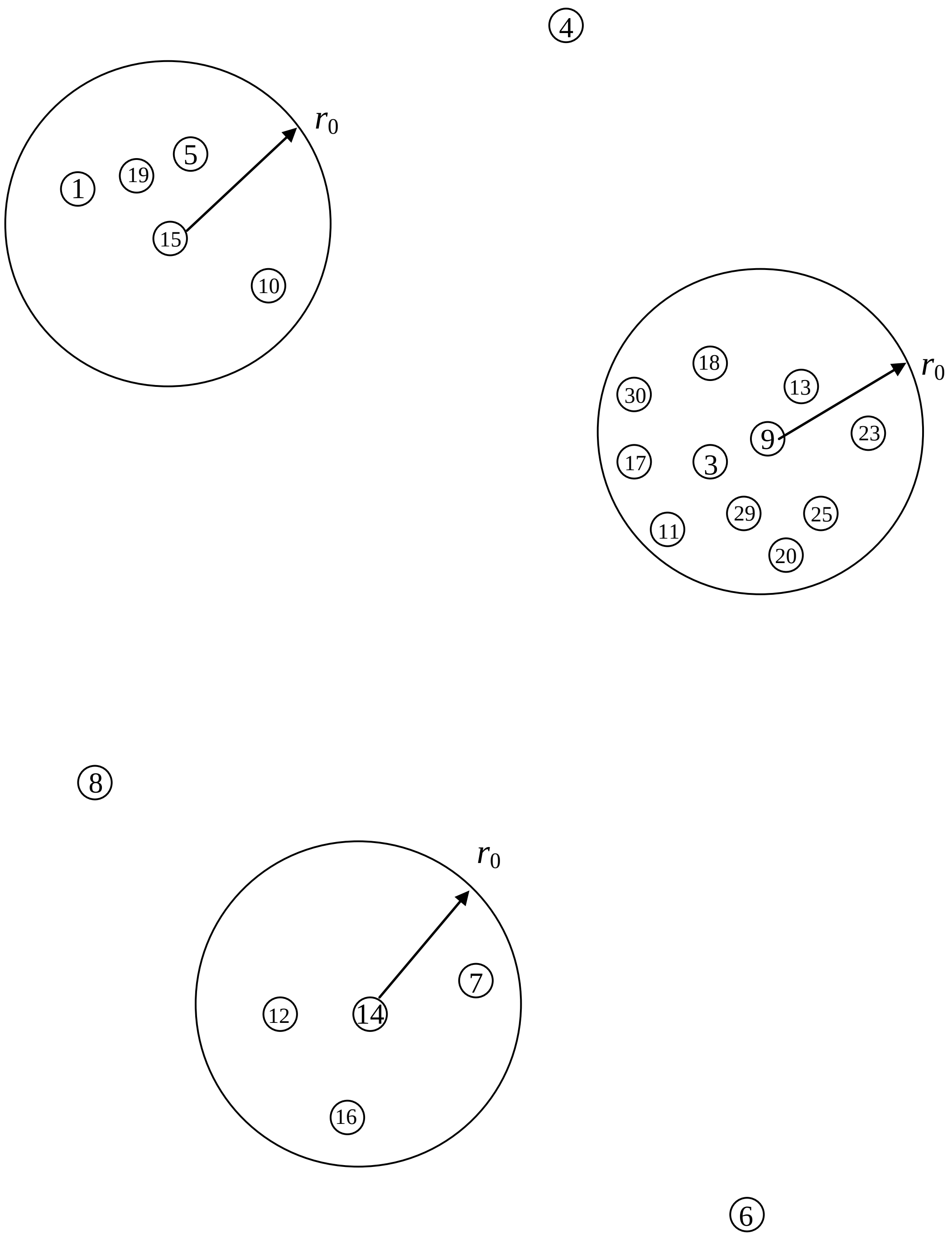

a)

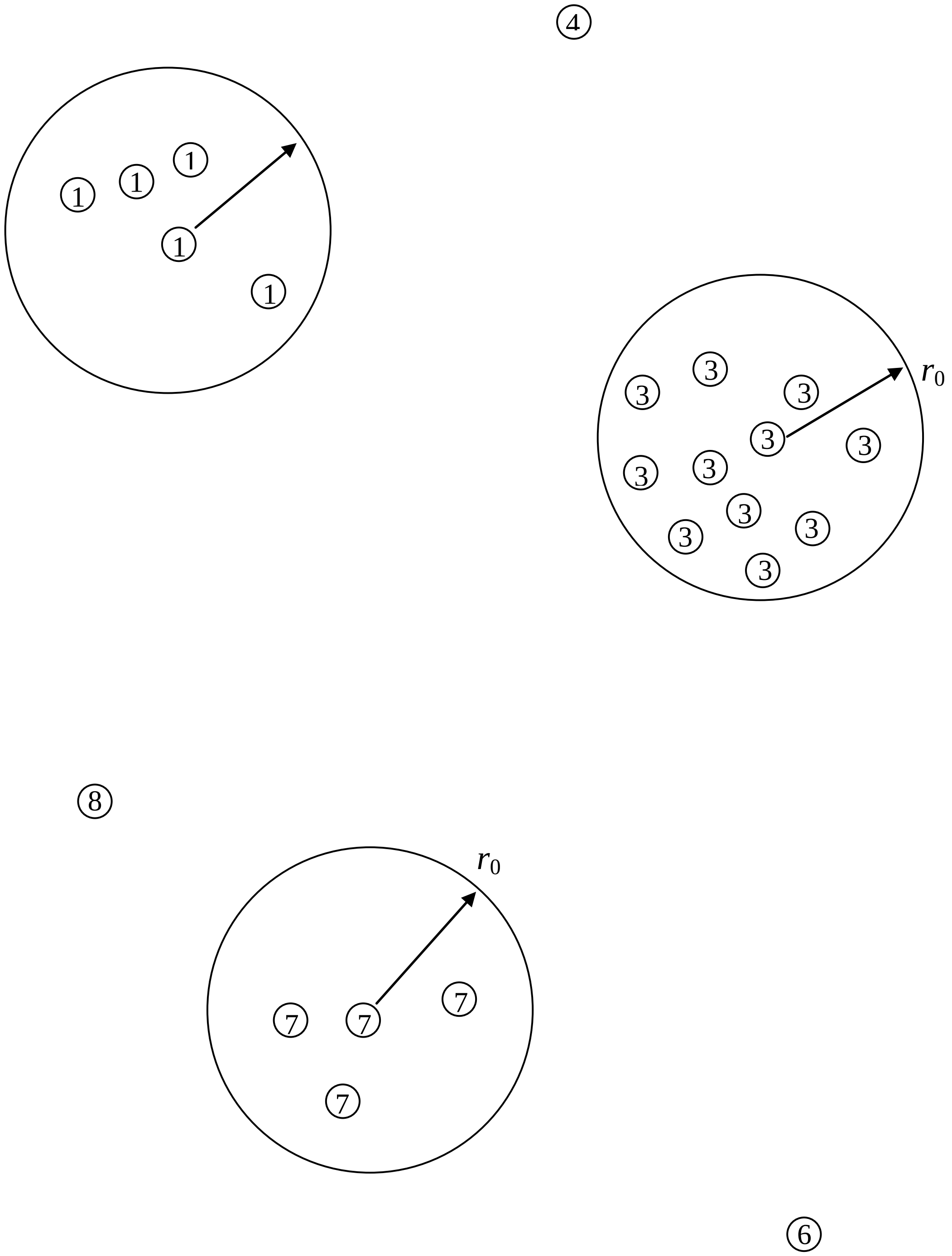

b)

Figure 2.4a,b. a) Stillinger clusters of atoms. Small circles are atoms and large circles are clusters of the size r_0. b) Their numeration in the Holian – Grady method.

2.4 Units

Henceforth LJ reduced units are used: $m^* = 1$, $r^* = r/\sigma$, $\rho^* = \rho\sigma^2$, $T^* = kT/\varepsilon$, $U^* = U/\varepsilon$, Helmholtz free energy $A^* = A/\varepsilon$, $P^* = P\sigma^2/\varepsilon$, heat capacity $C_V^* = C_V / \varepsilon$, speed of sound $c^* = c\sqrt{\frac{m}{\varepsilon}}$, and time $t^* = \frac{t}{\sigma}\sqrt{\frac{\varepsilon}{m}}$. Here star denotes a reduced unit but it will be dropped for sake of brevity.

Chapter 3

Phase Diagram of 2-Dimensional LJ-Spline Fluid

3.1. Introduction

A phase diagram comprises lines in ρ, T space for example, showing lines and points of coexistence between liquid and vapour, liquid and liquid, liquid and solid, solid and vapour, and solid and solid phases. A phase diagram is required in this work to decide on the initial heating levels (at what state point and in what phase to start the process) and to be able to track the thermodynamic path – does it for example cross a phase boundary? Phase diagrams can be constructed from the potentials by a variety of methods. One of the aims of this thesis is to build the phase diagram for the LJ-spline potential because we study fragmentation of liquids described by this potential. To the best of our knowledge, there is no published phase diagram for this potential.

3.2 Phase Diagrams in Two Dimensions

Phase behaviour of two-dimensional substances is of high interest for scientists. Quasi-two-dimensional systems are, for example, adsorption, liquid films and nanoconfined liquid films. It is important to know when the 2D-substance exists in solid, liquid and gas phases. The nature of two-dimensional melting remains an open and interesting question. Kosterlitz, Thouless, Halperin, Nelson, and Young (KTHNY) proposed a theory which suggested that the phase transition differs very much from that in ordinary three-dimensional systems (Strandburg 1988), (Kosterlitz and Thouless 1972, 1973), (Kosterlitz 1974), (Nelson and Kosterlitz 1977), (Nelson and Halperin 1979), (Young 1979). Many other theories, nevertheless, predict the usual first order transition of the same type as in three-dimensional (Strandburg 1988). A lot of experimental and theoretical work on the problem has been performed but the mechanism of two-dimensional melting remains unresolved.

KTHNY proposed that the melting occurs in two stages. The first one is a second-order transition from the solid (long-range positional order, long-range orientational order) to the hexatic phase (short-range positional order, quasi-long-range orientational order). The second one is a second-order transition from the hexatic phase into an isotropic phase (short-range positional and orientational order).

There are many simulations which contradict KTHNY. They produce the entropy change on melting and height of the first peak of the structure factor in agreement with the first order transition and show no hexatic phase. They also show a dramatic increase in the total number of dislocations as the system goes into the liquid phase whereas KTHNY predicts no change in that number. These are simulations on the Lennard-Jones system, and r^{-n} systems, for example, (Abraham 1980), (Ramakrishnan 1982), (Frenkel and McTague 1979), (Toxvaerd 1980). Binder *et al* (2002) found that for hard-disc fluid the possibility of the first-order phase transition cannot yet be completely ruled out.

Experiments on two-dimensional systems are very difficult. In spite of that, the experimental results are extremely interesting. In a number of systems apparent first order transitions have been observed, in some others indication for the hexatic to isotropic transition has been found. The number of systems that belong to the latter group continues to increase with improvement in experiments. For example, 2D colloidal systems support the KTHNY scenario (Gasser *et al* 2010).

In 1962, a solid – liquid phase transition in the two-dimensional hard-disk system was discovered (Alder and Wainwright, 1962). Since then, phase transitions in atomic systems with many different potentials have been studied by computer simulations. A two-phase coexistence region at a first-order phase transition in a constant density simulation evidences strongly of a first-order transition. However, it is difficult to distinguish a coexistence region from a hexatic phase. Strandburg, Zollweg, and Chester (Strandburg et al 1984) examined the local bond-orientation order for hard-disk and Lennard-Jones systems and showed a strong indication of a coexistence model.

It is also of importance to know whether the two-dimensional system is in a liquid, vapour or supercritical state. Many papers were devoted to study of that problem, for example, (Frenkel and Smit 1991), (Singh 1990), (Barker et al 1981). It has been found that the phase diagram and particularly the location of the critical point depend very substantially on the tail of the potential. The nature of the truncation is not that important for many bulk properties but for the liquid – vapour coexistence curves small changes in the tail result in a very large difference. The size effect (dependence on the system size) does not influence the binodal and the critical temperature much.

There are potentials which do not show liquid phase (Tejero et al 1994), (Hagen et al 1993), (Lekkerkerker et al 1992), (Frenkel 1999). In some of these papers sufficient and necessary conditions for existence of a liquid phase were worked out. If r_0 is the interatomic distance such that $r_0 \approx 1$ and $U(r_0)$ is a minimum and equal to -1, and r_1 is the distance such that $U(r_1) = -0.01$, then the liquid phase disappears at $1.05 < r_1 < 1.6$ (this are intermediate-range attractions) . For potentials with such r_1 (and shorter ones), one can accept, therefore, the existence of metastable binodal below the sublimation line. For the LJ potential, $r_1 \approx 2.6$ and this is a long-range attraction potential.

3.3 The Liquid-Vapour Dome

The liquid-vapour dome is a locus on a phase diagram (in ρ, T space, for example), showing coexistence between liquid and vapour phases. There are various simulation approaches to obtaining the liquid-vapour dome of a pure single component substance, for example, integration through the van der Waals loop (Hoover 2006), Gibbs ensemble Monte Carlo (Panagiotopoulos *et al.*, 1987, 1988), (Frenkel and Smit 2002), perturbation theory (Barker and Henderson 1967), (Henderson and Barker 1968), (Barker *et al.* 1981), Gibbs – Duhem integration (Kofke 1993a,b), quenched MD (Gelb and Muller 2002), histogram reweighting (Wilding 1995, 2001), (Potoff and Panagiotopoulos 1998), (Panagiotopoulos 2000), (Escobedo 2000), integration of subcritical isotherms (the same as integrating vdW loop) (Barker *et al.* 1981), etc. In our work, we use MD and Gibbs ensemble MC method.

3.3.1 Integration through vdW loop

At coexistence between two phases, one must have thermal, mechanical, and chemical equilibrium. That is, equality of temperature, pressure, and chemical potential (Gibbs energy per particle for pure substance):

$$P_1 = P_2,\ T_1 = T_2,\ \mu_1 = \mu_2, \tag{3.1}$$

where chemical potentials of phase 1 and phase 2 μ_1 and μ_2 equal G_1/N_1 and G_2/N_2 for pure phases.

Chemical potential can be obtained like this. From Maxwell relation,

$$\frac{\partial A}{\partial V} = -P \tag{3.2}$$

one gets

$$\frac{1}{N}\frac{\partial A}{\partial \rho} = \frac{P}{\rho^2} \tag{3.3}$$

Here A is the Helmholtz free energy per particle. From Eq. (3.3) one can derive

$$\frac{\beta A - \beta A_{\mathrm{id}}}{N} = \int_0^{\rho} \left(\frac{\beta P}{\rho} - 1 \right) \mathrm{d}\frac{P}{\rho} \tag{3.4}$$

where A_{id} is the Helmholtz free energy of the ideal gas. From Eq. (3.4), one obtains the Helmholtz free energy. The Gibbs energy per particle is obtained from

$$\mu \equiv \frac{G}{N} = \frac{A}{N} + \frac{PV}{N} = \frac{A}{N} + \frac{P}{\rho} \tag{3.5}$$

since $\frac{V}{N} = \rho^{-1}$.

The binodal can be constructed using the isotherms obtained from Eq. (3.4) by the minimisation method described in (Hoover 2006). To build the binodal with this method, one minimises the metric $\Delta P^2 + \Delta G^2$ where ΔP and ΔG are the differences in the pressures and the Gibbs energies (per one particle) between high and low density points on an isotherm. Low density equally spaced points are taken from the interval $\rho_1 \le \rho \le \rho_{\max}$and high density equally spaced points are taken from $\rho_{\min} \le \rho \le \rho_2$ (subscripts min and max correspond to the local minimum and maximum of the curve, respectively). The minimum of the metric occurs at ρ_i and ρ_k; ρ_i belongs to the first interval and ρ_k to the second one. These density points closely satisfy the above phase equilibrium conditions, Eq. (3.1).

Let us consider a simple case, the van der Waals equation of state in reduced units:

$$P_{\mathrm{r}} = \frac{8\rho_r T_{\mathrm{r}}}{3-\rho_r} - 3\rho_r^2 \qquad (3.6)$$

where $T_{\mathrm{r}} = T/T_{\mathrm{c}}$, $\rho_{\mathrm{r}} = \rho/\rho_{\mathrm{c}}$ and $P_{\mathrm{r}} = P/P_{\mathrm{c}}$ (T_{c}, ρ_{c} and P_{c} are the critical values). aTypical isotherms generated from Eq. (3.6) are shown in Fig. 3.1. Rearranging Eq. (3.6), we have

$$\rho^3 - 3\rho^2 + \rho\frac{8T+P}{3} - P = 0 \qquad (3.7)$$

where we dropped the subscript 'r' for clarity. The form of Eq. (3.7) makes it clear this is a cubic equation of state.

To use the metric minimisation method, we find the pair of densities ρ_{liq}, ρ_{vap} which minimises the metric: $(\Delta P)^2 + \left(\frac{\Delta G}{N}\right)^2$. The Gibbs energy of the van der Waals system per atom is given by

$$G = -\frac{8T}{3}\ln\left(\frac{3}{\rho} - 1\right) + \frac{8T}{3-\rho} - 6\rho + \varphi(T) \qquad (3.8)$$

where $\varphi(T)$ is a constant of integration and a function of T only.

One scans a series of ρ's on the vapour side and a series of ρ's on the liquid side, computes the metric above and finds the ρ's which minimise it. To determine the ρ's belonging to each phase we

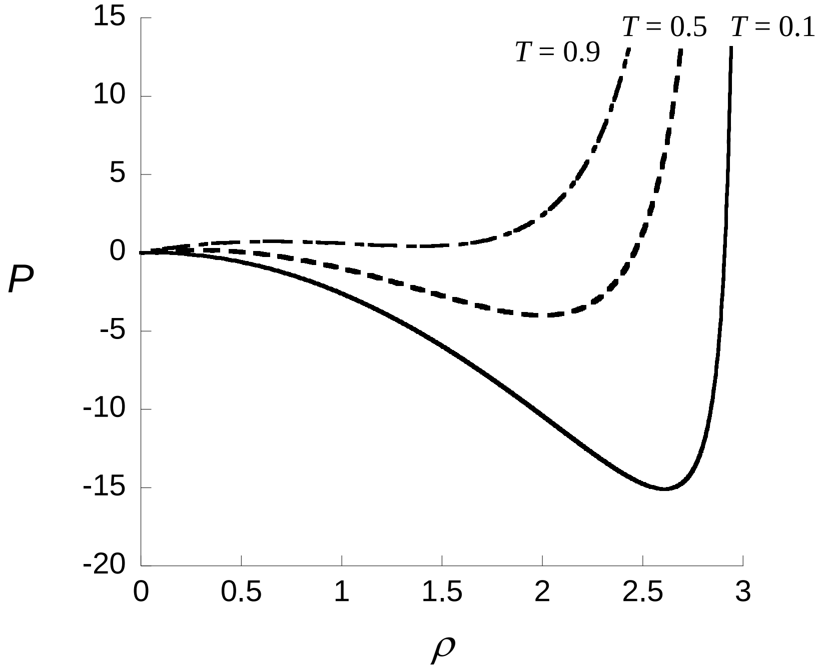

Figure 3.1. $P - \rho$ isotherms for the two-dimensional van der Waals fluid. Solid line, $T = 0.1$, dashed line, $T = 0.5$, dash-dotted line, $T = 0.9$.

find the local maxima and minima in the van der Waals equation, $\left(\frac{\partial P}{\partial \rho}\right)_T = 0$. These are solutions of the cubic equation:

$$\rho^3 - 6\rho^2 + 9\rho - 4T = 0 \qquad (3.9)$$

Then $0 < \rho < \rho_{\max}$ is vapour and $\rho_{\min} < \rho < 1$ is liquid (the critical density equals 3).

In addition, the spinodal curve may be obtained analytically. Along a spinodal, both the equation of state and $\frac{\partial P}{\partial V} = 0$ must be satisfied (Debenedetti 1996). Solving gives

$$T = \frac{\rho}{4}(3 - \rho)^2 \tag{3.10}$$

Plotting the numerically obtained binodal and analytically obtained spinodal together, gives Fig. 3.2.

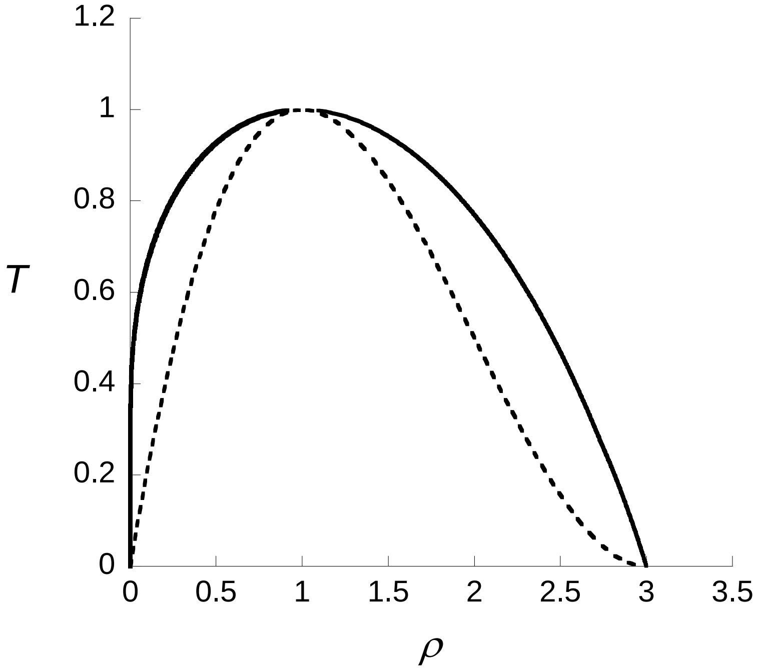

Figure 3.2. Binodal and spinodal of the two-dimensional van der Waals fluid. Outer curve, binodal, inner curve, spinodal. The left curve corresponds to vapour and the right curve to liquid.

3.3.2 Application of MC or MD

An isotherm can be obtained by a sequence of MC or MD simulation in an *NVT* ensemble (Chapter 3) equally spaced in $\Delta\rho$ from ρ_{min} (say 0.01) to ρ_{max} (say 0.8), or from an equation of state. The process of generating isotherms *P*(*V*) in our work was automated using a Perl script. One can also work in an *NPT* ensemble and compress a starting vapour or expand a starting solid.

3.3.3 Gibbs ensemble route

As mentioned in the Introduction, the phase diagram for LJ-spline fluid has not been obtained yet. We have attempted to obtain the liquid-vapour dome for this fluid in two dimensions by Monte Carlo simulations with the Gibbs ensemble method described in Chapter 3.

Calculations were carried out for *N* equal and much greater than 333 atoms. At the beginning, they were randomly distributed between the liquid and gas boxes, and placed at random in each box. In one cycle, we performed on average *N* atom moves, one volume change and 1 – 60 atom swaps. The range of densities studied was from 0.01 to 0.85. The number of cycles was from 10 000 to 12 000, the number of equilibration cycles was 3000 – 6000. The atom displacement sizes in the liquid and gas phases were adjusted such that approximately every second displacement was accepted. Approximately, every third volume move and every hundredth or tenth atom swap were accepted. It is an empirical rule in the Gibbs ensemble method (Panagiotopoulos *et al.*, 1987, 1988), (Harris and Yung 1995). The average number of atoms in the gas box was between 20 and 200. The simulation was stopped when the system equilibrated, that is the dependence of the boxes' volumes, numbers of atoms, densities, energies per atom, and pressures on the number of steps exhibited a plateau. Also, the pressures in the both boxes must be equal.

In Figs. 3.3 and 3.4 we give some details of a typical Gibbs MC simulation at $T = 0.4$ for $N = 333$. In Fig. 3.3 an example of unsuccessful simulation is given: it failed to converge and there are two phases in the liquid box: solid one and vapour one. The triple point must be a little higher than $T = 0.4$. Indeed, the phase diagram in Fig. 4.26 suggests that the triple point temperature is about 0.4. A probable reason could be insufficient equilibration. It is not that easy to achieve a proper convergence in the Gibbs method. Liquid in the liquid box can partly turn to vapour (or to solid) due to low interfacial tension of the two-dimensional liquid (Smit and Frenkel 1991). It can happen in the three-dimensional box but it is more pronounced in two dimensions. The vapour box of this simulation is shown on Fig. 3.4. Estimation of the triple point for similar 2D LJ fluids is given in Table 3.1. The results are close what should be expected.

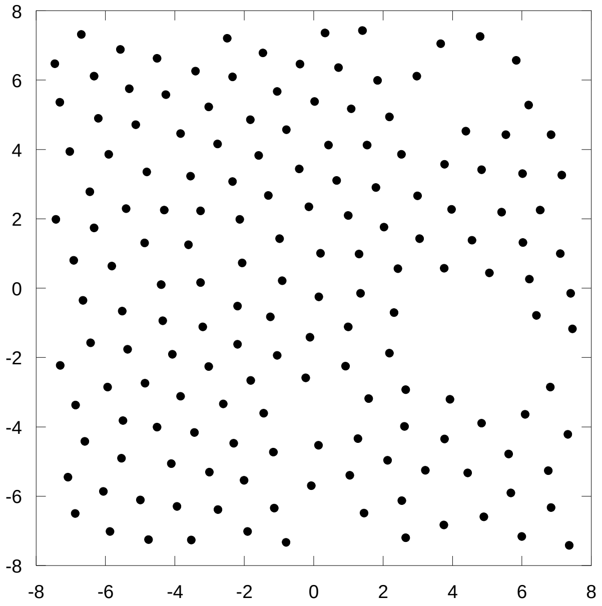

Figure 3.3. Final configuration in the liquid box in Monte Carlo Gibbs ensemble simulation at T = 0.4. LJ-spline fluid. Unsuccessful attempt. One can observe sublimation (solid – vapour coexistence). The triple point must be a little higher than T = 0.4.

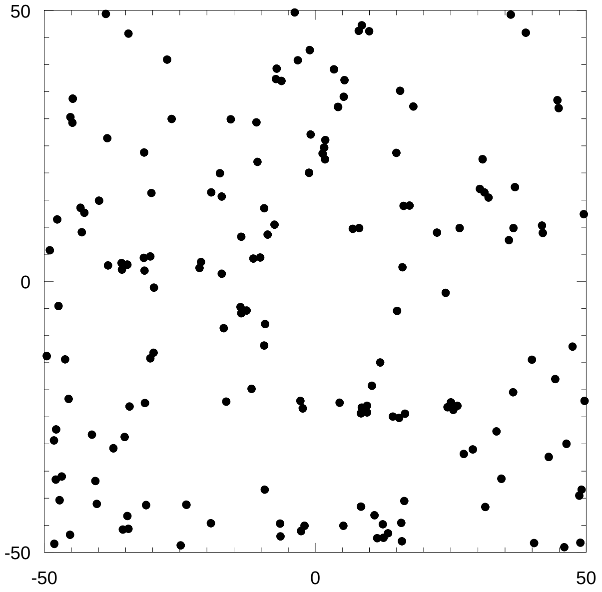

Figure 3.4. Final configuration in the vapour box in Monte Carlo Gibbs ensemble simulation at *T* = 0.4. LJ-spline fluid. Unsuccessful attempt.

Table 3.1. Estimation of the triple point location for the 2D LJ systems

Method	T^*_{triple}	**References**
MD simulation	0.41	(Toxvaerd 1980)
MC simulation	0.40	(Vanswol *et al* 1980)
Perturbation and cell theories	0.41	(Barker et al 1981)
MC simulation	0415	(Barker et al 1981)
MC simulation	0.4	(Pillips et al 1981)

A successful simulation for the same temperature but with 666 particles is given in Figs. 3.5 and 3.6.

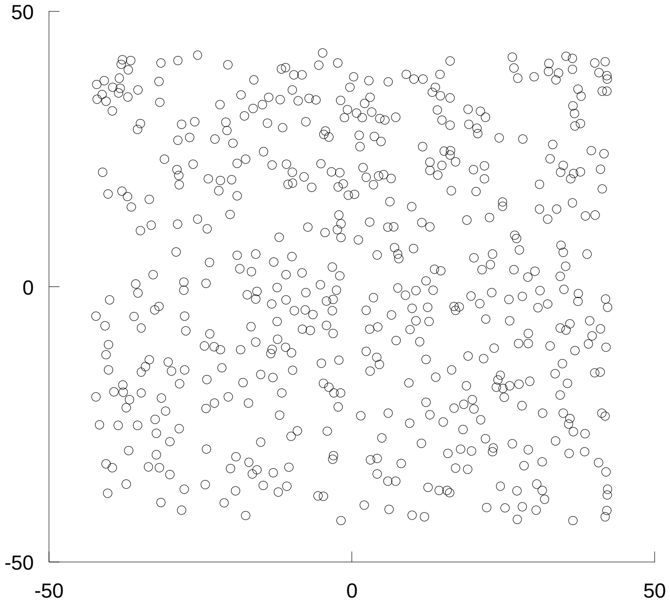

Figure 3.5. Liquid box, *T* = 0.4. LJ-spline fluid. 522 particles.

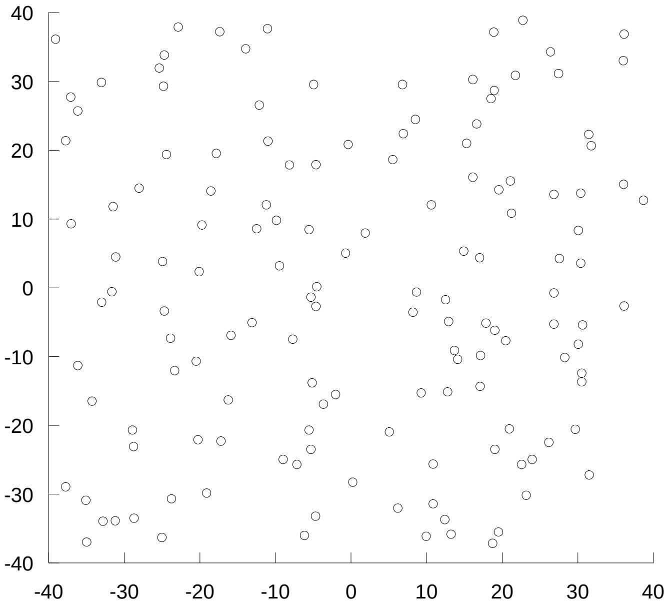

Figure 3.6. Vapour box, *T* = 0.4, LJ-spline fluid, 144 particles.

The resulting binodal of the two-dimensional LJ-spline fluid is given in Fig. 3.7. This curve was determined with large statistical uncertainties. That top is very flat which is in agreement with other authors (Smit and Frenkel 1991). This flatness cannot be described by an equation of state. The part of the binodal below $T = 0.4$ is unreliable because the substance for these temperatures is a melting solid, Fig. 3.8 and Gibbs ensemble simulations for it are not efficient. One can suggest that the critical point for this fluid is: $T_c \approx 0.45 – 0.47$ and $\rho_c \approx 0.4$. These results are close to those for similar 2D LJ fluids what should be expected, Table 3.2.

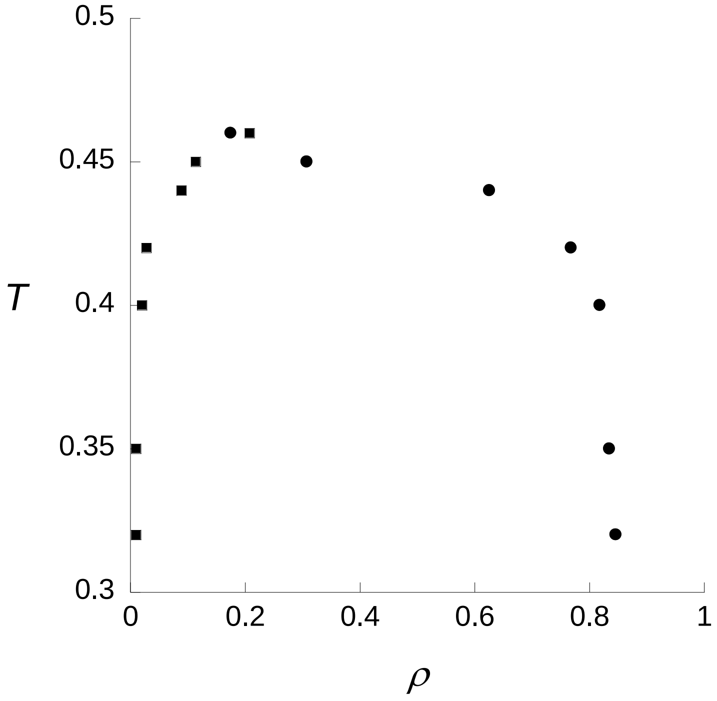

Figure 3.7. Binodal of the two-dimensional LJ-spline fluid obtained by Gibbs ensemble Monte Carlo simulations in this work. The triple line is about $T = 0.4$. The critical point is: $T_c \approx 0.45 – 0.47$ and $\rho_c \approx 0.4$.

Table 3.2. Estimation of the location of the critical point for the 2D LJ fluid

Method	T_c^*	ρ_c^*	**References**
MC and Equation of State	0.533	0.335	(Barker et al 1981)
MC simulation	0.537	0.365	(Reddy and O'Shea 1986)
MC simulation	0.472	0.33	(Singh et al 1990)
Gibbs Ensemble MC (truncated potential)	0.515	0.355	(Smit and Frenkel 1991)
Gibbs Ensemble MC (truncated and shifted potential)	0.459	0.35	(Smit and Frenkel 1991)
Molecular dynamics	0.47	0.35	(Rovere et al 1993)
Gibbs Ensemble MC	0.497	0.35	(Panagiotopoulos 1994)
Gibbs Ensemble MC	0.498	0.36	(Jiang and Gubbins 1995)

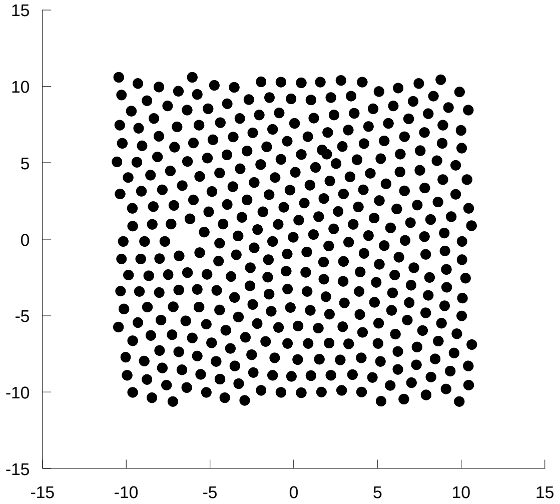

Figure 3.8. A snapshot of particle positions in a Gibbs Ensemble MC simulation of LJ-spline fluid for $T = 0.35$.

Panagiotopoulos (1994) found that the size effects in Gibbs ensemble simulations of LJ two dimensional systems were small far from the critical point but becomes large close to it. We also found that increasing of the number of particles from 300 till 600 did not play any role far from the critical point but close to it we had to increase the number of atoms a few times because otherwise all particles moved to one box. In doing the simulation, some problems were encountered, for example, a box becomes empty, flipping of box identities, large errors near the critical point. To remedy them we increased N, the number of swaps and the number of steps.

3.3.4 Gibbs – Duhem integration

Another method is Gibbs – Duhem integration (Kofke 1993a,b) which is thermodynamic integration of the Clapeyron equation along the saturation line. It allows coexistence to be determined by a single simulation (however, one has to perform many auxiliary simulations in the course of the simulation). It provides a good accuracy over the entire range of densities. This method requires, however, knowing one coexistence point in advance. A big advantage of this method is that it does not perform particle insertions, which is a serious drawback in the Gibbs ensemble method for dense substances, and, therefore, can be applied to phase coexistence between any two phases.

On the other hand, Gibbs-Duhem method is not suitable for study of a single state points; it produces an entire coexistence curve. One starts the integration of the Clapeyron equation from the initial state point. One chooses a temperature step and the saturation pressure is estimated after one step. Simultaneously, NPT MD or MC simulations are performed at this new temperature (they produce the volume change and enthalpy change). A new pressure is produced and the simulation is repeated with this new pressure until the convergence. The process is repeated after the new temperature step at many points along the integration line. The Clapeyron equation has the following form:

$$\frac{\mathrm{d}P}{\mathrm{d}T} = \frac{\Delta S}{\Delta V} = \frac{\Delta H}{T\Delta V} \qquad (3.11)$$

Here ΔS is the change in the entropy and ΔH is the change in enthalpy. If one of the phases is dilute, it is convenient to write Eq. (3.11) slightly different (Frenkel and Smit 2002):

$$\frac{\mathrm{d}\ln P}{\mathrm{d}1/T} = -\frac{T\Delta H}{P\Delta V} \tag{3.12}$$

The advantage of this is that one can take relatively large steps in $1/T$ which correspond to small steps in T. Dr. Travis wrote a Kofke code which uses *NPT* Molecular Dynamics for two phases with an RK4 integrator. The Kofke code is written in Perl, a high level scripting language. It solves the equation $\frac{\partial y}{\partial x} = f(x,y)$ and selects x and y based on Eqs. (3.11) or (3.12), and can integrate with increasing or decreasing x. We tested our code producing the van der Waals binodal and comparing with the binodal obtained from the equation of state, Fig. 3.9. An excellent agreement was found. We also tested it out using Eqs. (3.11) and (3.12). Again there was a complete coincidence of the curves, Fig. 3.10. The starting point was the critical point of the van der Waals fluid.

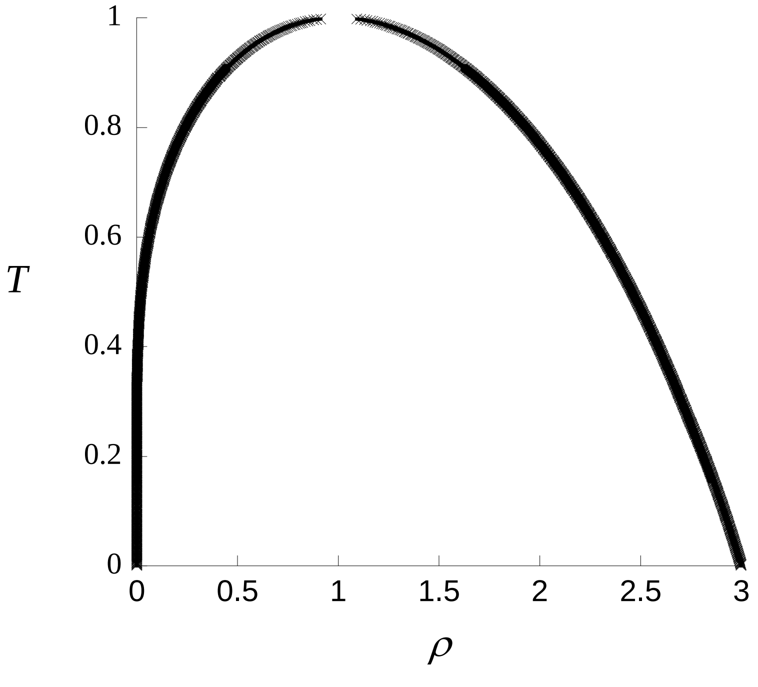

Figure 3.9. The binodal of the van der Waals fluid obtained with Kofke integration (crosses), and the one from Fig. 3.2 obtained from the equation of state (line).

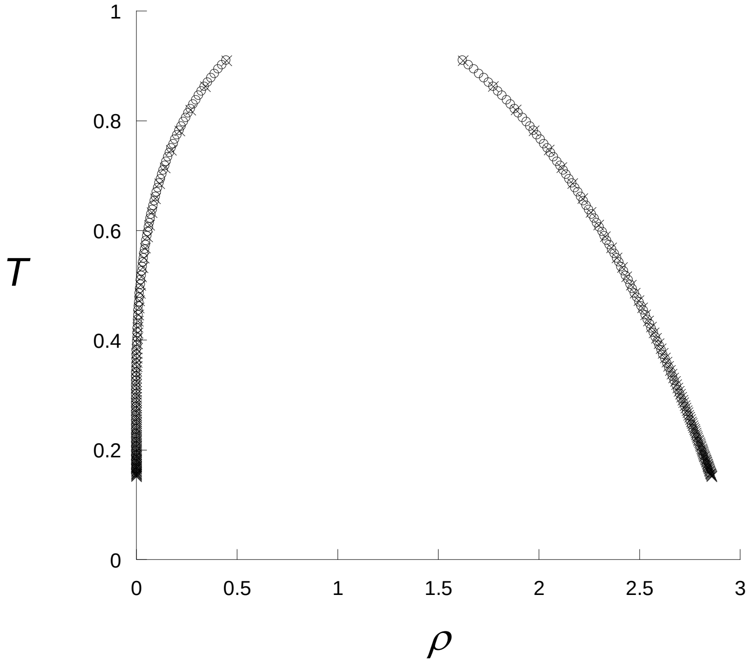

Figure 3.10. The binodal of the van der Waals fluid obtained in our work using Eq. (3.11), circles, step size in *T* is 0.008, and Eq. (3.12), crosses, step size in 1/*T* is 0.06.

We obtained the binodal of the two-dimensional LJ-spline fluid by the Kofke method. It is presented in Fig. 3.11 and shows a reasonable agreement with that obtained with the Gibbs ensemble Monte Carlo simulation. One can conclude that the critical point for that liquid is somewhere around $T = 0.45$ and ρ is around 0.4. The agreement of Kofke method with MC one is good for the temperatures less than 0.4 (approximate position of the triple line). Integration through the triple line decreases the accuracy of results. Comparing these results with Table 3.2 one can see that, in general, the critical temperature for closely related LJ systems is higher but the critical density lower. The binodal top in our simulation is also very flat.

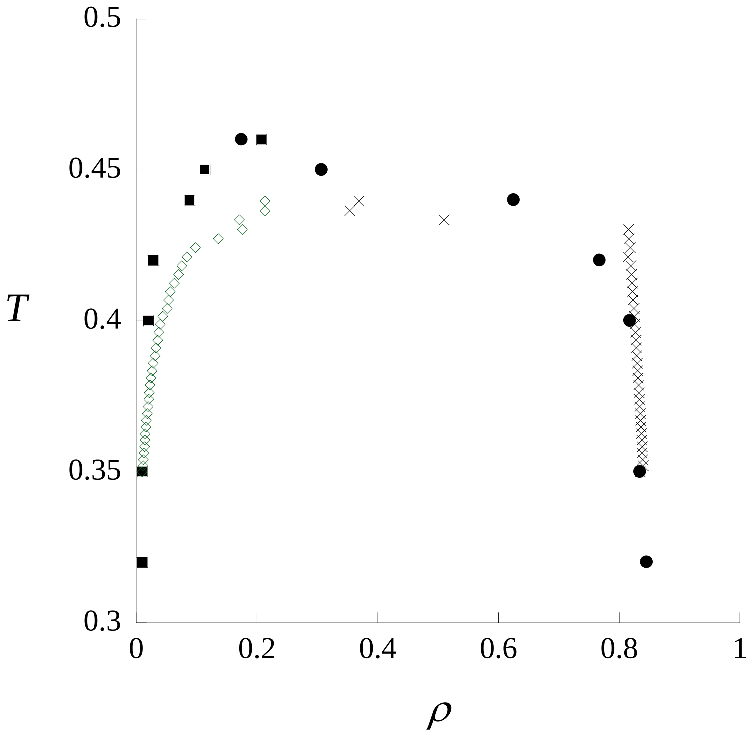

Figure 3.11. Binodal of the two-dimensional LJ-spline fluid obtained by Kofke method in this work (diamonds and crosses) compared to that obtained by Gibbs ensemble Monte Carlo (filled symbols). Triple line is about $T = 0.4$.

In Fig. 3.12 we show the same simulation by the Kofke method but starting from the point $T = 0.4$. One can see that the simulation fails at $\rho \approx 0.4$. Other authors who obtained the binodal for LJ fluids with Gibbs-Duhem integration, for example, Lisal and Vacek (1996), halted their integration near the critical point because the liquid phase turned to vapour-like phase in that region. This is unavoidable in the NPT MD simulation. Their result for a two-centre LJ fluid is given in Fig. 3.13. However, our result in Fig. 3.12 is still not good enough probably due to imperfection of our programming method.

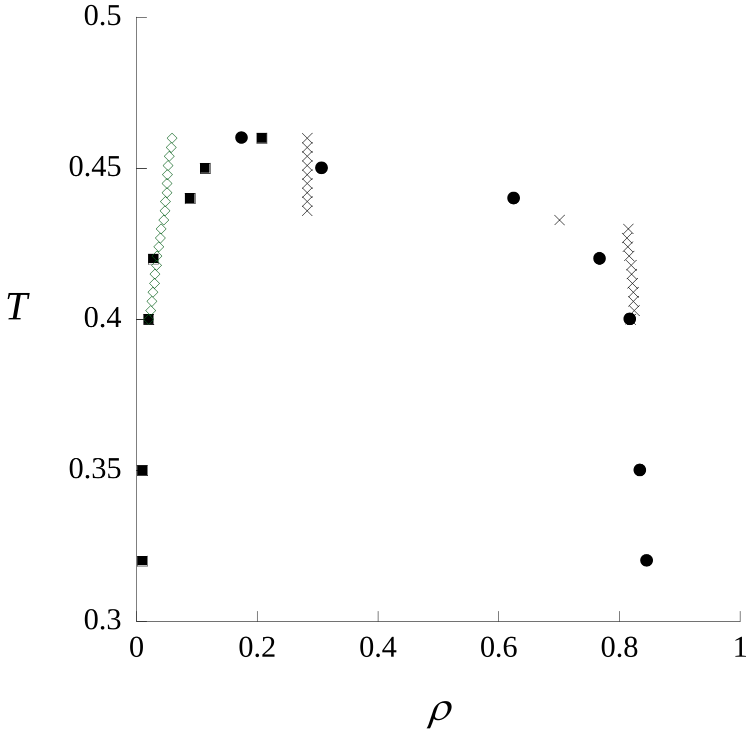

Figure 3.12. Same as in Fig. 3.11 but the Kofke simulation starts from the point *T* = 0.4.

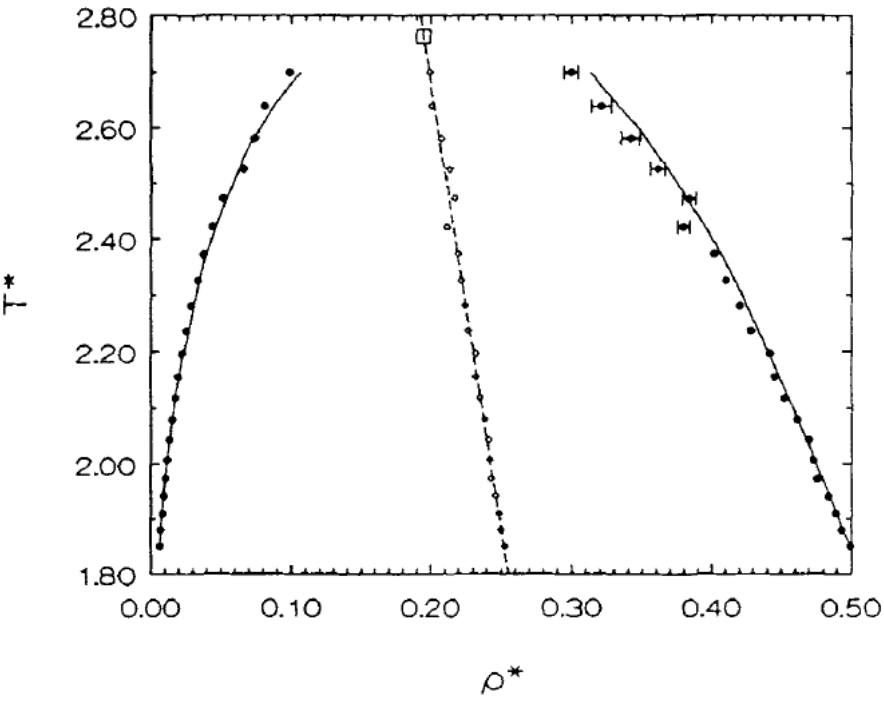

Figure 3.13. Binodal for the two-centre LJ fluid obtained by Kofke method (Lisal and Vacek 1996).

3.3.5 Other methods

There are alternative ways to get the liquid-vapour dome. A new and very promising one is the histogram reweighting technique (Wilding 1995, 2001), (Potoff and Panagiotopoulos 1998), (Panagiotopoulos 20000), (Escobedo 2000). The idea of this method is that histograms of physical quantities accumulated at one set of system parameters can be reweighted to produce histograms for another set of parameters. Application of this technique greatly improves the accuracy of MC simulations especially close to the critical point where large fluctuations occur. The histogram reweighting requires a few MC simulations with grand canonical ensemble instead of one in the Gibbs ensemble and for accurate determination of the critical parameters must be combined with finite-size scaling technique. Using finite-size scaling theory one can extract the infinite-volume critical point by performing a number of studies with increasing system size. Histogram reweighting has been applied in systems where the location of the critical point was estimated earlier.

Quench MD is another method to locate phase coexistence points (Gelb and Muller 2002). During the equilibration under *NVT* conditions, the temperature is dropped into a two-phase region, and the system separates into domains of two coexisting phases. Every domain is locally equilibrated and it is not necessary to achieve the global equilibrium of the system which results in a huge savings of computational time. This method has a drawback though: interfaces in small systems are bad.

The method can be used to locate more types of phase equilibrium (vapor–liquid, liquid–liquid or solid–fluid) and to study more complex molecular species than other approach. It is very well suited to the determination of phase equilibria in systems about which little is known. It is faster than any other competing technique. Using it, one can determine the location of critical points or lines with a good accuracy, however, histogram reweighting method methods are more precise.

3.4 Solid – Liquid Coexistence

3.4.1 Introduction

Solid – fluid and solid – vapour curves can be obtained by direct simulation of the coexisting phases in the same box by MD (Ladd and Woodcock 1977, 1978). This is a successful route to the phase diagram if the equations of state of every phase are known. Using them one can find the parameters of the Lennard-Jones potential for every phase.

There is also thermodynamic integration (Hoover and Ree 1967), (Hoover et al 1971), (Frenkel and Ladd 1984), (Frenkel and Smit 2002). It requires the absolute free energies of the solid and liquid which can be obtained via the methods of the above authors. In thermodynamic integration, one considers a reversible path from the solid phase under consideration to an artificial state of known free energy.

There are other methods of obtaining a melting point and melting line: perturbation theory (Barker and Henderson 1967), (Henderson and Barker 1968), (Barker *et al.* 1981), direct simulation of liquid and solid – moving interface method (Voller and Cross 1981). The former is treating the substance as a hard-sphere system with attractive forces as a perturbation. In (Barker *et al.* 1981) it was adapted to 2 dimensions. The two-dimensional Lennard-Jones fluid is a good model for physisorbed gases, where gas-substrate interactions may be considered as a perturbation.

Hoover and Ree introduced the single occupancy cell method for simulating solids (Hoover and Ree 1967). They consider a lattice gas with one particle per lattice cell. At high densities this gas turns to a solid and at low densities it is an ideal gas which free energy is known. The free energy of the solid at a given temperature is then obtained from the equation

$$F_{\text{solid}}(V_2) - F_{\text{gas}}(V_1) = -\int_{V_1}^{V_2} P(V)\mathrm{d}V \qquad (3.13)$$

That method is not reliable because there is an evidence of a phase transition when the interactions between particles take over from the cell walls. In that case, the path from the solid to the gas may be not reversible. However, it is acceptible for calculation of the absolute free energy of the hard-sphere and hard-disk solids.

Hoover and co-authors developed the harmonic-lattice method in 1971 (Hoover et al 1971). They use the harmonic solid, the free energy of which can be computed exactly. This method is applicable only to solids which are harmonic at low temperatures and/or high densities. This excludes systems with discontinuous potentials. Also, solids that are unstable at low temperatures cannot be studied by this method. Another problem is that it involves lengthy computation.

Helmholtz energy can be calculated by quasi-harmonic lattice-dynamic method (Ree and Holt 1973). This method is especially powerful when the anharmonic contributions are small but not necessarily of quantum mechanical nature. One expands the total potential energy of a system of atoms each interacting via the given potential in a Taylor series in displacements of the atoms from their equilibrium positions. Then one truncates the series after the quadratic term. The resulting series consists of the constant zero-point-temperature lattice energy term, E_0, and the quadratic term. The linear term drops out because of the crystal symmetry. The resulting equations of motion can be diagonalized using the periodic boundary condition. This gives $3N – 3$ normal-mode frequencies ν_i. Because in this calculation the vibrational characteristics of the crystal are volume and strain dependent, the method is called quasi-harmonic.

The Voller-Cross method is solving Navier-Stokes equations for a deforming phase boundary which is very difficult. For calculating fluid – solid coexistence one can also utilize Gibbs-Duhem integration described in §3.3.4. As mentioned earlier, it is very suitable for dense substances.

3.4.2 Free energy route

Thermodynamics of solid-liquid coexistence is also governed by Eqs. (3.1). In this method, one solves the pair of simultaneous equations for coexisting densities:

$$P(\rho_{\text{liquid}}) = P(\rho_{\text{solid}}) \tag{3.14}$$

$$\mu(\rho_{\text{liquid}}) = \mu(\rho_{\text{solid}}) \tag{3.15}$$

The temperatures are equal in the both phases, $T_{\text{liquid}} = T_{\text{solid}}$. The problem involved here is one cannot avoid a liquid – vapour phase transition unless one goes for $T > T_c$.

Helmholtz free energy of fluid is obtained from integrating the equation of state, $P(\rho)$, Eq. (3.3), to states of zero density (ideal gas limit). Helmholtz free energy of solid is obtained by Frenkel – Ladd method – connect system to Einstein crystal, whose free energy is known. The Gibbs free energy per particle is obtained from it by Eq. (3.5). The equation of state, $P(\rho)$, is still necessary for solid branch.

3.4.3 Method of Frenkel and Ladd

Frenkel and co-authors proposed the most comprehensive method to compute the absolute free energy of a solid phase (Frenkel and Ladd 1984), (Frenkel and Smit 2002). They construct a reversible path to the reference state, which is an Einstein crystal with the same structure as the solid phase. Therefore, it is very likely that there will be no phase transitions along the path and it will be reversible. The free energy of an Einstein crystal can be easily found. Frenkel and co-authors added a coupling term to the unperturbed potential energy U_0, such that

$$U = U_0 + (1-\lambda)(U - U_0) + \lambda \sum_{i=1}^{N} \alpha \left(\mathbf{r}_i - \mathbf{r}_i^0\right)^2 \tag{3.16}$$

where U is the potential energy of the solid, U_0 is its potential energy when all atoms are at their equilibrium sites, λ is the thermodynamic coupling parameter $(0 \le \lambda \le 1)$, α is the spring constant of the Einstein crystal, and $\mathbf{r}_i^0$ is the equilibrium position of the particle i. For $\lambda = 0$, we get the original interactions between atoms described by U. For $\lambda = 1$, the intermolecular interactions are switched off, except for the constant term U_0, and the system transforms to the Einstein crystal.

In statistical mechanics, the Helmholtz free energy A is defined as

$$A = -kT \ln Q \tag{3.17}$$

where Q is the partition function. The derivative of the free energy of the solid phase with respect to λ is given by

$$\left(\frac{\partial A}{\partial \lambda}\right)_{N,V,T} = -kT \frac{\partial}{\partial \lambda} \ln \int \ldots \int \exp\left(-\frac{U(\lambda)}{kT}\right) \mathrm{d}\mathbf{q}^N = \left\langle \frac{\partial U(\lambda)}{\partial \lambda} \right\rangle_\lambda \tag{3.18}$$

Now it is easy to calculate the free energy of the real crystal knowing only the free energy of the Einstein crystal:

$$A(\lambda = 0) = A(\lambda = 1) - \int_0^1 \left\langle \frac{\partial U(\lambda)}{\partial \lambda} \right\rangle_\lambda \mathrm{d}\lambda \tag{3.19}$$

The integrand can be calculated directly in the simulation. In our case, Eq. (3.18) turns to

$$A = A_{\mathrm{Ein}} + \int_1^0 \left\langle \frac{\partial U(\lambda)}{\partial \lambda} \right\rangle_\lambda \mathrm{d}\lambda = A_{\mathrm{Ein}} + \int_1^0 \left\langle \sum_{i=1}^N \alpha \left(\mathbf{r}_i - \mathbf{r}_i^0\right)^2 - (U - U_0) \right\rangle_\lambda \mathrm{d}\lambda \tag{3.20}$$

The configurational free energy of the Einstein crystal is

$$A_{\mathrm{Ein}} = -\frac{D}{2\beta} \sum_{i=1}^N \ln \frac{\pi}{k\beta} \tag{3.21}$$

where D is the dimensionality. It is computationally more efficient to use a crystal with fixed centre of mass. This will result in a small modification of Eq. (3.20): a term $-kT \ln\left(\frac{\beta^2 \alpha}{4\pi^2}\right)^{D/2}$ is added on the right hand side. The method of Frenkel and co-authors is fast and accurate and can be applied to all types of interactions.

3.5 Calculation of Virial Coefficients

The parts of phase diagrams corresponding to low and moderate densities (where interactions between the particles are sufficiently weak) can be successfully calculated using virial coefficients which characterise contributions of two-body, three-body, four-body, etc, interactions. For strong interactions computer simulations are necessary. Nevertheless, a few-term approximation to the virial expansion is feasible for simple potentials and leads to satisfactory agreement for fluids even close to the critical point.

3.5.1 Second virial coefficient

The second virial coefficient B_2 is calculated by the formula

$$B_2(T) = -\frac{1}{2}\int_0^{R\mathrm{cut}} \left[\exp\left(-\beta U(r)\right) - 1\right] \mathrm{d}r \qquad (3.22)$$

We applied Gauss-Legendre metod (Griffiths and Smith 1991) and 5000 divisions were made in the integration. The coefficient B_2 for LJ-spline potential is plotted in Fig. 3.14.

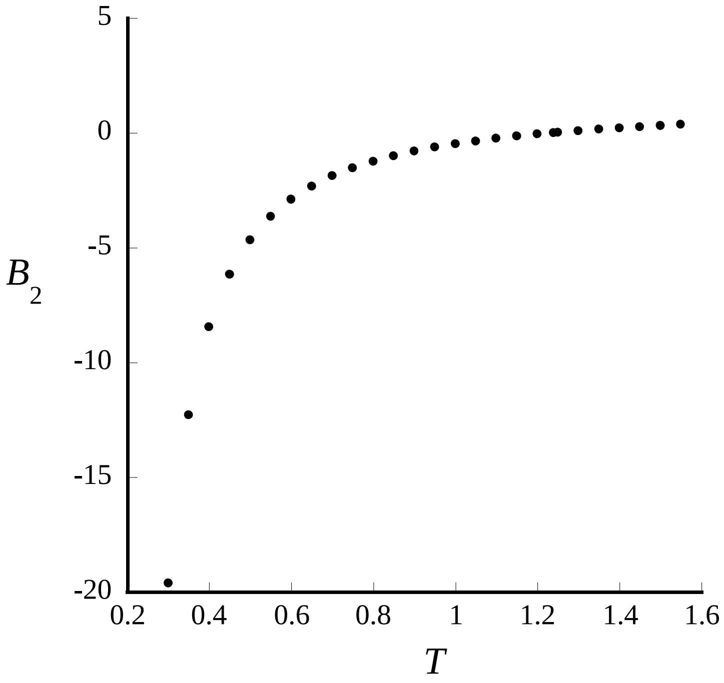

Figure 3.14. Dependence of the second virial coefficient B_2 for LJ-spline potential on the temperature.

3.5.2 Third virial coefficient

Calculation of the 3rd virial coefficient B_3 for LJ-spline potential can be done by formula

$$\frac{\langle f_{12} f_{13} f_{23} \rangle}{\langle f_{12} f_{13} \rangle} = -\frac{3B_3}{4B_2^2} \tag{3.23}$$

(Hoover 1991). Here B_2 is the second virial coefficient and $f_{ij} = \exp\left(-\beta U(r_{ij})\right) - 1$ is the Mayer *f*-function, *i* and *j* are the numbers of particles. The values in brackets can be obtained by hit and miss Monte Carlo method. There are 3 particles within a circle with radius R_{cut} with the centre on the particle 1, Fig. 3.15. In the Monte Carlo process, the 2nd and 3rd particle were given random position in a square centred on particle 1 with the side length $2R_{\text{cut}}$. If the positions get into the circle, f_{ij} are not equal to zero.

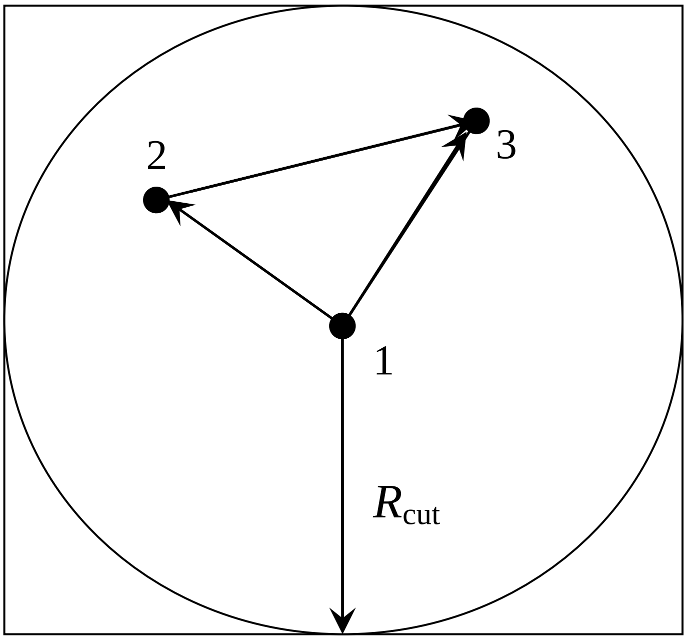

Figure 3.15. Calculation of the third virial coefficient by Monte Carlo method. Particle 1 is placed in the centre, the 2nd and 3rd particle are placed randomly in the circle.

The values in the numerator and denominator in the left hand side of Eq. (3.23) were summed over 10 000 000 steps and averaged. This number of steps was chosen empirically. The dependence of B_3 of two-dimensional LJ-spline fluid on the temperature is shown in Fig. 3.16. For 2*D* hard disk system, our program produces the 3rd virial coefficient 1.9299 for $T = 1.0$ after 100 millions MC steps. The exact value equals 1.9295 [Hoover 1991]. Same scheme can be adopted to compute B_4 but this requires several diagrams to be worked out.

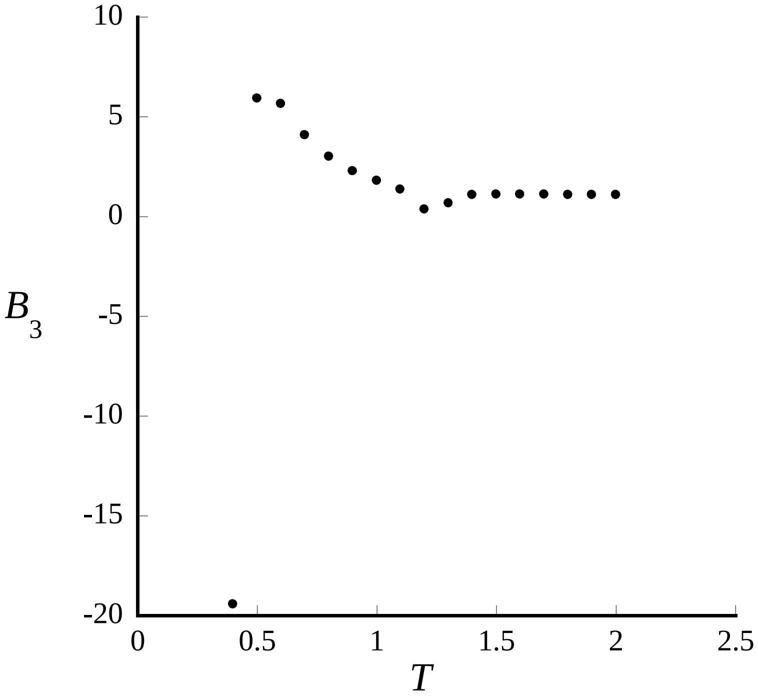

Figure 3.16. Dependence of the 3rd virial coeff. B_3 on the temperature for LJ-spline potential in two dimensions (10 millions MC steps).

3.5.3 Comparison of the virial equation of pressure with MC simulations

The equation of pressure with two virial coefficients is:

$$P = \rho kT(1 + B_2\rho + B_3\rho^2) \qquad (3.24)$$

It is necessary to compare the pressure of two-dimensional LJ-spline fluid obtained from Eq. (3.24) with that obtained from MD simulation to find the range of applicability of the virial coefficients. For $T = 1.2$, $B_2 = -0.056$ and $B_3 = 1.027$ (for 10 000 000 Monte Carlo steps), and the comparison is shown in Fig. 3.17:

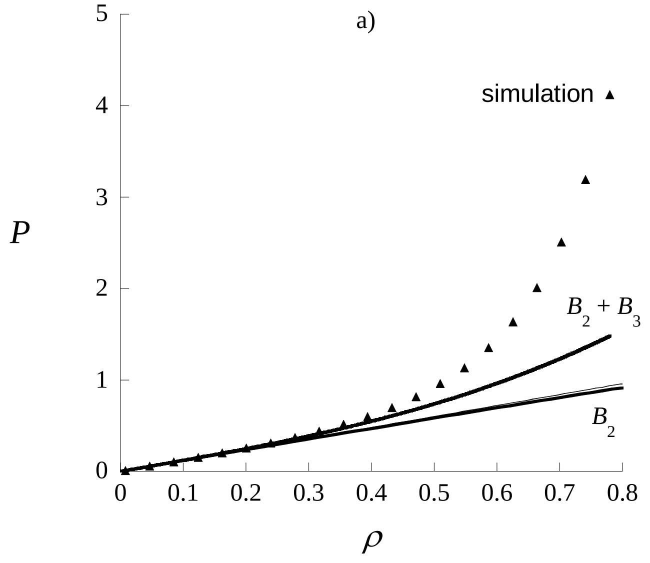

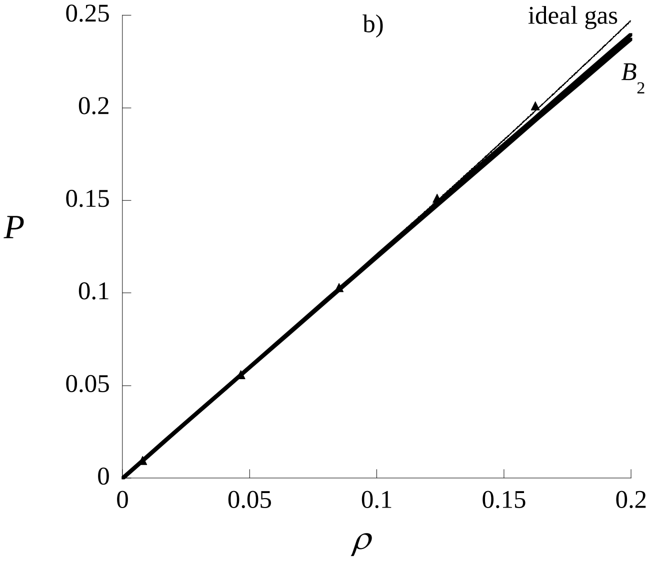

Figure 3.17a,b. Comparison of the pressure obtained by MD simulation of 2D LJ-spline fluid and by the virial equation (3.24) for $T = 1.2$. a) Symbols: simulated pressure, middle curve: Eq. (3.24); lower curve takes only B_2 into account; and the ideal gas line. b) A part of the upper plot increased.

One can see that there is a good agreement till $\rho \approx 0.3$. For $T = 0.7$, $B_2 = -1.8796$ and $B_3 = 4.095$, and the comparison is shown in Fig. 3.18. There is a good agreement till $\rho \approx 0.2 - 0.3$. For lower T, the agreement is poorer because the gas resembles less the ideal gas (the role of interatomic interactions is more important).

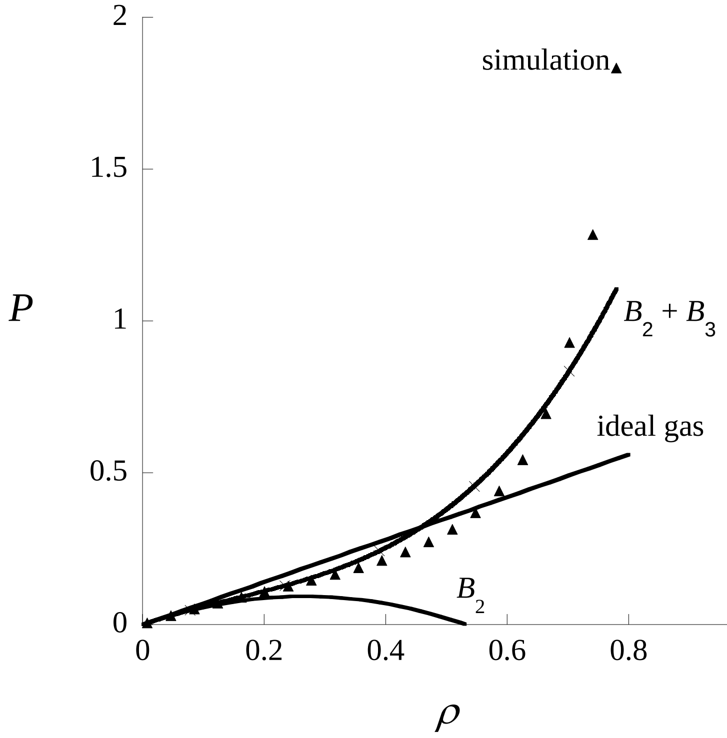

Figure 3.18. Comparison of the pressure obtained by MD simulation of two-dimensional LJ-spline fluid and by the virial equation (3.24) for $T = 0.7$. Symbols: simulated pressure; lower curve: taking B_2 into account; in the middle: ideal gas line; upper curve: Eq. (3.24).

3.6 Calculation of the Solid – Liquid Branch of the Phase Diagram. Practical Results

To calculate solid and liquid branches on a phase diagram it is necessary to solve numerically Eqs. (3.1). To evaluate the chemical potential (i. e., Gibbs energy per particle), one has to determine the Helmholtz free energy. For that purpose it is necessary to integrate Eq. (3.2) along reversible paths connecting reference states for which the free energy is known to the states of interest. For fluid the reference state is the ideal gas with $\rho = 0$ and the temperature of interest (here $T = 1$). The excess free energy of fluid (relative to the ideal gas) is calculated from Eq. (3.2) as

$$\frac{\beta A_{ex}(\rho)}{N} = \int_0^{\rho} \left[\frac{\beta P}{\rho'} - 1 \right] \frac{\mathrm{d}\rho'}{\rho'} \tag{3.25}$$

Supercritical isotherms $P(\rho)$ were obtained by us in MD simulations with periodic boundary conditions and Gaussian thermostat. The number of particles was 1024 and the number of steps was 2 − 10 millions. We use supercritical isotherms because there are no phase transitions along them. They were calculated for the temperature range 0.7 – 2.0 (the critical temperature is approximately 0.55), and for the density range 0.008 – 0.78 for liquids, and 0.8 – 1.1 for solids. The process of generating isotherms $P(V)$ was automated using a Perl script. An isotherm of the two-dimensional LJ fluid at $T = 0.7$ thus obtained is given in Figs. 3.19 and 3.20. It consists of liquid and solid branches. One can see the region of solid-liquid coexistence at $\rho \approx 0.81 – 0.85$.

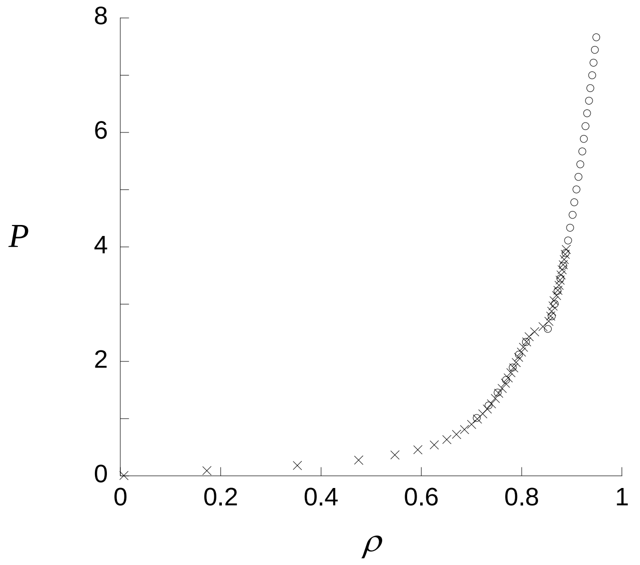

Figure 3.19. Pressure of two-dimensional LJ-spline substance versus its density at $T = 0.7$ obtained by MD simulations. Open circles: solid; crosses: fluid. Both curves overlap.

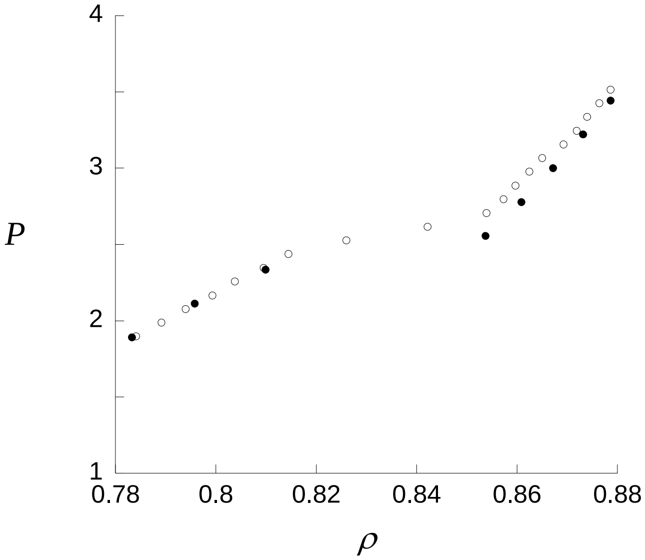

Figure 3.20. The melting region of Fig. 3.19 enlarged. Open symbols: liquid branch; filled symbols: solid branch.

Supercritical isotherms for fluid (until $\rho = 0.81$) can be fitted by a polynomial (Udink and Frenkel 1987):

$$P = \rho T(1 + B_2\rho + A_1\rho^2 + A_2\rho^3 + A_3\rho^4 + A_4\rho^5 + A_5\rho^6) \qquad (3.26)$$

Here B_2 is the 2nd virial coefficient calculated numerically by Eq. (3.23) and A_i are the fitting coefficients. The dependence of the pressure on the density for that fluid is given in Figure 3.21. The coefficients A_i are given in Table 3.3.

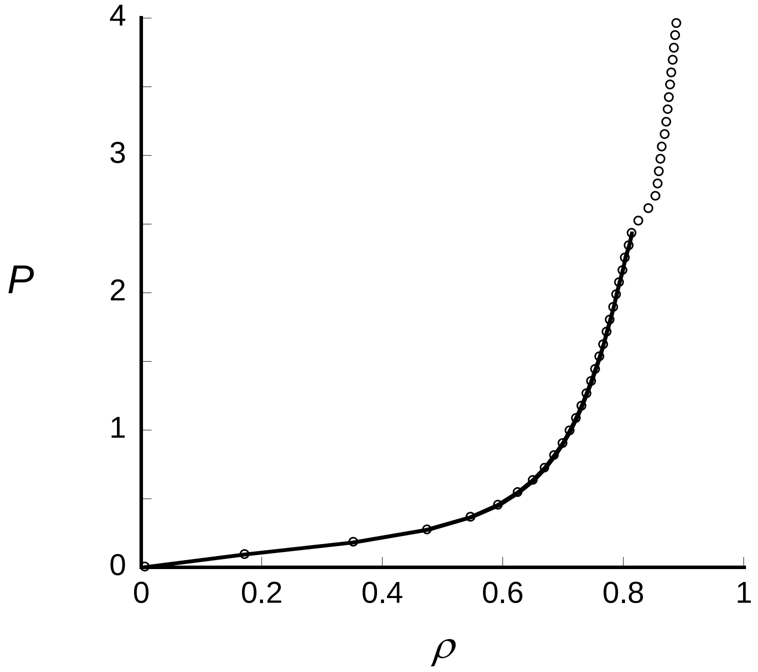

Figure 3.21. Dependence of the pressure of two-dimensional LJ-spline fluid on its density at T = 0.7; line: fit, Eq. (3.26); symbols: MD simulation, Fig. 3.19.

From Eqs. (3.25) and (3.26) we have:

$$A_{ex}(\rho) = T\left[B_2\rho + \sum_{i=1}^{5}\frac{A_i\rho^{i+1}}{i+1}\right] \tag{3.27}$$

For solid phase we choose the reference state T = 0.7 and ρ = 1. The density ρ = 1 lies outside the solid-liquid coexistence densities for all the temperatures so that the process is always reversible. The excess free energy of solid (relative to an Einstein crystal) for densities below unity can be obtained from Eq. (3.2):

$$\beta A(\rho) - \beta A(1) = \int_1^{\rho}\frac{\beta P}{\rho'^2}\mathrm{d}\rho' \tag{3.28}$$

Here the integration is performed from the solid reference state with the density 1.0. The supercritical pressure obtained in MD simulations was fitted by a 3-rd order polynomial (Udink and Frenkel 1987):

$$P = A_1\rho + A_2\rho^2 + A_3\rho^3 \qquad (3.29)$$

For $T = 0.7$, the coefficients A_i are given in Table 3.3. The dependence of pressure on density (from $\rho = 0.85$) for this temperature is given in Figure 3.22.

Table 3.3. Coefficients of Eqs. (3.26) and (3.29) for two-dimensional LJ-spline substance at *T* = 0.7

Phase	A_1	A_2	A_3	A_4	A_5
Liquid	−13.37(9.0)	122.17(60.5)	-307.35(150)	304.38(162)	-89.484(64.5)
Solid	141.34(1.6)	−354.78(3.5)	225.76(1.9)	–	–

Error is given in the brackets.

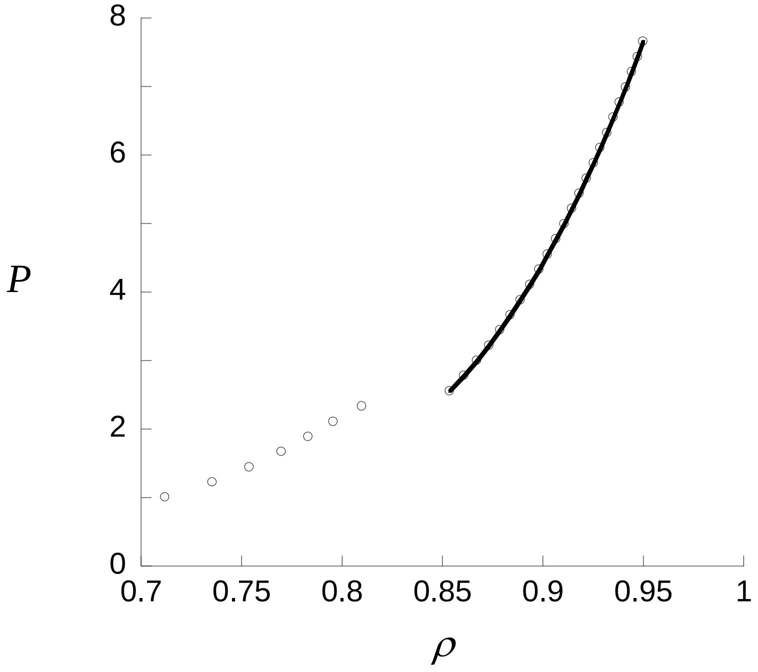

Figure 3.22. Dependence of the pressure of two-dimensional LJ-spline solid on its density at $T = 0.7$. Line: fit, Eq. (3.29); symbols: MD simulation.

The corresponding data and plots for T = 1.0 are presented in Table 3.4 and Figs. 3.23 – 3.26. The region of solid-liquid coexistence in this case is at $\rho \approx 0.85 - 0.89$. According to the ideas of Udink and Frenkel (1987) the solid – liquid region for LJ-spline fluid is narrow because of short range potential.

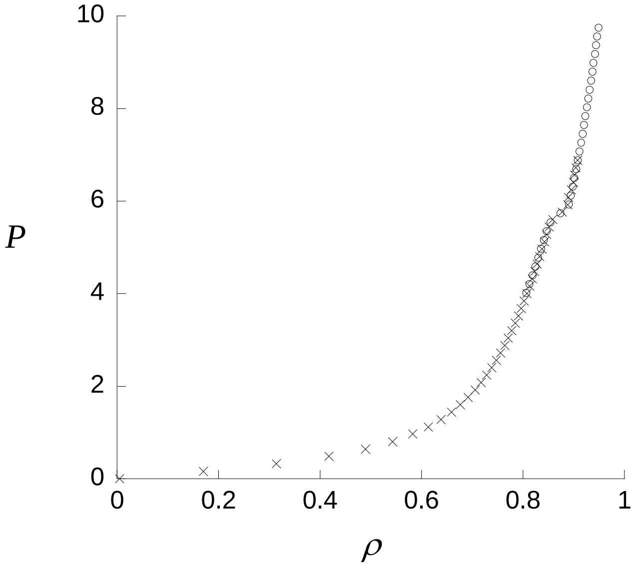

Figure 3.23. Pressure of two-dimensional LJ-spline substance versus its density at T = 1.0 obtained by MD simulation. Crosses: liquid; circles: solid.

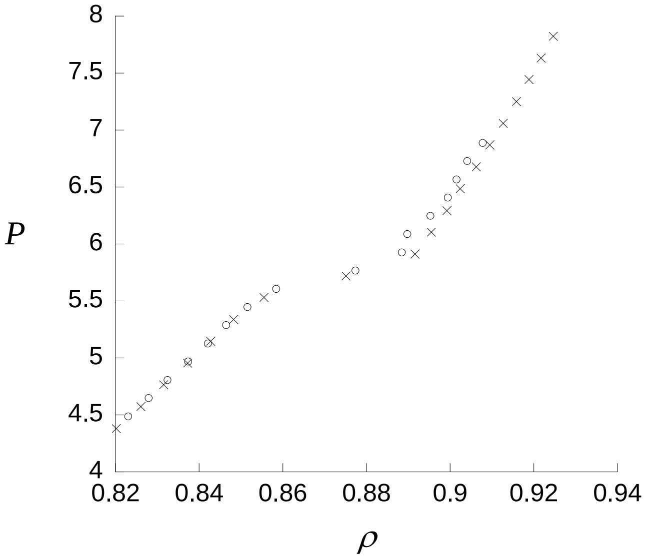

Figure 3.24. The melting region of Fig. 3.23 enlarged. Crosses: liquid; circles: solid.

Table 3.4. Coefficients of Eq. 3.26 and (3.29) for two-dimensional LJ-spline substance at *T* = 1.0.

Phase	***A*₁**	***A*₂**	***A*₃**	***A*₄**	***A*₅**
Liquid	−29.735(10.6)	225.27(68.4)	−570.53(162)	607.95(167)	−220.22(63.5)
Solid	171.57(3.4)	−416.66(7.4)	259.84(4.0)	–	–

Error is given in the brackets.

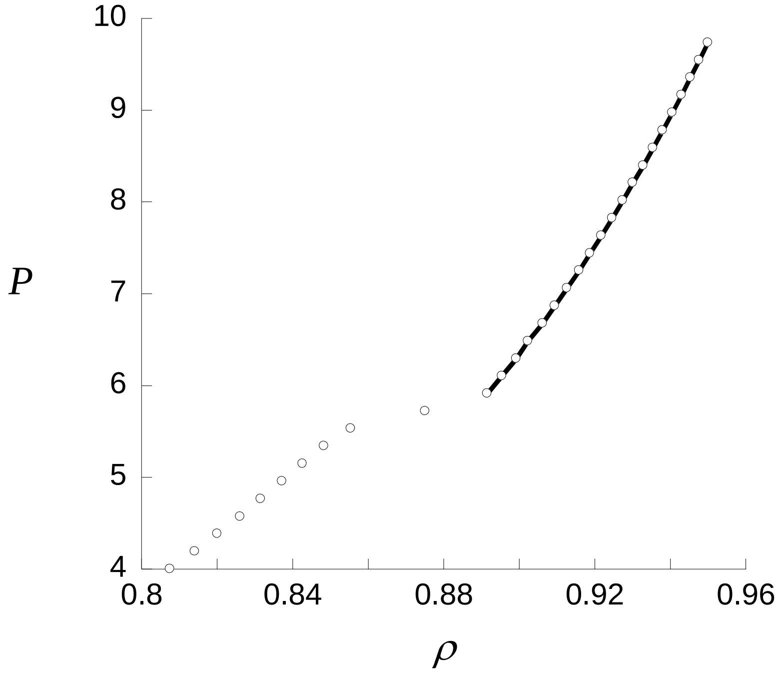

Figure 3.25. Dependence of the pressure of two-dimensional LJ-spline solid on its density at T = 1.0. Line: fit, Eq. (3.29); symbols: MD simulation.

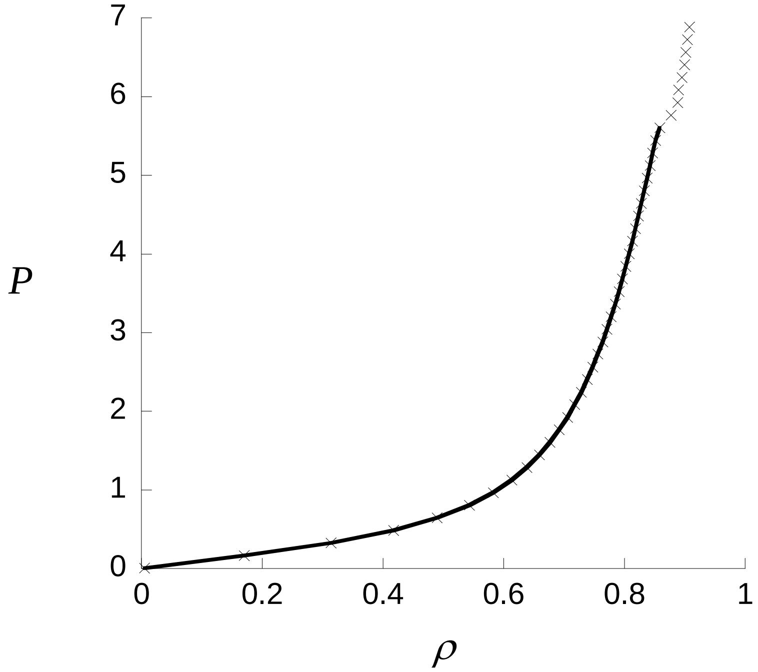

Figure 3.26. Dependence of the pressure of two-dimensional LJ-spline fluid on its density at *T* = 1.0. Line: fit, Eq. (3.26); crosses: MD simulation.

With Eq. (3.29), Eq. (3.28) turns to

$$A_{ex}(\rho) = A(1) + A_1 \ln \rho + A_2(\rho - 1) + \frac{A_3}{2}(\rho^2 - 1) \qquad (3.30)$$

From Eqs. (3.4), (3.27) and (3.30) one can obtain the Gibbs energy per particle for both phases.

We made an attempt to solve Eqs. (3.1), (3.4), (3.27), (3.29) and (3.30) by a Matlab program but convergence was not achieved and wrong results were obtained because of a high instability of the problem. Our Matlab program is given in Appendix 1. Using metrics minimisation, the points on the solid – liquid phase diagram were obtained numerically for *T* = 0.7 and 1.0. They are given in Table 3.5. The liquid − solid curves are extrapolated along them, Fig. 4.25. This is also a new interesting result.

Table 3.5. Liquid-solid interface for LJ-spline potential obtained by Maxwell equal area construction.

T	ρ_{liquid}	ρ_{solid}
0.7	0.840	0.869
1.0	0.860	0.886

In Fig. 3.27 the Helmholtz energy for LJ-spline liquid and solid for T = 0.7 is given. One can see that it is extremely complicated to determine the coexisting densities by the common tangent construction. If this plot had two distinct minima, we could apply this common tangent method.

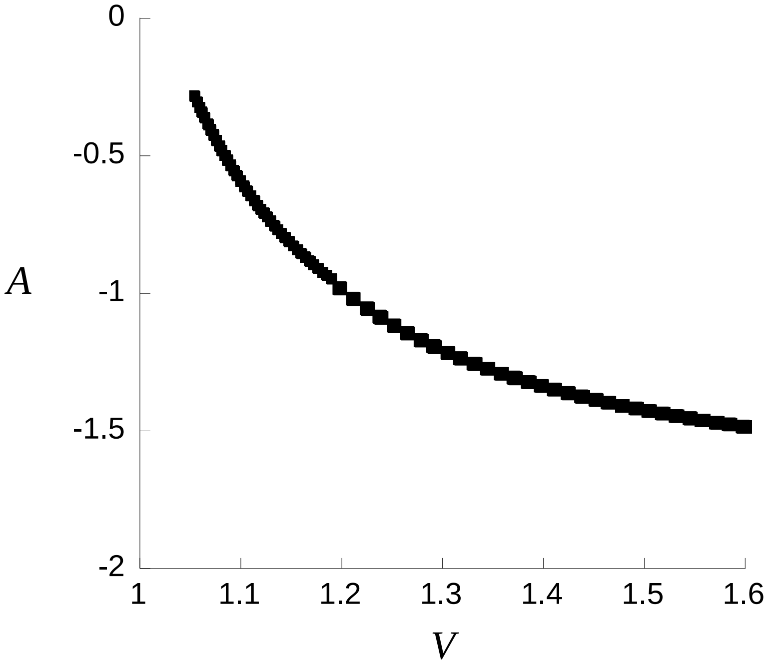

Figure 3.27. Helmholtz energy for LJ-spline liquid and solid for T = 0.7. Left curve, solid, right curve, liquid.

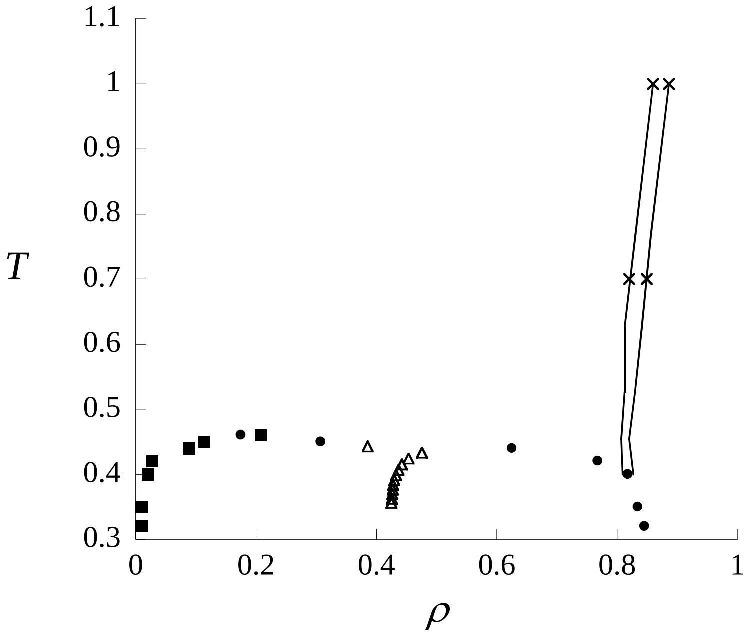

Figure 3.28. Phase diagram of the LJ-spline fluid. On the right hand side, the liquid – solid curves. Triple line is about *T* = 0.4. In the middle, triangles, the law of rectilinear diameters.

3.7 Conclusions

In this Chapter, the upper part of the binodal for the two-dimensional LJ-spline fluid is obtained by Gibbs ensemble Monte Carlo simulation. Nobody obtained it earlier. It has been found that the triple point is about *T* = 0.4. This phase diagram resembles those of similar LJ potentials what should be expected. Two points on the liquid - solid branch of the phase diagram were obtained using metrics minimisation and this is also a new and good result. However, we did not succeed to produce these points with our Mathlab program. A possible reason could be an error in algebra and this requires further investigation. These two points are at *T* = 0.7 and 1.0, and the curves are extrapolated along them. This is also a new interesting result. An attempt to obtain the same diagram by the Gibbs − Duhem simulation failed and this requires further investigation. We have shown that it is very complicated to determine the coexisting liquid and solid densities by the common tangent construction.

We have also produced the 2nd and 3rd virial coefficient for the two-dimensional LJ-spline fluid. It was not done earlier. It is important to compare the pressure of the two-dimensional LJ-spline fluid obtained with these coefficients with that obtained from MD simulation to find the range of applicability of the virial coefficients. The pressure of the two-dimensional LJ-spline fluid obtained with the virial coefficients is compared with that obtained from MD simulation for $T = 0.7$ and 1.2. There is a good agreement till $\rho \approx 0.2 - 0.3$.

Chapter 4

Expansion via the Holian-Grady Method

4.1 Introduction

Studies of fluid fragmentation are now of importance because of many applications. One can mention hot nuclear matter which exhibits fragmentation and a transition from a liquid-like phase to a gas-like one during bombardment by heavy ions (Schulz *et al*. 1984). One can name other examples: combustion in motors and in other processes of combustion (Sotolongo-Costa 1996), for example, droplet fragmentation in a diesel fuel jet (Ahurst and Holian 1999) and fragmentation and atomization of liquids in liquid jets at the nozzle exit (Reitz and Bracco 1982). To describe the phenomenon of fragmentation quantitatively it is useful to achieve the ability to simulate the fragmentation of a fluid under homogeneous adiabatic expansion.

The aim of our work described in this Thesis is to carry out molecular dynamics simulations of fragmentation of expanding two-dimensional fluids. The molecular dynamics (MD) method has a very big predictive capability. Molecular dynamics is exact for a given force law. It complements Monte Carlo well. We use simple force laws to study microscopic fragmentation. In fragmentation science it is necessary to find the correct statistical theory among the many existing. It is very difficult to do from the experiments due to their complexity. MD is a very useful tool for this purpose.

There are two published methods of simulation of a homogeneous expansion of fluids by molecular dynamics: the methods of Blink and Hoover (Blink and Hoover 1985), and Holian and Grady (Holian and Grady 1988). The former one is more complicated and will be considered in detail in the next Chapter. In our work we have compared the numerous results produced by both methods for different systems under a large variety of conditions. To the best of our knowledge, nobody has done such an extensive comparison before. We compare our simulations with energy based theoretical models of fragmentation.

In this Chapter, we consider the method of Holian and Grady for the simulation of fragmentation of condensed matter undergoing adiabatic expansion. It uses non-equilibrium molecular dynamics and the periodic boundary conditions. It was used also by Toxvaerd (1998). We describe the algorithm and verify it against the existing literature data, and then we report simulations of much larger systems (up to N = 541 696) than our predecessors.

4.2 Holian-Grady Algorithm

In this molecular dynamics based method the two-dimensional system is modelled as an expanding grid of periodically repeated squares (it means, the periodic boundary conditions are imposed). At time zero the fluid is in an equilibrium state. The particles possess initial coordinates and momenta. At time t = 0+, the side lengths of the rectangle expand at a constant rate, $\dot{\eta}$, in both the x and y directions:

$$L_x(t) = L_x(0)(1+\dot{\eta}t)\,;\ L_y(t) = L_y(0)(1+\dot{\eta}t) \qquad (4.1)$$

Consequently, the velocities of particles increase linearly with the rate $\dot{\eta}$. For example, the x component of the velocity of particle i becomes

$$v_{ix}(0+) = v_{ix}(0) + \dot{\eta}x_i(0) \qquad (4.2)$$

where $x_i(0)$ and $v_i(0)$ are its initial coordinate and thermal velocity. For the times greater than t = 0+, the expansion is adiabatic because no more energy is added to the system, and the particles obey Newton’s equations of motion, with expanding periodic boundary conditions.

If particle i leaves the simulation box at the left side in the x direction with a velocity v_{ix}, it enters at the right side of the box with the coordinate $x_i(t+) = x_i(t) + L_x(t)$ and a velocity equal to

$$v_{ix}(t+) = v_{ix}(t) + \dot{L}_x(t) = L_x(0)\dot{\eta} \qquad (4.3)$$

The opposite occurs if the particle leaves the box at the right hand side: $x_i(t+) = x_i(t) - L_x(t)$ and $v_{ix}(t+) = v_{ix}(t) - \dot{L}_x(t)$.

In order to determine thermal properties of the system during the expansion one needs to obtain the particuliar velocities of the particles $\mathbf{v}_i'(t)$ (in expanding frame). It is done by the following formula (Toxvaerd 1998):

$$\boldsymbol{v}_i'(t) = \boldsymbol{v}_i(t) - \dot{\eta}\boldsymbol{r}_i(t)\frac{L_x(0)}{L_x(t)} \tag{4.4}$$

It is possible to improve upon Holian and Grady's algorithm by making use of the Dolls tensor Hamiltonian (not explored here).

4.3 Equilibration: Validation

To validate our two-dimensional MD code we compared our results of a simulation of the two-dimensional Lennard-Jones fluid with those in Barker et al (1981) obtained by MC for *N* = 256, Table 4.1, and got excellent agreement. Our system size *N* was 1600 particles, run length was 100 000 steps and the cut off radius was 5.0 (so not LJ spline). Holian and Grady do not give any numbers to compare for their equilibrium case.

Table 4.1. Pressure, *P*, and the potential energy, *U* obtained with our MD code and obtained by MC by Barker et al (1981).

	This work		**(Barker et al 1981)**	
	<*P*>	**–<*U*>**	**<*P*>**	**–<*U*>**
***T*=0.7, ρ = 0.803**	2.07(9)	2.363(59)	2.01	2.367
***T*=1.0, ρ = 0.80**	3.57(6)	2.177(69)	3.51	2.178

Holian and Grady used the Lennard-Jones potential truncated at $R_{\mathrm{cut}} \approx 1.74\sigma$ and smoothly extrapolated to zero by a cubic spline from the point of inflection $R_{\mathrm{cut2}} \approx 1.24\sigma$, Fig. 2.2. In (Toxvaerd 1998) Lennard-Jones potential truncated at 2.5σ and shifted was used. Blink and Hoover (1985) use the LJ potential truncated at 2.5.

To verify our own two-dimensional MD code for the Holian-Grady expansion method, we performed a number of simulations at the same conditions as in (Holian and Grady 1988). We consider a two-dimensional fluid with a LJ potential truncated and smoothly extrapolated by a cubic spline with the same R_{cut} and R_{cut2}, Eq. (2.18). The initial state is a fluid at a density approximately that of the triple point ($\rho = 0.75$), and a temperature a little higher than that of the critical point of LJ fluid with full-range potential ($T = 0.6$).

The pressure in this method was calculated by the virial

$$PV = \sum_i m\mathbf{v}_i^2 + \frac{1}{2}\sum_i \sum_j \mathbf{r}_{ij} \cdot \mathbf{F}_{ij} \qquad (4.5)$$

where $\mathbf{v}_i$ are the velocities of atoms, $\mathbf{r}_{ij}$ and $\mathbf{F}_{ij}$ are the distances and the forces between the atoms and V is the system volume (Allen and Tildesley 1987).

A set of 4225 particles, as in (Holian and Grady 1988) was initially set up on a regular square lattice. Their initial velocities are sampled from a Maxwell-Boltzmann distribution with zero mean and variance proportional to the required temperature (§2.1.1). At the beginning, an equilibrium state was prepared for a constant volume with 100 000 steps. This number was chosen by trial and error method: we plotted physical values versus time. A plateau in this dependence indicated equilibrium was achieved.

During the equilibration, a Gaussian thermostat was used to control temperature (§2.1.7). To integrate the equations of motion a Runge-Kutta 4th order scheme was used with $\Delta t = 0.001$. In Fig. 4.1 the positions of the particles are shown after the equilibration.

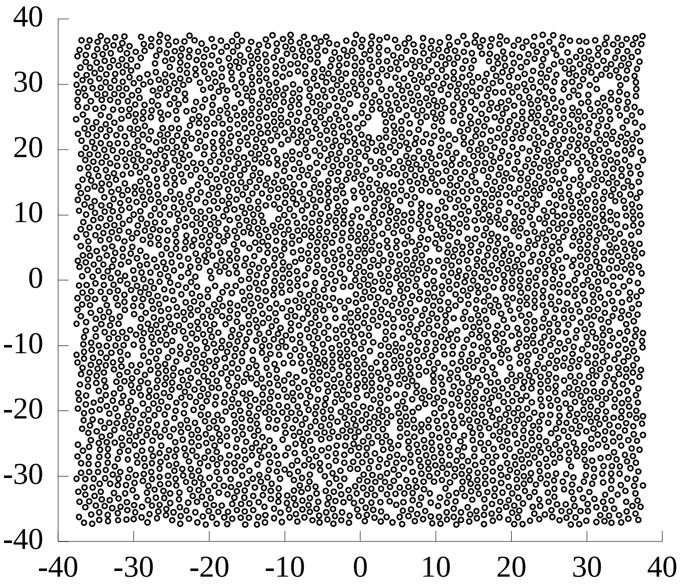

Figure 4.1. Snapshot of particle positions after the equilibration of two-dimensional MD system before expansion by Holian and Grady method (this work). $N = 4225$, $\rho = 0.75$, $T = 0.6$. Number of steps = 100000, Time step = 0.001.

Our snapshots of the two-dimensional liquid reveal the presence of large vacancies within the fluid which agrees with the data of other researchers and with the experiment (Fehder 1969), (Singh et al 1990). As pointed out by them, the presence of these vacancies indicates an important effect of the attractive forces in the two-dimensional LJ fluid. These authors used in their analysis also the radial distribution functions $g(r)$, they compared them at several densities. Another method of quantitative analysis would be to employ the structure factor $S(q)$. This is an aim of the future work.

4.4 Expansion: Validation

We carried out a few expansion runs after the equilibration, with the same conditions as in (Holian and Grady 1988): initial density $\rho_0 = 0.75$, initial temperature $T_0 = 0.6$. Two expansion rates, $\dot{\eta}$, were used: 0.107 and 0.21. The square simulation box is expanded until its side lengths have increased by a factor of approximately 2. That is, the final density is 0.175 for all expansion rates.

It is interesting to compare these rates with typical experimental values. The values of σ, ε and atom mass for argon are $3.4\cdot10^{-10}$ m, $1.65\cdot10^{-21}$ J and $39.9/6.02\cdot10^{-26}$ kg, respectively. For $\dot{\eta}$ = 0.107, the dimensionless time needed to double the box length is $1/\dot{\eta}$ = 10. This time is $2.15\cdot10^{-11}$ seconds, and $\dot{\eta}$ approximately equals $5\cdot10^{10}$ s^{-1}. The strain rate of a piston in a car engine is maximum 10^7 s^{-1}. So, the strain rates used in atomic simulations are many orders of magnitude greater than anything achievable in engineering situations.

The expanding fluid follows an isentrope on the phase diagram of the two-dimensional Lennard-Jones system in Fig. 4.2.

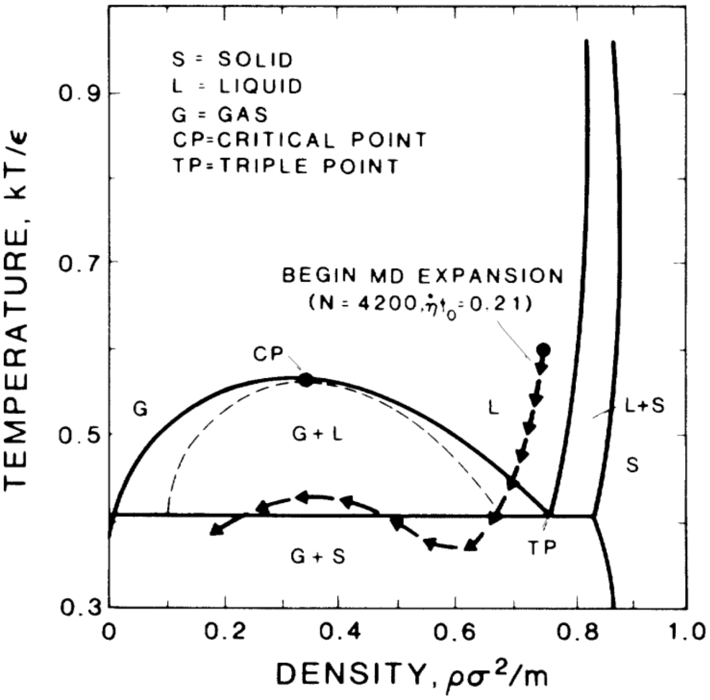

Figure 4.2. Phase diagram for two-dimensional Lennard-Jones system. Reproduced from (Holian and Grady 1988). Arrows show molecular dynamics expansion path. Dashed curve is spinodal line. (There is a misprint in the legend of that Figure. The expansion path is for $\dot{\eta}$ = 0.107 but not for 0.214 – private communication by B. Holian to K. Travis.)

The simulations used a 4th order Runge-Kutta integrator with Δt = 0.002 for $\dot{\eta}$ = 0.0535, Δt = 0.001 for $\dot{\eta}$ = 0.107, etc. Time step decreases with the expansion rate. We obtained a similar picture and final temperature to Holian and Grady at the beginning of the expansion, Fig. 4.3a. Their plot is given on Fig. 4.3b. Holian and Grady found that fragmentation began about the time $t = 1$, the density $\rho \approx 0.612$ and temperature $T \approx 0.37$, when incipient voids (microcracks) form due to thermal fluctuations. Our result supports this view. At the time 0 of the expansion, our system contained 4210 particles in 6 clusters and 15 monomers. At the time $t = 1$ and rate 0.107, there were 4089 particles in 86 clusters (in average, 48 particles per cluster). At the expansion rate 0.214 and at $t = 0.5$, we had 4021 particles in 189 clusters (in average, 21 particles per cluster). The average cluster size decreases with increasing rate, as expected. The dependence of cluster size on the expansion rate is considered in detail in §4.10. The comparison of that size for a given density and temperature is given in §4.9.

A snapshot of the particle positions at the end of the expansion at the rate 0.107 (at $t = 10$) is given in Fig. 4.3c. This is a picture of a non-equilibrium state, since many of the fragments are far from spherical. It resembles very well the corresponding Figure from (Holian and Grady 1988), Fig. 4.3d in this report. (In (Holian and Grady 1988) it is written that this is a snapshot for the expansion at the rate $\dot{\eta} = 0.21$ but this is a misprint – private communication by B. Holian to K. Travis.) At $t = 10$ (Figs. 4.3c and d), one can see that the system consists of many elongated fragments with similar sizes. The number of monomers is small in both cases. In our case, it is about 279(20), standard error is given in the brackets, i.e. 6.6%. It was about 140 at $t = 1$. Holian and Grady point out that if the system was at equilibrium then 80% of the mass would be in the vapour phase. Unfortunately, these authors do not provide a proof of their statement. Our simulation of the equilibrium case at the same state point as in Fig. 4.3c: $\rho = 0.175$, $T \approx 0.38$, gave the number of monomers 558(20), namely 13% (see §4.11, Fig. 4.26).

a) t = 1; ρ = 0.612, $T \approx$ 0.37. This work

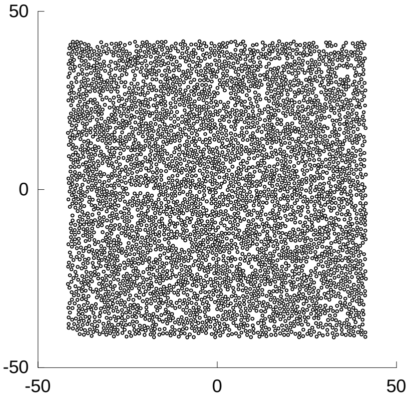

b) t = 1; ρ = 0.612; $T \approx$ 0.37 (Holian and Grady 1988)

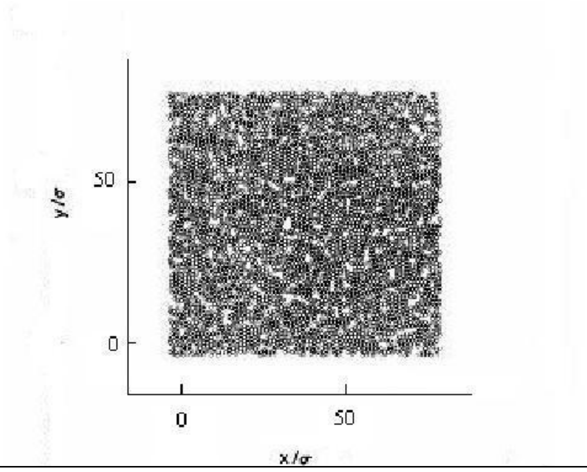

c) t = 10; ρ = 0.175, $T \approx$ 0.38. This work

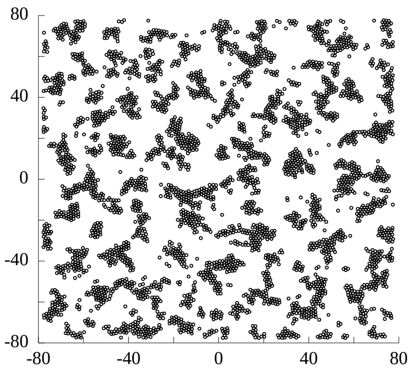

d) t = 10; ρ = 0.175, $T \approx$ 0.39 (Holian and Grady 1988)

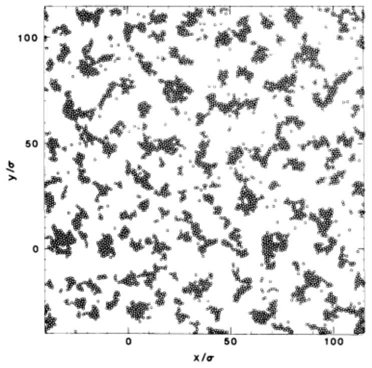

Figure 4.3a - d. a) Snapshot of particle positions shortly after start of two-dimensional MD expansion with Holian − Grady method. N = 4225, ρ_0 = 0.75, T_0 = 0.6 and $\dot{\eta} = 0.107$. Expansion time t = 1, ρ = 0.612, $T \approx$ 0.37. b) Same but obtained by Holian and Grady (reproduced from (Holian and Grady 1988)), ρ = 0.612, $T \approx$ 0.37. c) Snapshot of final particle positions, ρ = 0.175, t = 10, $T \approx$ 0.38. d) Same but obtained by Holian and Grady (reproduced from (Holian and Grady 1988)), ρ = 0.175, $T \approx$ 0.39.

Ideally, we would show that ours and Holian-Grady's results are equivalent by comparing radial distribution functions but Holian and Grady did not include such information in their papers and, therefore, we have to rely on pictures, cumulative fragment distributions and final temperatures.

4.4.1 Analysis of fragment distribution

The fragment size distribution can be characterised by the cumulative number of clusters. The cumulative number of clusters is the number of clusters of mass *M* or greater (it is more convenient to use the cumulative number because it is much less noisy than the actual number). The cumulative distribution is represented by a bimodal distribution:

$$C(M) = \int_M^{\infty} S(M')\,dM' = N_m \exp\left(-\frac{M}{\mu_1}\right) + \frac{N - N_m}{\mu_2} \exp\left(-\frac{M}{\mu_2}\right) \qquad (4.6)$$

where $S(M)$ is density of probability of clusters of size M, N is the number of particles in the system, N_m is the number of monomers, and μ_1 and μ_2 are the two population means. The first mode μ_1 is equal to 1 and the second one μ_2 is equal to the average fragment mass. Such a distribution obtained by Holian and Grady at $\dot{\eta}$ = 0.107 is presented at the Fig. 4.4.

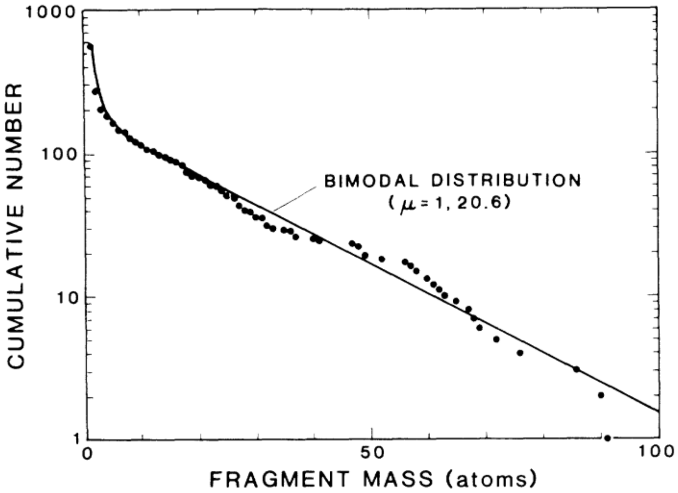

Figure 4.4. Cluster statistics for the final state of two-dimensional MD expansion (N = 4225) at initial rate $\dot{\eta} = 1.07$. Reproduced from (Holian and Grady 1988). Cumulative number of fragments of mass *M* or greater (dots) vs *M*, along with fitted bimodal distribution (solid curve). The initial density and temperature were ρ_0 = 0.75 and T_0 = 0.6, and the final density and temperature were ρ =

0.175 and T ≈ 0.39 (There is a misprint in (Holian and Grady 1988). They performed the simulation at $\dot{\eta}$ = 0.107, not at 0.214.)

One can determine the average cluster size $<\mu_2>$ (we denote it $<\mu>$ from now on) from the slope of the shoulder on the plot of cumulative number versus fragment mass, ln$C(n)$ vs n. Holian and Grady determined that the average cluster size $<\mu>$ on Fig. 4.4 equals 20.6. Our simulation at $\dot{\eta}$ = 0.107 is given in Fig. 4.5. It was obtained with 10 realisations (it means, with 10 different initial configurations, this will be considered later). It resembles Fig. 4.4 rather well. We obtained $<\mu>$ = 20.2. We also present the plot of the cumulative number of fragments for the expansion rate 0.214 in Fig. 4.6 obtained with 10 realisations. Our simulation produced $<\mu>$ = 8.0(3).

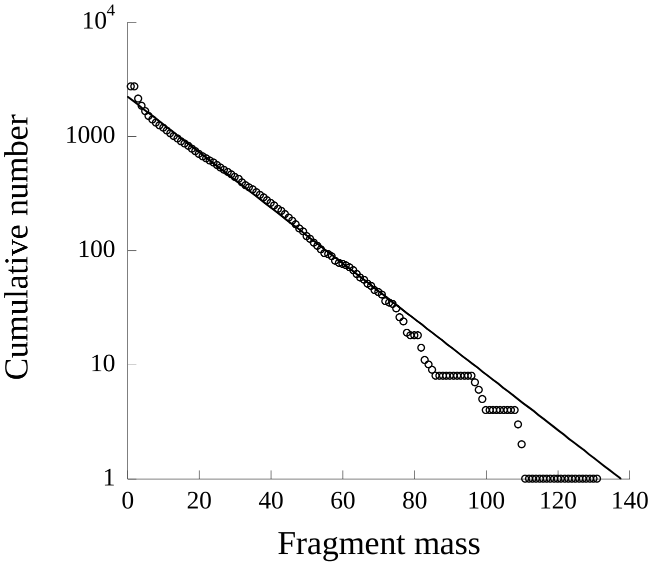

Figure 4.5. Cumulative number of clusters of mass M or greater vs M at the end of two-dimensional MD expansion by the Holian-Grady method. N = 4225, ρ_0 = 0.75, T_0 = 0.6 and expansion rate $\dot{\eta} = 0.107$. Straight line is linear fit.

We found that plots in Figs. 4.5 and 4.6 also obey the bimodal distribution, however, they disobey it at far right end, for large fragments. The role of the first mode is negligible. The experimental distribution for explosive fragmentation of a steel cylinder obeys a bimodal distribution beautifully in the whole range of fragment sizes (Mock and Holt 1983). At $\dot{\eta} = 0.107$ there are a few clusters which are much larger than the others. At the rate $\dot{\eta} = 0.214$, the dependence of the number of clusters on their size is much smoother.

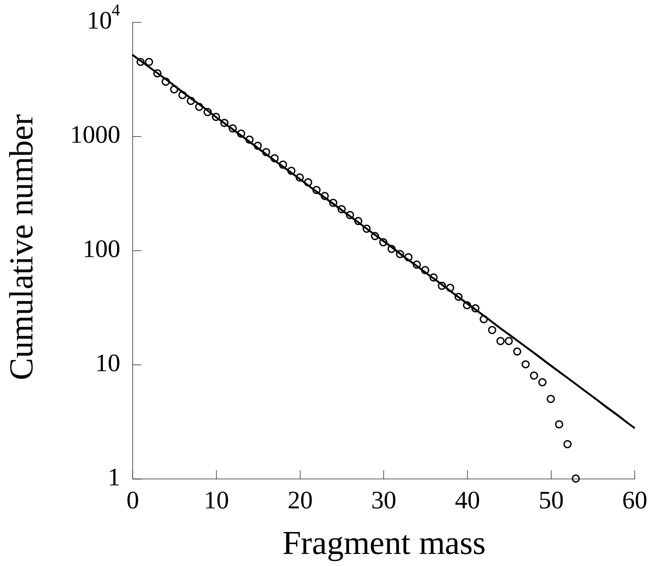

Figure 4.6. Cumulative number of clusters of mass *M* or greater vs *M* at the end of two-dimensional MD expansion by the Holian-Grady method. $N = 4225$, $\rho_0 = 0.75$, $T_0 = 0.6$ and expansion rate $\dot{\eta} = 0.214$. Straight line is linear fit.

4.5 Cluster Statistics

In (Blink and Hoover 1985) the fragment translational, rotational, thermal and monomer temperatures were defined. The translational temperature is the fragment's centre-of-mass kinetic energy divided by Boltzmann's constant *k*, and the fragment size in atoms. The rotational temperature is $\frac{L^2}{kN_c I}$ where *I* is the moment of inertia of the fragment, *L* is the angular momentum around its centre, and N_c is the number of particles in the fragment. The fragment thermal temperature is defined as the remaining kinetic energy (once translational and rotational contributions have been removed) divided by *k* and the fragment size. The monomer temperature is the temperature of the monomers (vapour, fragments containing exactly one atom). We have written programs which extract these temperatures from our simulations results. These programs calculate also the relative shape anisotropy (it will be defined further) and the root mean square radius of gyration. The radius of gyration can be defined through the gyration tensor:

$$S_{ab} = \frac{1}{n}\sum_{i=1}^{n} r_a^i r_b^i \tag{4.7}$$

Here *n* is the total number of the particles in the cluster, r_a^i and r_b^i are Cartesian coordinates of the *i*-th particle in the centre of mass frame. The gyration tensor is symmetric and can be reduced to the diagonal form:

$$\mathrm{S} = \begin{bmatrix} \lambda_x^2 & 0 \\ 0 & \lambda_y^2 \end{bmatrix} \tag{4.8}$$

where $\lambda_x^2 \le \lambda_y^2$ (these diagonal values are called the principal moments of the tensor). Then the squared radius of gyration is defined as the sum of its diagonal elements:

$$R_{\mathrm{g}}^2 = \lambda_x^2 + \lambda_y^2 \tag{4.9}$$

The relative shape anisotropy is defined

$$\kappa^2 = \frac{\left(\lambda_x^2 - \lambda_y^2\right)^2}{R_{\mathrm{g}}^4} \tag{4.10}$$

It takes the values between zero and one. Zero means perfect circle and one means line.

4.5.1 Relative shape anisotropy

In Fig. 4.7 the dependence of the shape factor of the fragments on the relative expansion time for the system with *N* = 4225 is given for various expansion rates. They show that for all rates except 0.856, the relative shape anisotropy has a weak dependence on $\dot{\eta}$, and *t*. At the rate 0.856 the dependence exhibits a peak. At the highest rate the fragments are mostly elongated, which should be expected.

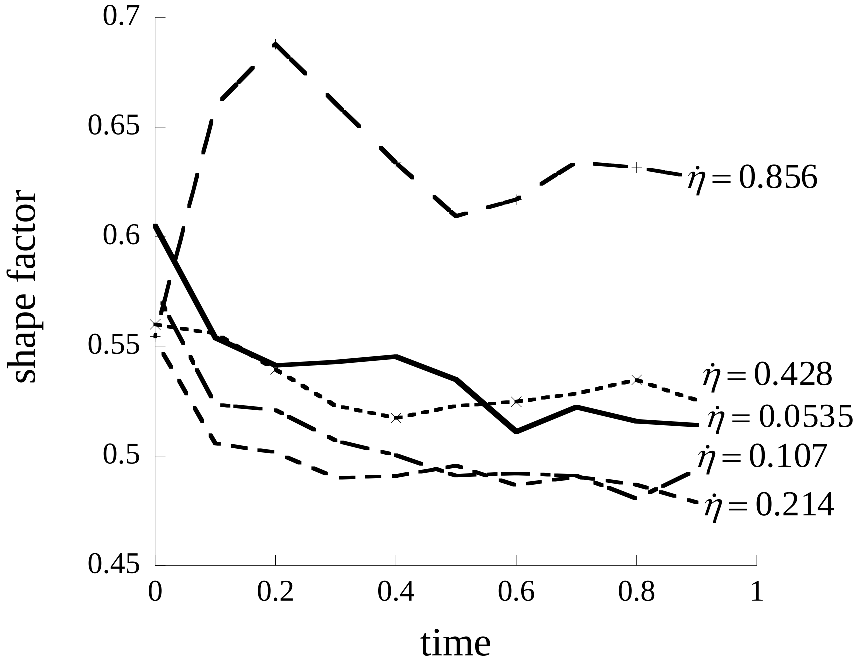

Figure 4.7. Shape factor of fragments versus reduced expansion time for various expansion rates. $N = 4225$, $\rho_0 = 0.75$ and $T = 0.6$. The time is divided by the total expansion time.

In Fig. 4.8 the same dependence is given for the system with $N = 541\ 696$. It resembles very much the plot for $N = 4225$, Fig. 4.7. We know already that the fragment size decreases with increasing expansion rate but their shape is approximately the same for all rates but 0.856. For all rates but 0.856 the relative shape anisotropy depends weakly on the expansion rate and time. At the rate 0.856, the dependence exhibits the same striking peak as for $N = 4225$. One can make a conclusion that in general, the shape factor increases with the expansion rate.

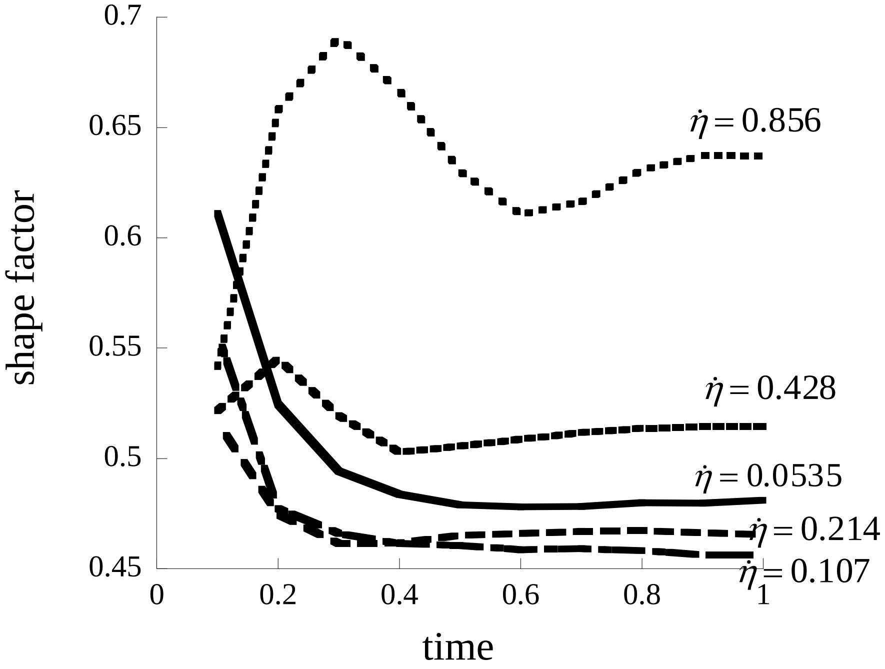

Figure 4.8. Shape factor of fragments versus reduced expansion time for various expansion rates. N = 541 696, ρ_0 = 0.75 and T = 0.6. The time is divided by the total expansion time.

On Figs. 4.9 and 4.10, the dependence of the probability distributions of the relative shape anisotropy on the fragmentation time are given for N = 33 856 and expansion rates 0.0535 and 0.856. This dependence for other system sizes is similar. The latest one is approximately the mirror image of the former one; and for the rate 0.428 we found that the probability distribution practically does not depend on the fragmentation time. However, it is possible that these differences between the mirror images are not statistically significant. One can see that in the system about 15% of clusters are almost symmetric.

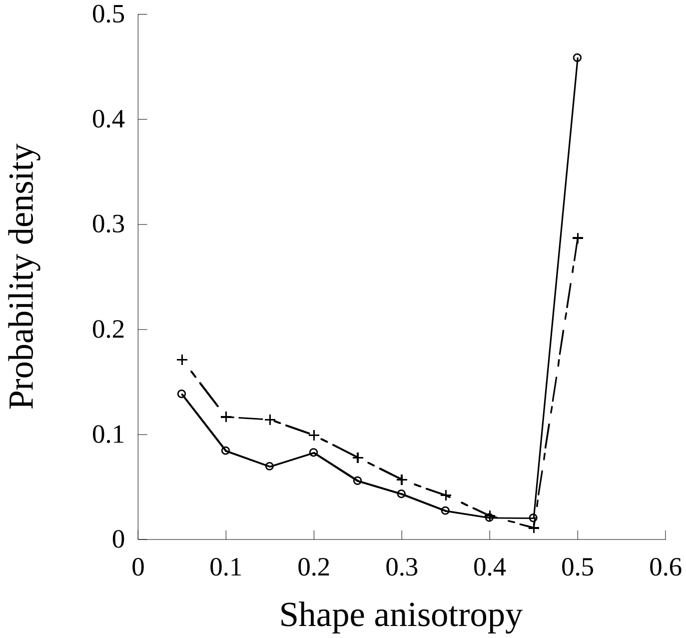

Figure 4.9. Histogram of the relative shape anisotropy on the relative fragmentation time in the Holian-Grady method. *N* = 33 856, $\dot{\eta} = 0.0535$, circles, *t* = 0.1, plusses, *t* = 1.

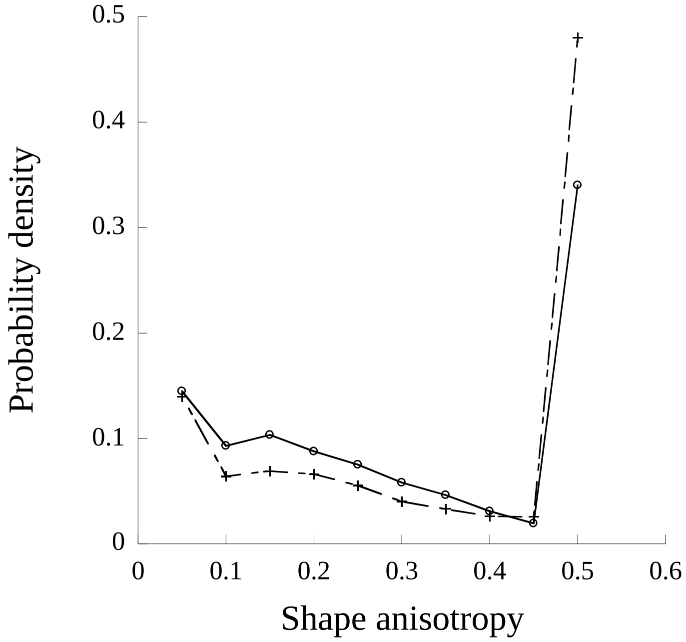

Figure 4.10. Histogram of the relative shape anisotropy on the relative fragmentation time in the Holian-Grady method. *N* = 33856, $\dot{\eta} = 0.856$, circles, *t* = 0.1, plusses, *t* = 1.

4.5.2 Thermal temperature of fragments

In Fig. 4.11 the dependence of the thermal temperature of fragments in the laboratory frame on the expansion time for various expansion rates is given. One can see that at the initial stage the temperature increases sharply due to external expansion, then it decreases. The reason of that is simple. We expand the box, the inter-particle bonds fail due to fluctuations, and the energy of expansion turns to kinetic and thermal energy of fragments. After some time, the system consists of many fragments which are not chained to each other, and subsequent pulling does not increase the energy of fragments. The thermal energy of fragments slowly decreases because it increases the monomer temperature which is lower. Our program measures the configuration temperature in the expanding system frame. It practically does not depend on the expansion rate and time and is equal with a high accuracy to 0.30(1). For the rate $\dot{\eta} = 0.856$ it is slightly higher: 0.33(5). Therefore, the thermal temperature also practically does not depend on the expansion rate and time.

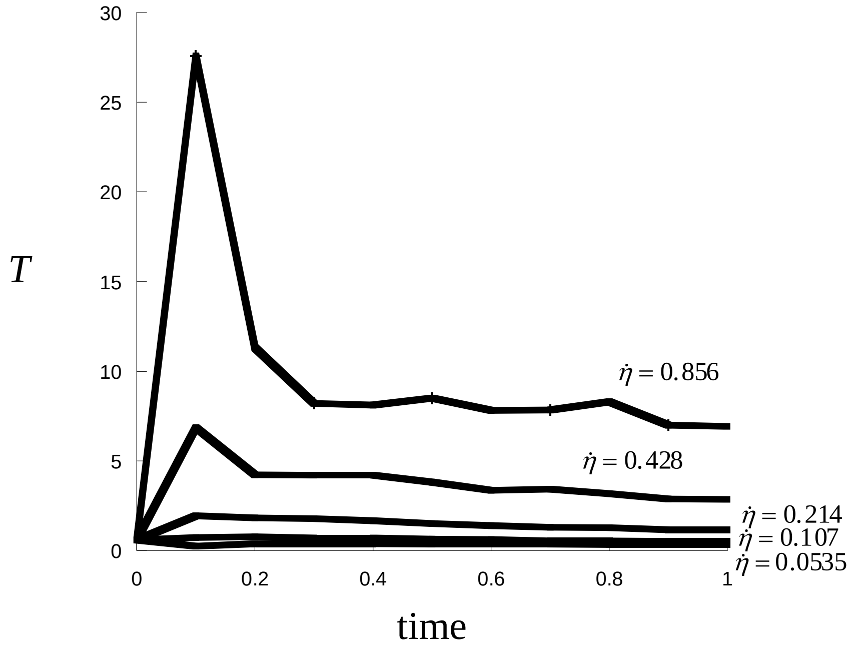

Figure 4.11. Thermal temperature of fragments in the laboratory frame versus expansion time for the expansion rates 0.0535, 0.107, 0.214, 0.428 and 0.856. $N = 4225$, $\rho_0 = 0.75$ and $T_0 = 0.6$. The time is reduced.

In Fig. 4.12 the same dependence for the rate 0.107 and for N = 67 600, 135 424 and 541 696 is given. It resembles the one for N = 4225, and one can notice that the temperatures in these Figures grow proportionally to $\sqrt{N}$ which is an interesting fact but what should be expected because thermal fluctuations grow proportionally to $\sqrt{N}$ (Landau 1981), Table 4.2. In (Stepanov 1995) it was shown that in condensed matter, the fluctuations are proportional to $\sqrt{N}$ till $N = N_0$ and are constant at larger N. The thermal temperature in the expanding system frame does not depend on the system size because the configuration temperature equals 0.30(1) with a high accuracy for almost all system sizes. For N = 541 696 and the rate $\dot{\eta} = 0.856$ the configuration temperature is again slightly higher: 0.34(5).

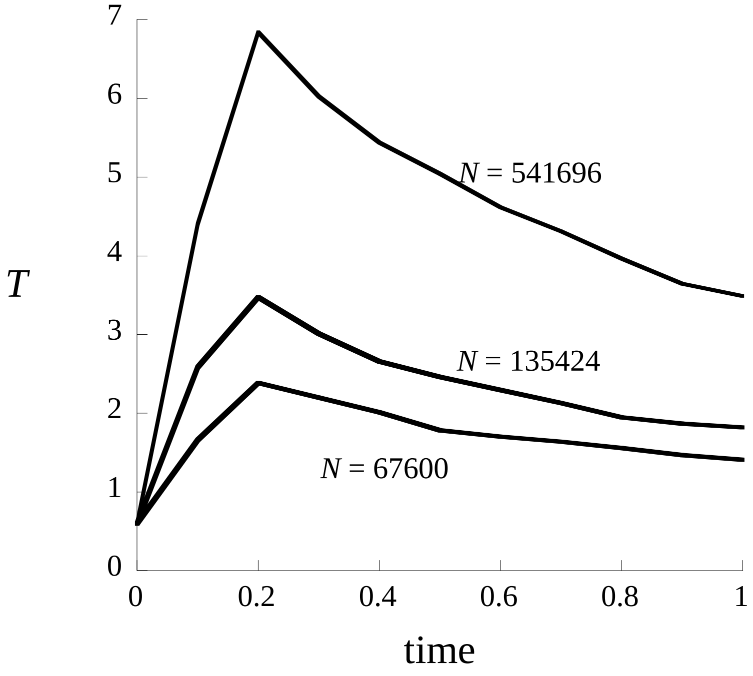

Figure 4.12. Thermal temperature of fragments in the laboratory frame versus reduced expansion time for the expansion rate 0.107. From top to bottom: N = 541 696, N = 135 424, N = 67 600, ρ_0 = 0.75 and T_0 = 0.6.

Table 4.2. The ratio of the thermal temperatures of fragments in the laboratory frame for N = 541696, T_3, and N = 67 600, T_1; $\sqrt{\frac{541696}{67600}} = 2.83$.

Time	0.1	0.2	0.3	0.4	0.5	0.6	0.7	0.8	0.9	1.0
T_3	4.4032	6.8426	6.0252	5.4384	5.0414	4.6157	4.3105	3.9662	3.6453	3.4882
T_1	1.6604	2.3832	2.1991	2.0107	1.7842	1.7051	1.6384	1.5602	1.4679	1.4017
T_3/T_1	2.6520	2.8712	2.7399	2.7048	2.8256	2.7070	2.6310	2.5422	2.4833	2.4884

4.6 Expansion Pathway

As mentioned in Chapter 3, the configurational temperature is a useful diagnostic tool in simulation of a many particle system because it tracks the temperature of the system even when it is not in global thermodynamic equilibrium. In Fig. 4.13 we show the dependence of the thermal temperature and configurational temperature on the density during a simulation for the expansion rate $\dot{\eta}$ = 0.107. The thermal temperature plot resembles well that in Fig. 4.2, it oscillates along the triple-point line, $T \approx 0.4$. As expected, the configurational temperature tracks the thermal temperature even if the system is far from equilibrium. It is interesting to note that at the early stage and at the end of the expansion, the difference between both temperatures becomes very small. The thermal temperature of the system after expansion with the rate 0.107 is about 0.39, Figs. 4.2 and 4.3. The configurational temperature after the expansion is approximately 0.36.

The plot on Fig. 4.13 clearly demonstrates that one can take the configurational temperature instead of the thermal one in cases when the latter is difficult to calculate. The difference between the two temperatures is small.

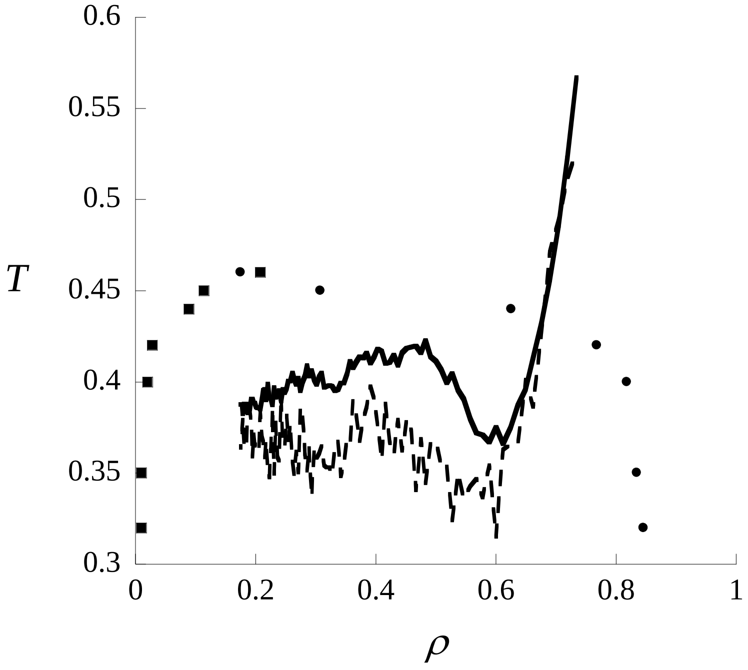

Figure 4.13. Dependence of the thermal temperature (solid line) and configurational temperature (dashed line) on density during two-dimensional MD expansion simulation by the Holian-Grady method (this work). Symbols: our binodal for LJ-spline fluid. $N = 4225$, $\dot{\eta} = 0.107$, $\rho_0 = 0.75$, $T_0 = 0.6$.

4.7 Effect of Expansion Rate

To explore the effect of changing the expansion rate on fragmentation we have explored a range of different expansion rates $\dot{\eta} = 0.0535$, 0.107, 0.214, 0.428 and 0.856. Figs. 4.14a-e show respectively the final snapshots (for two-fold expansion and hence same final density of 0.175) for the same $N = 4225$ system ($\rho_0 = 0.75$ and $T_0 = 0.6$) and same time step as used in §4.4.

One can see that the fragment size decreases with the expansion rate but their shape is approximately the same except for the rate 0.856: they are wormlike. Really, Figs. 4.7 and 4.8 confirm that. The average fragment size decreases by a factor of approximately 2 when the rate is doubled, Table 4.4. This suggests a scaling law. In §4.10 this will be studied in more detail. The final temperature of the fragments increases slightly with the expansion rate. The number of monomers increases drastically for $\dot{\eta} = 0.856$: it is about a half of the population.

The maximum cluster sizes in this case are (with increasing expansion rate): 189, 83, 43, 24 and 11.5. A correlation is evident: that size decreases twice when the expansion rate increases twice.

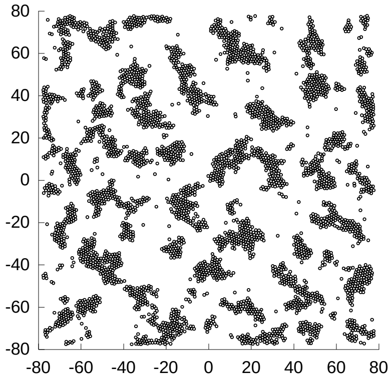

a) $\dot{\eta} = 0.0535$

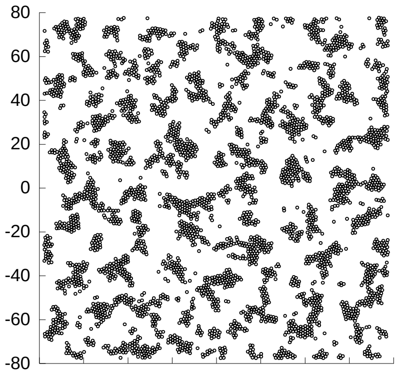

b) $\dot{\eta} = 0.107$

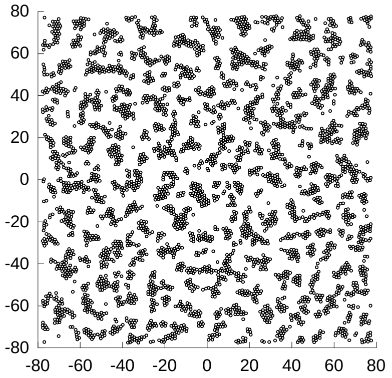

c) $\dot{\eta} = 0.214$

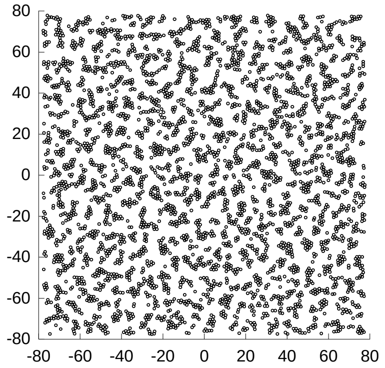

d) $\dot{\eta} = 0.428$

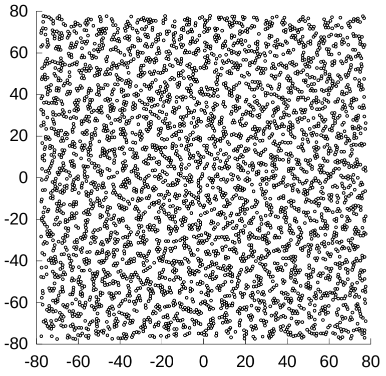

e) $\dot{\eta} = 0.856$

Figure 4.14. Final particle positions for MD two-fold expansion, $N = 4225$, $\rho_0 = 0.75$ and $T_0 = 0.6$. a) $\dot{\eta} = 0.0535$, expansion time $t = 20$, $T \approx 0.38$; b) $\dot{\eta} = 0.107$, expansion time $t = 10$, $T \approx 0.38$; c) $\dot{\eta} = 0.214$, $t = 5$, $T \approx 0.40$; d) $\dot{\eta} = 0.428$, $t = 2.5$, $T \approx 0.45$; e) $\dot{\eta} = 0.856$, $t = 1.25$, $T \approx 0.48$.

4.8 Fragmentation – Sensitivity to Initial Microscopic State

There are many sets of coordinates $\{\mathbf{r_i}\}$ and momenta $\{\mathbf{p_i}\}$ consistent with the fixed value of ρ_0 and T_0; this is simply a consequence of statistical mechanics. It is of interest to see how reproducible the fragmentation is if we change the microscopic state for a fixed thermodynamic condition. One way to do this is to change the seed in the random number generator used to create initial momenta. The set of coordinates and momenta which corresponds to a certain seed number can be called realisation. We have chosen another route. We equilibrated the system at a slightly higher temperature, then changed the temperature back to the initial one and again equilibrated. That is, if the initial temperature was 1.0, the first realisation was increasing it to 1.05 and then back to 1.0, the second realisation was increasing it to 1.10, etc. Then we averaged the results of the simulations over the number of realisations. We have run simulations with 1, 5, 10 and 20 realisations. In Table 4.3 the dependence of the average fragment size and the temperature of the fragments on the number of realisations is given. One can see that 10 realisations can be taken to produce reliable results and, therefore, we use 10 realisations in the remainder of our simulations.

Table 4.3. Dependence of the average cluster size, <μ>, and the final temperature, T, on the number of realisations (initial configurations of the system), at various expansion rates, $\dot{\eta}$, N = 4225. ρ = 0.75, T = 0.6. In brackets, standard deviation.

		$\dot{\eta} = 0.107$		$\dot{\eta} = 0.214$	
		<μ>	T	<μ>	T
Number of Realisations	1	23.6	0.42	7.7	0.38
	5	18.0(4)	0.36(2)	7.8(2)	0.38(2)
	10	17.9(5)	0.37(2)	8.0(3)	0.37(1)
	20	16.2(16)	0.37(2)	7.0(6)	0.37(1)

Simulations with 10 realisations produce the same final temperature and approximately the same cluster number as those with 20 realisations. Examples of the cumulative distributions for $\dot{\eta} = 0.107$ and 0.214 for different number of realisations obtained in our work are given in Figs.

4.15 and 4.16. In Figs. 4.15 and 4.16 there is a satisfactory agreement between the results obtained by 10 and 20 realisations. At $\dot{\eta} = 0.107$, for large cluster numbers they even coincide. Our predecessors took not more than 5 realisations (Ashurst 1999a,b). In Fig. 4.16 the maximum cluster size for 1 and 5 realisations ranges from 80 to 120 particles: this is in a complete agreement with (Ashurst 1999) who tried 1 and 3 realisations for the same system. For 10 and 20 realisations, the maximum cluster is about 130 particles.

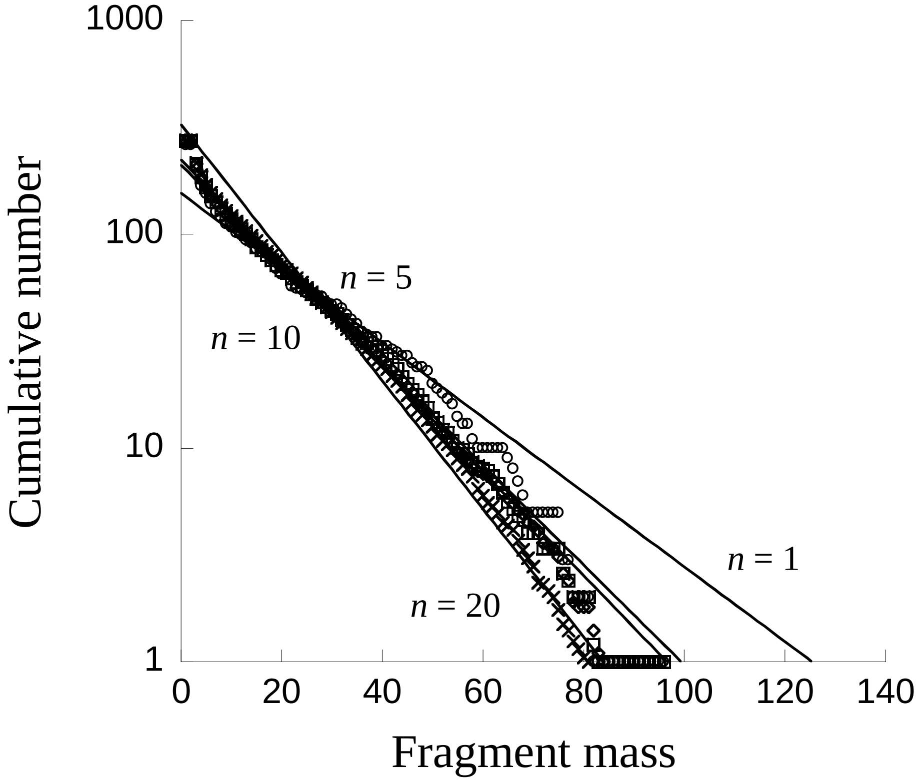

Figure 4.15. Cumulative number of clusters of mass M or greater vs M at the end of two-dimensional MD expansion by the Holian-Grady method. N = 4225, $\dot{\eta} = 0.107$, ρ_0 = 0.75 and T_0 = 0.6. The curves are for n = 1, 5, 10 and 20 realisations. Straight lines are trend lines.

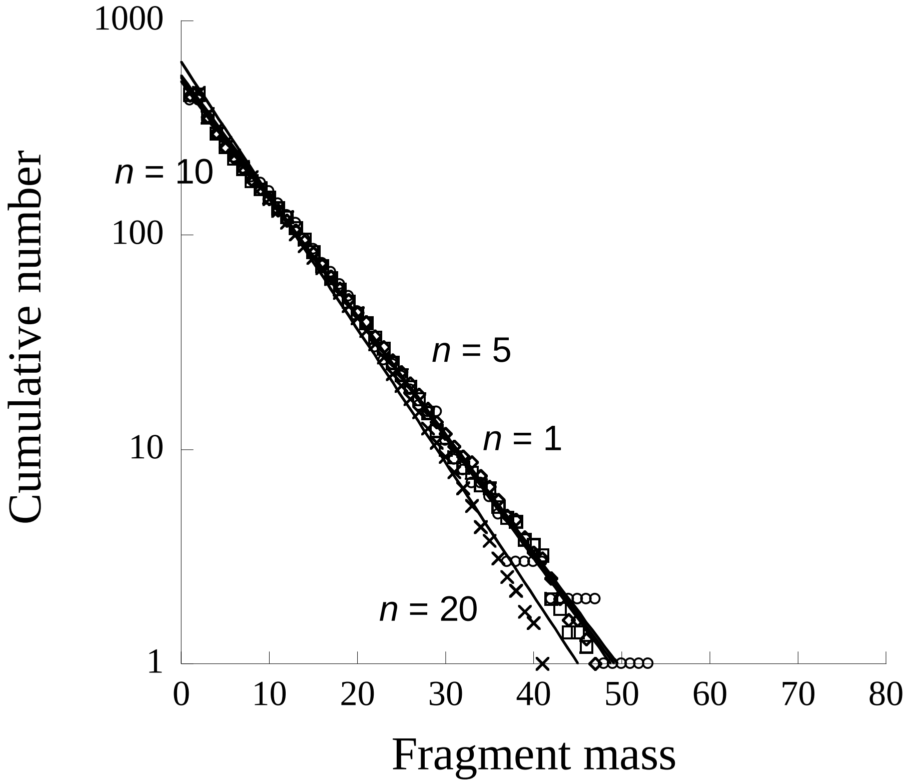

Figure 4.16. Cumulative number of clusters of mass M or greater vs M at the end of two-dimensional MD expansion by the Holian-Grady method. $N = 4225$, $\dot{\eta} = 0.214$, $\rho_0 = 0.75$ and $T_0 = 0.6$. The curves are for n = 1, 5, 10 and 20 realisations. Straight lines are trend lines.

4.9 Fragmentation – Sensitivity to Initial Thermodynamic State

It is important to know how the distribution and properties of fragments depend on the initial temperature and pressure of the system. Therefore, we performed simulations for the systems with a constant density and varying temperature, and with a constant temperature and varying density (for 10 realisations). The number of particles N was 4225 and the expansion rate, $\dot{\eta}$, was 0.107. The first series of simulations was for a constant initial density $\rho_0 = 0.75$ and the initial temperatures T_0 = 0.7, 0.8, 0.9 and 1.0. The second series of simulations was for a constant initial temperature T_0 = 0.6 and the initial densities ρ_0 = 0.7, 0.6, 0.5, 0.4.

Snapshots of the final configurations from the first series are given in Fig. 4.17. They do not differ noticeably from each other. The cumulative distributions of clusters also do not differ much from each other, Fig. 4.18. The average cluster size obtained from those distributions, $<\mu>$, also slowly decreases with temperature: 13.2, 11.4, 10.4 and 9.5. It is interesting that the final temperature of the fragments is practically the same. For $T_0 = 0.7$, the maximum cluster is 104 particles, for $T_0 = 0.8$ it is 93, for $T_0 = 0.9$ it is 84 particles, and for $T_0 = 1.0$ it is 82 particles.

The final positions for the second series are given in Fig. 4.19. They also do not differ very much from each other but one can see that the size of fragments decreases faster than in Fig. 4.17. The values of the average cluster size, $<\mu>$, are 12.0, 9.1, 7.2 and 5.8. The dependencies of the cumulative distribution of clusters on the density also differ from each other stronger than in Fig. 4.17. For $\rho_0 = 0.7$, the maximum cluster is 85 particles, for $\rho_0 = 0.6$ it is 69, for $\rho_0 = 0.5$ it is 60 particles, and for $\rho_0 = 0.4$ it is 52 particles, Fig. 4.20. One can make a conclusion that there is a small dependence of fragmentation on the initial temperature, and a stronger dependence on the initial density. The final temperature of the fragments again is practically the same.

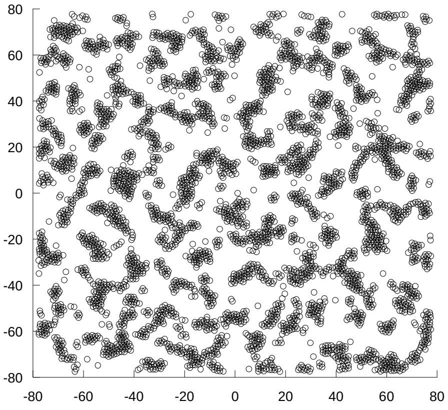

$\rho_0 = 0.75$, $T_0 = 0.7$, $T_{\mathrm{final}} = 0.51(7)$

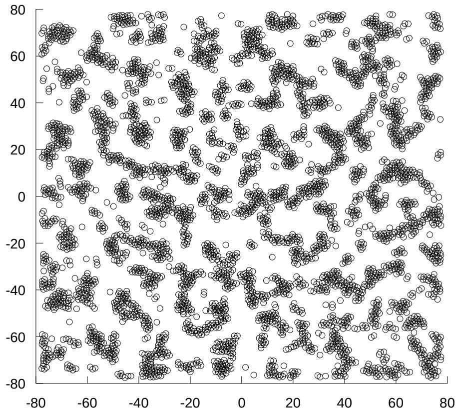

$\rho_0 = 0.75$, $T_0 = 0.8$, $T_{\mathrm{final}} = 0.52(4)$

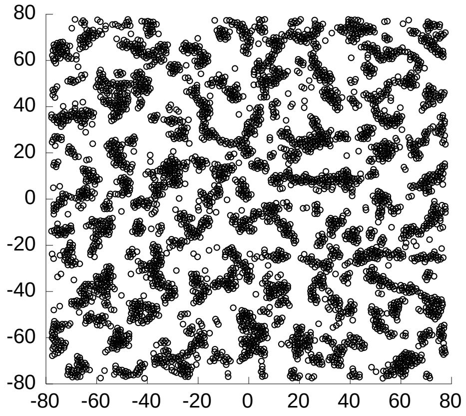

$\rho_0 = 0.75$, $T_0 = 0.9$, $T_{\mathrm{final}} = 0.46(4)$

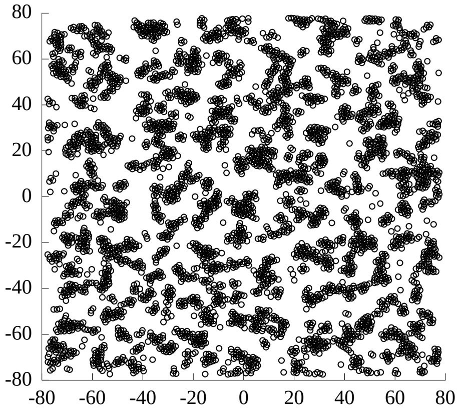

$\rho_0 = 0.75$, $T_0 = 1.0$, $T_{\mathrm{final}} = 0.46(3)$

Figure 4.17. Snapshots of final particle positions for the Holian-Grady method for the initial density $\rho_0 = 0.75$ and temperatures $T_0 = 0.7$, 0.8, 0.9 and 1.0. $N = 4225$, $\rho_{\mathrm{final}} = 0.175$, $\dot{\eta} = 0.107$. T_{final} is thermal temperature of fragments. In brackets, standard deviation.

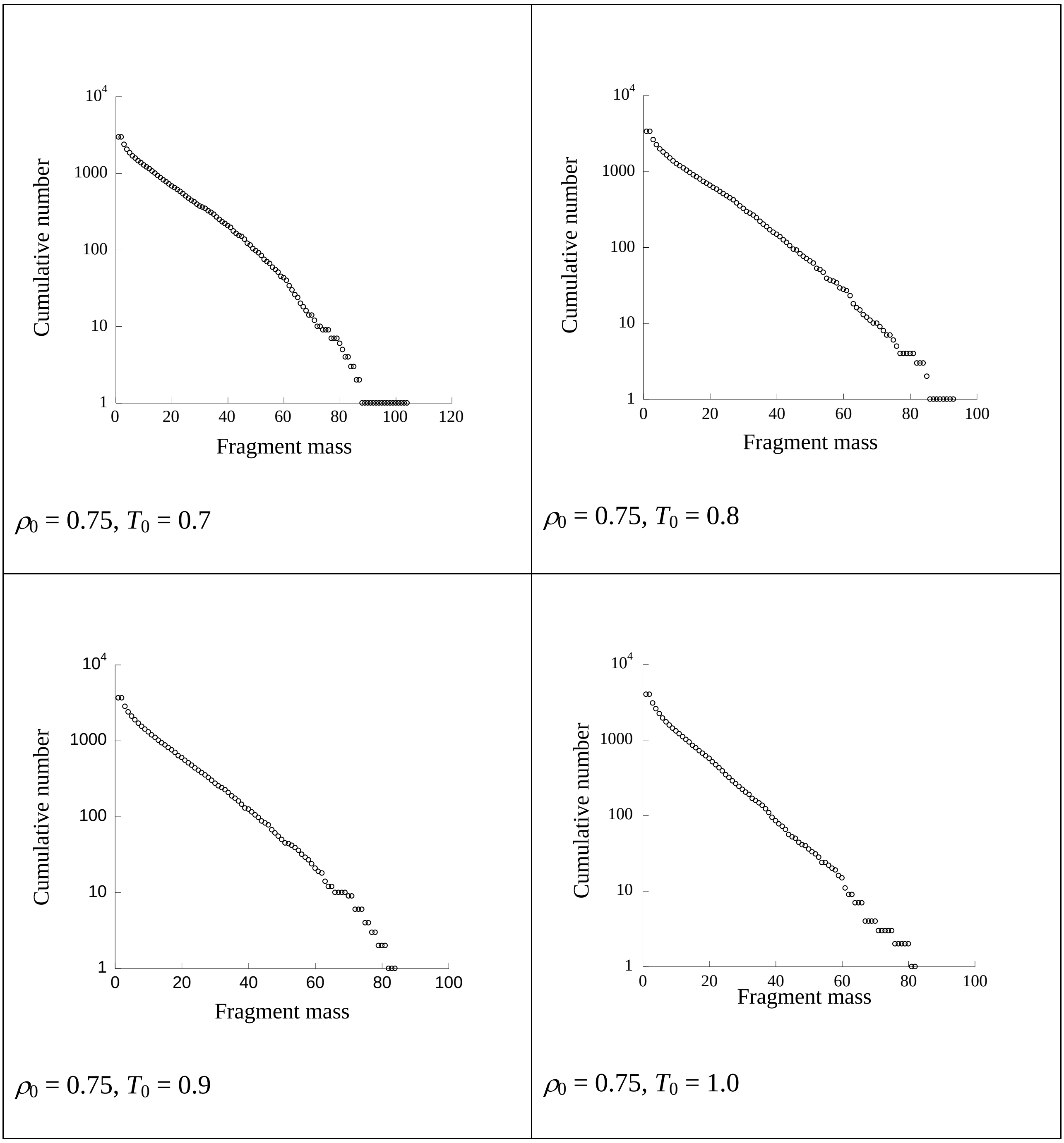

ρ_0 = 0.75, T_0 = 0.7

ρ_0 = 0.75, T_0 = 0.8

ρ_0 = 0.75, T_0 = 0.9

ρ_0 = 0.75, T_0 = 1.0

Figure 4.18. Cumulative number of clusters of mass M or greater vs M at the end of two-dimensional MD expansion by the Holian-Grady method. N = 4225, $\dot{\eta} = 0.107$. The initial density ρ_0 = 0.75 and temperatures T_0 = 0.7, 0.8, 0.9 and 1.0. The average cluster size, $<\mu>$, equals 13.2, 11.4, 10.4, and 9.5, respectively.

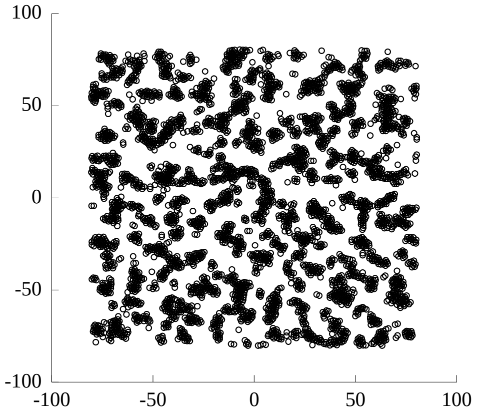

$\rho_0 = 0.7$, $T_0 = 0.6$, $T_{\text{final}} \approx 0.47(7)$

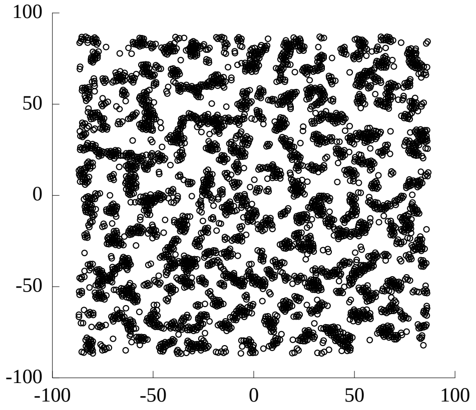

$\rho_0 = 0.6$, $T_0 = 0.6$, $T_{\text{final}} = 0.45(4)$

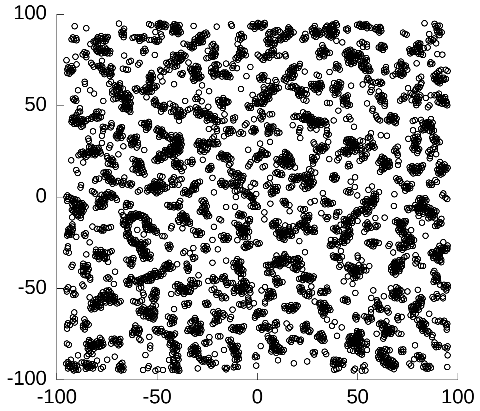

$\rho_0 = 0.5$, $T_0 = 0.6$, $T_{\text{final}} = 0.48(6)$

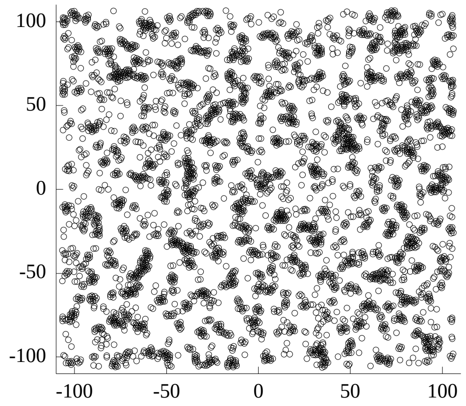

$\rho_0 = 0.4$, $T_0 = 0.6$, $T_{\text{final}} = 0.48(4)$

Figure 4.19. Snapshots of final particle positions for the Holian-Grady method for the initial temperature $T_0 = 0.6$ and densities $\rho_0 = 0.7$, 0.6, 0.5 and 0.4. $N = 4225$, $\dot{\eta} = 0.107$. T_{final} is thermal temperature of fragments.

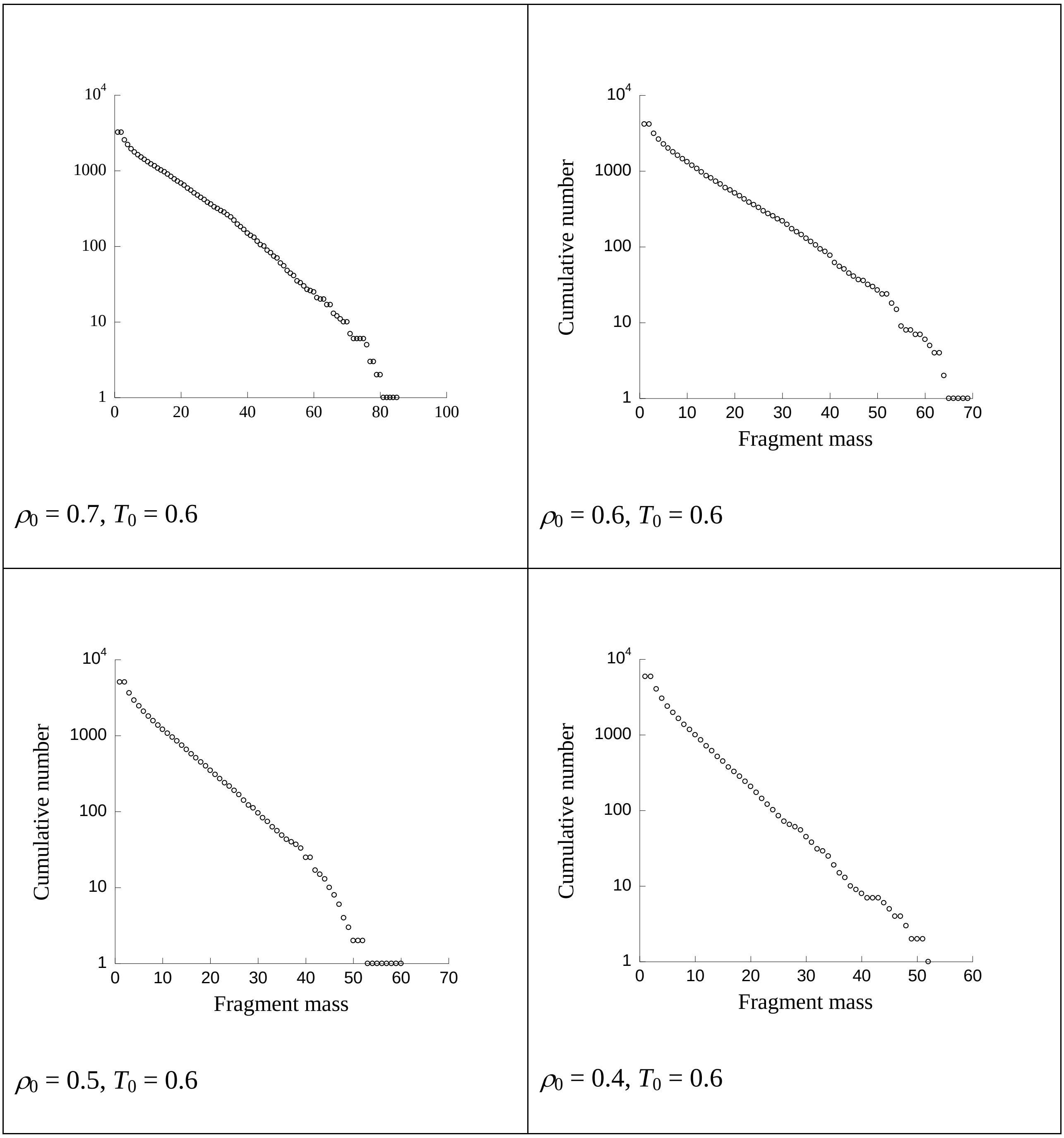

$\rho_0 = 0.7$, $T_0 = 0.6$

$\rho_0 = 0.6$, $T_0 = 0.6$

$\rho_0 = 0.5$, $T_0 = 0.6$

$\rho_0 = 0.4$, $T_0 = 0.6$

Figure 4.20. Cumulative number of clusters of mass M or greater vs M at the end of two-dimensional MD expansion by the Holian-Grady method. $N = 4225$, $\dot{\eta} = 0.107$. The initial temperature $T_0 = 0.6$ and densities $\rho_0 = 0.7, 0.6, 0.5$ and 0.4. The average cluster size, $<\mu>$, is 12.0, 9.1, 7.2, and 5.8, respectively.

4.10 Dependence of the Average Cluster Size on the System Size and Expansion Rate

We explored much larger systems than Holian and Grady (1988) to check and extend their results: from 1089 to 541 696 particles. Our results were averaged over 10 realisations in each case and the time step in the expansion ranged from 0.002 for $\dot{\eta} = 0.0535$ to 0.000125 for $\dot{\eta} = 0.856$. An interesting result is obtained: the average cluster size depends weakly on the system size, and strongly on the expansion rate, as shown in Table 4.4.

Table 4.4. Dependence of the average cluster size on the expansion rate for systems of different sizes, ρ = 0.75, T= 0.6. In brackets, standard deviation.

Rate \ Size	**0.0535**	**0.107**	**0.214**	**0.428**	**0.856**
1089	40.6(66)	17.9(13)	9.4(18)	4.0(2)	1.6(1)
2116	36.8(36)	17.3(20)	7.5(4)	3.0(2)	1.5(1)
4225	41.4(21)	17.9(5)	8.0(3)	3.0(1)	1.4(1)
8464	41.4(57)	16.7(16)	7.2(9)	3.0(3)	1.4(1)
16900	41.8(23)	17.7(6)	7.2(4)	3.1(1)	1.3(1)
33856	38.5(17)	15.6(9)	7.0(2)	3.0(1)	1.2(1)
67600	35.6(31)	15.7(8)	7.0(2)	2.8(1)	1.23(5)
135424	32.4(60)	14.9(4)	6.5(3)	2.81(4)	1.25(3)
541696	31.6(11)	13.3(4)	5.5(1)	2.64(5)	1.14(4)

For N = 541 696, the number of monomers is anomalously high for $\dot{\eta} = 0.856$: it is about 151 240. The maximum cluster sizes for this system are (with increasing expansion): 328, 142, 70, 34 and 16. The same correlation is evident as for N = 4225, §4.7: that size decreases twice when the expansion rate increases twice, and the maximum cluster for this system is not much smaller than that for 541696 particles.

In science and engineering simple models of fragmentation are required which give the average fragment mass as a function of the expansion rate. Grady proposed a simple model which balances the kinetic energy of expansion of a fluid sphere and the potential energy of its surface (Grady 1982, Holian and Grady 1988). For a two-dimensional droplet, the kinetic energy of expansion per unit mass is $\frac{R^2\dot{\eta}^2}{4}$. The potential energy of its surface per unit mass is $\frac{r_\mathrm{c}E_\mathrm{coh}}{R}$, where r_c is the thickness of the surface and E_coh is the cohesive energy. One then minimises the sum of these energies for the minimum density of the surface and obtains the mean cluster size:

$$\langle\mu\rangle = \frac{\pi\rho}{2}\left(\frac{2r_\mathrm{c}E_\mathrm{coh}}{\dot{\eta}^2}\right)^{2/3} \tag{4.11}$$

Eq. (4.11) can be evaluated for atomistic systems: $E_\mathrm{coh} \approx n_\mathrm{d}\varepsilon/2m$, where n_d is the nearest neighbours number (6 for 2 dimensions), ε is the inter-atomic potential well depth, and $r_\mathrm{c} \approx \sigma$. The mean cluster size is therefore:

$$\langle\mu\rangle = (0.75)6^{2/3}\pi\dot{\eta}^{-4/3} \tag{4.12}$$

Holian and Grady (1988) obtained the dependence of $<\mu>$ on $\dot{\eta}$ for only one system size, N = 4225. Their linear fit to that dependence had the slope about –4/3. Our dependence of the average cluster size on the expansion rate for N = 4225 and for the same initial temperature and density is plotted in Fig. 4.21. It differs slightly from the result in Holian and Grady (1988): it equals –1.23(0.4). We performed the investigation for many system sizes, from 1089 to 541 696 particles for ρ_0 = 0.75 and T_0 = 0.6. The results are given in Table 4.5. The scaling exponent does not depend on the system size and approximately equals –1.22(2) which is close to Grady's model. Our results seem to be more reliable because they are obtained by averaging over 10 realisations but Holian and Grady did only one realisation. In Fig. 4.22 the dependence of the average cluster size on the expansion rate for N = 541 696 is presented. The simulations points lie exactly on the line, as they do for 4225 particles, i.e., there is practically no scatter. So, our results support the power law of Grady's model in a very broad range of system sizes. The scaling exponent is close to that of Grady's model.

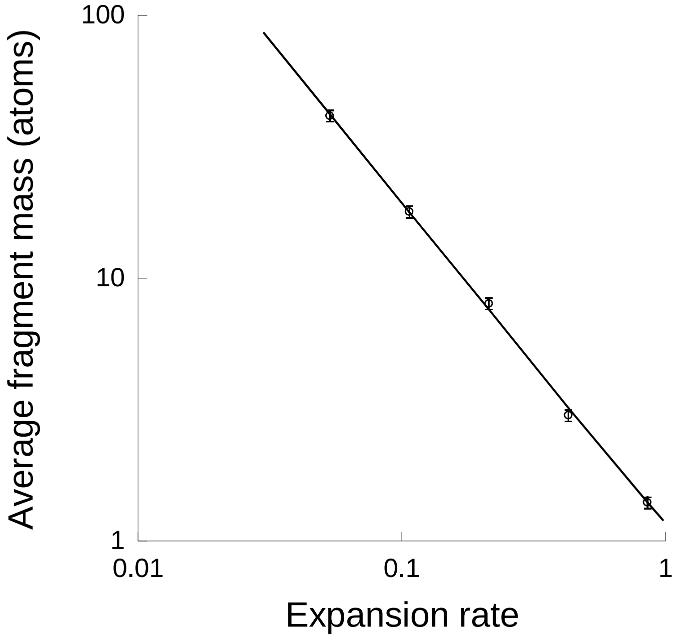

Figure 4.21. Dependence of the average cluster size on the expansion rate, $\dot{\eta}$, $N = 4225$, $\rho_0 = 0.75$, $T_0 = 0.6$. The line has slope –1.23(0.4).

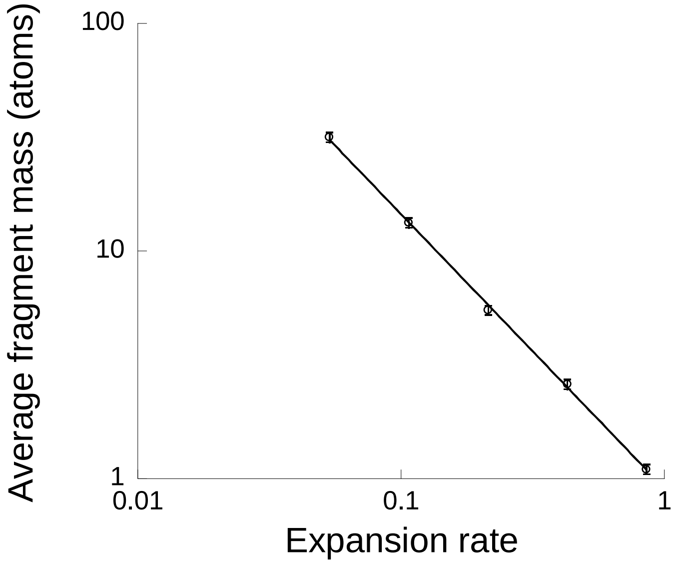

Figure 4.22. Dependence of the average cluster size on the expansion rate, $\dot{\eta}$, $N = 541\ 656$, $\rho_0 = 0.75$, $T_0 = 0.6$. The line has slope –1.20(0.4).

Table 4.5. Dependence of the scaling exponent in Grady's model on the size of the system, ρ_0 = 0.75, T_0 = 0.6.

Size, *N*	**1089**	**2116**	**4225**	**8464**	**16900**	**33856**	**67600**	**135424**	**541696**
Slope	–1.15	–1.20	–1.23	–1.22	–1.25	–1.24	–1.23	–1.19	–1.20

The Grady's model predicts that the largest fragment size in a two-dimensional system is proportional to $\dot{\eta}^{-1}$ (Ashurst and Holian 1999a). Our simulations for $N \leq 541\ 696$ confirm very well those of Ashurst and Holian for $N = 4225$. The results are presented in Fig. 4.23 and Table 4.6. The average scaling exponent is –1.04(7).

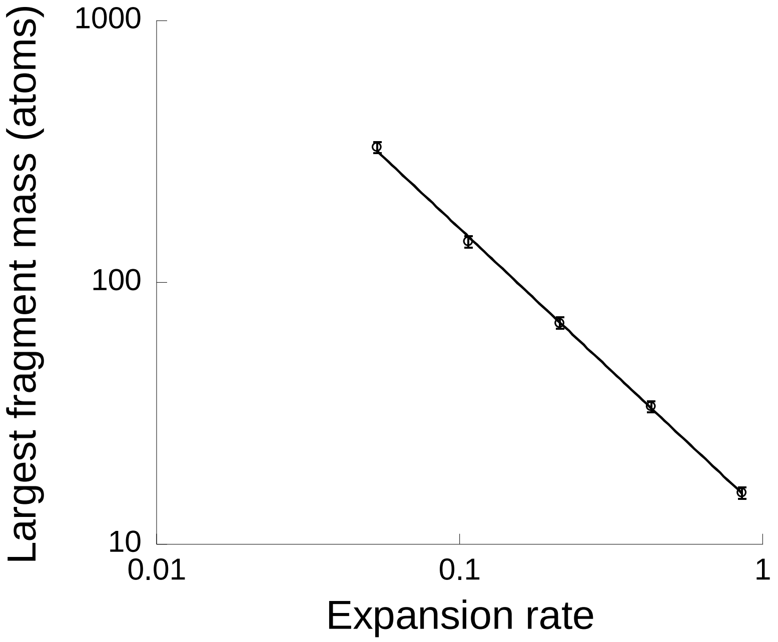

Figure 4.23. Dependence of the largest cluster size on the expansion rate, $\dot{\eta}$, $N = 541\ 656$, ρ_0 = 0.75, T_0 = 0.6. The line has slope –1.09(0.4).

Table 4.6. Dependence of the scaling exponent in Grady's model on the size of the system for the largest fragment, ρ_0 = 0.75, T_0 = 0.6.

Size, *N*	**1089**	**2116**	**4225**	**8464**	**16900**	**33856**	**67600**	**135424**	**541696**
Slope	–0.93	–1.17	–0.99	–0.99	–1.05	–1.03	–1.06	–1.07	–1.09

In Fig. 4.24 the cumulative number of fragments versus fragment mass is given for *N* = 541 656 and five expansion rates. The distributions are qualitatively similar to those for lower *N*. The maximum cluster size decreases sharply with the expansion rate: from 550 to 17. The maximum cluster size at $\dot{\eta} = 0.107$ is 170, and at $\dot{\eta} = 0.214$ it is 90. Compared with the corresponding values for *N* = 4225: 130 for $\dot{\eta} = 0.107$ and 55 for $\dot{\eta} = 0.214$, one can see that this size does not increase much with increasing size.

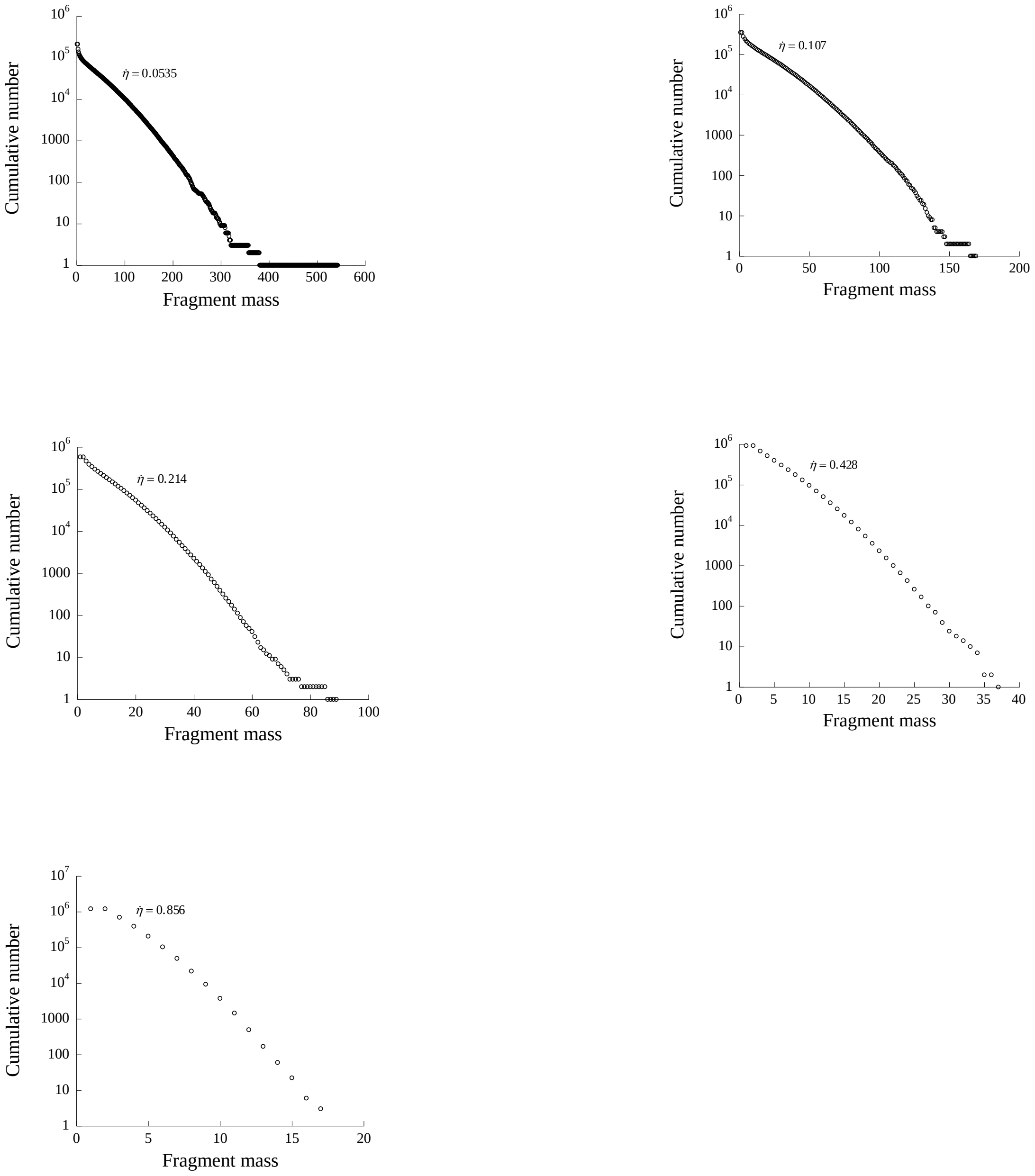

Figure 4.24. Cumulative distribution of fragments for N = 541 656, ρ_0 = 0.75 and T_0 = 0.6 at various expansion rates in the Holian-Grady method for 10 realisations.

4.11 Expansion Pathway in the ρ – T Plane

It is of interest to see what phases on the phase diagram correspond to the density and temperature of the expanding system, how different is the state of the expanding system from that of the equilibrium one, and how the equilibrium system influences the expanding one. We plotted on the phase diagram the density and temperature of the system with $N = 4225$ during the expansion at the rate $\dot{\eta} = 0.107$ from the initial state at 0.1, 0.2, ... , 0.9 of the expansion time, Fig. 4.25.

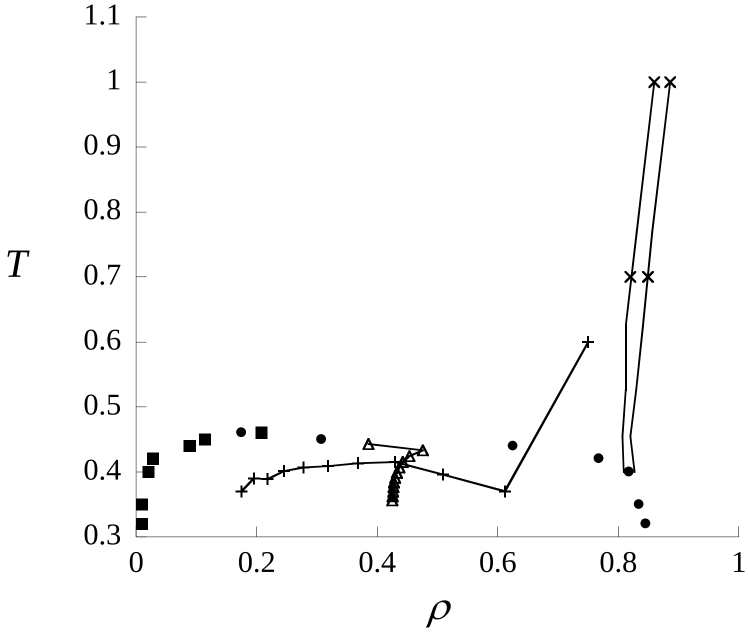

Figure 4.25. Thermodynamic pathway (bold line) on LJ-spline phase diagram. $N = 4225$, $\rho_0 = 0.75$, $T_0 = 0.6$ and $\dot{\eta} = 0.107$. In the middle, triangles, the law of rectilinear diameters. On the right hand side, the liquid – solid curves of the phase diagram.

In Fig. 4.26 we present system snapshots along the expansion path together with the equilibrium states sampled from the same state points. The equilibrium states were taken as the averages of 10 simulations with different initial conditions. Non-equilibrium states at $t = 1000 - 2000$ consist of coexisting solid and liquid, then the number of solid fragments rapidly decreases and they become liquid-like ones. Non-equilibrium states until $t = 8000$ are much more uniform, have much smaller voids and have much smaller and more elongated fragments (that should be expected – far from equilibrium fragments are far from spherical form and their size should be smaller). After $t = 6000$ the difference becomes much smaller. The equilibrium states exhibit solid, liquid and gas phases.

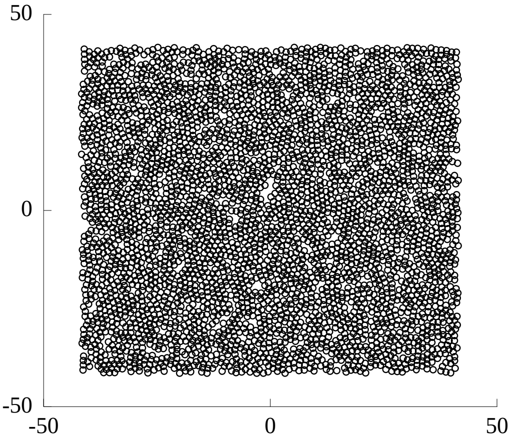 $t = 1000$, $\rho = 0.612$, $T \approx 0.38$.	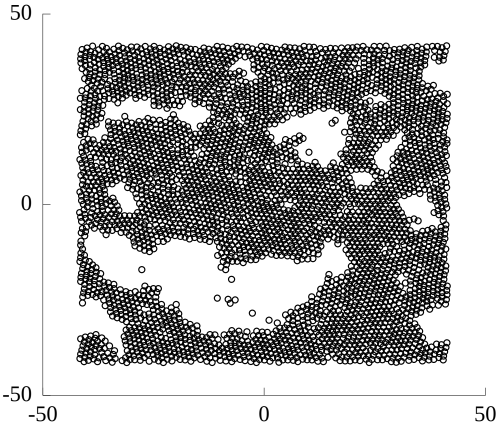 $\rho = 0.612$, $T = 0.38$. Equilibrium.
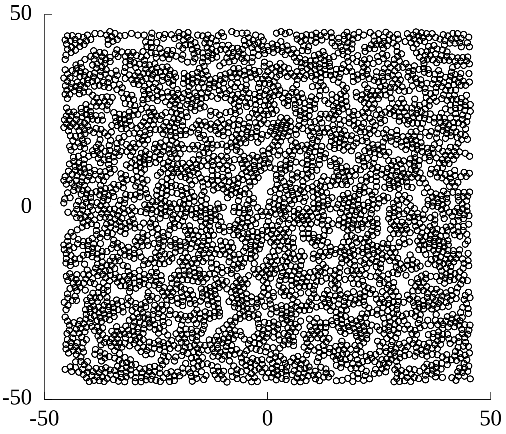 $t = 2000$, $\rho = 0.509$, $T \approx 0.40$.	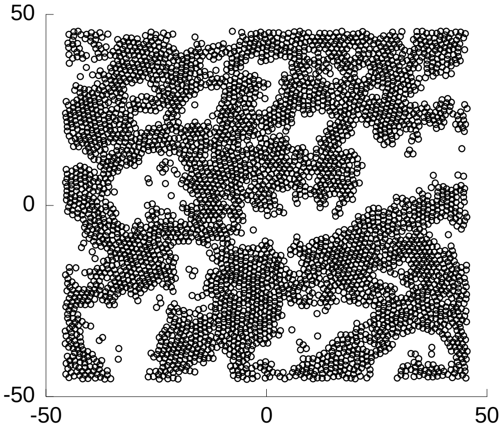 $\rho = 0.509$, $T = 0.40$. Equilibrium.

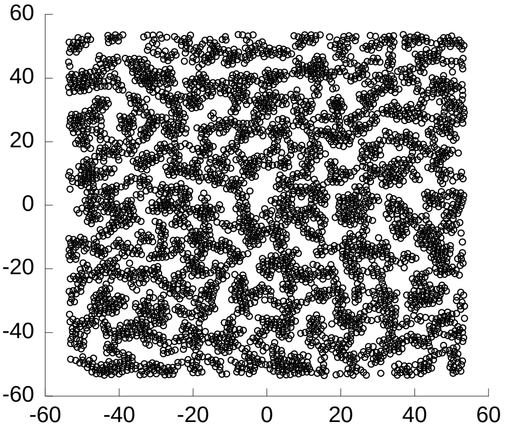

t = 4000, *ρ* = 0.368, *T* ≈ 0.41.

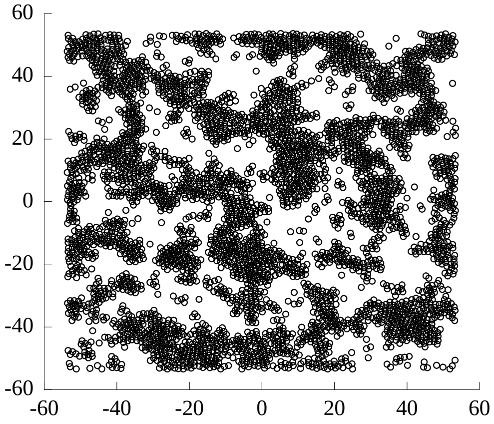

ρ = 0.368, *T* = 0.41. Equilibrium.

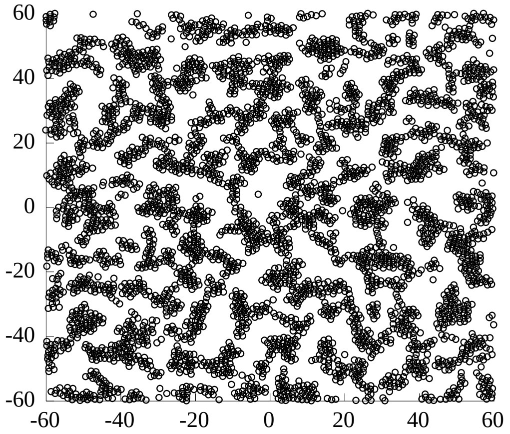

t = 6000, *ρ* = 0.278, *T* ≈ 0.41.

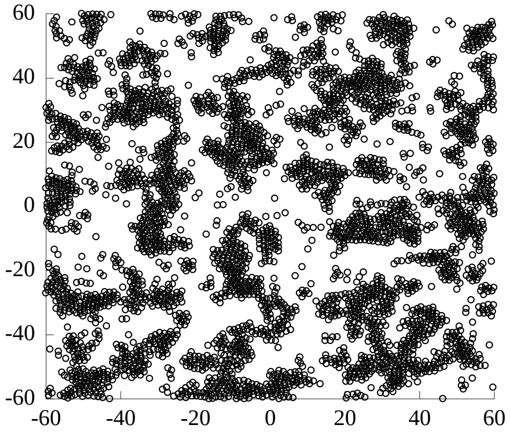

ρ = 0.278, *T* = 0.41.Equilibrium.

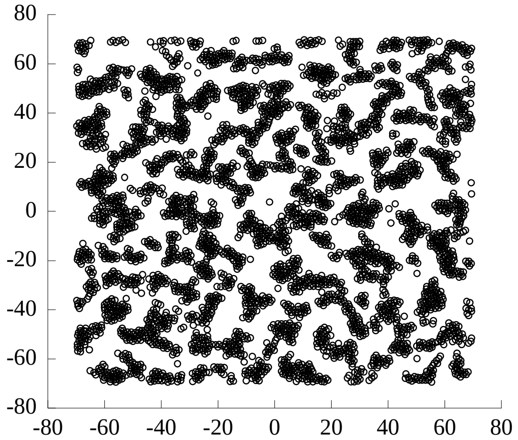

t = 8000, $\rho = 0.218$, *T* ≈ 0.39.

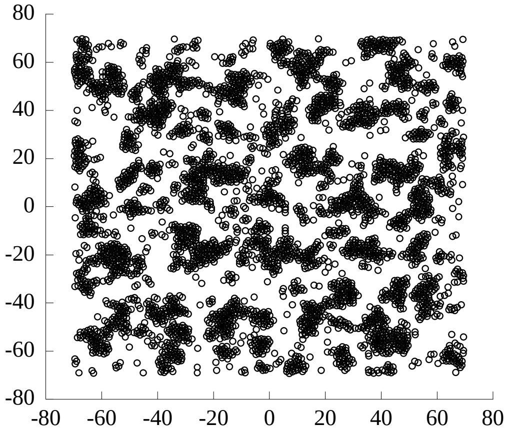

$\rho = 0.218$, $T = 0.39$. Equilibrium.

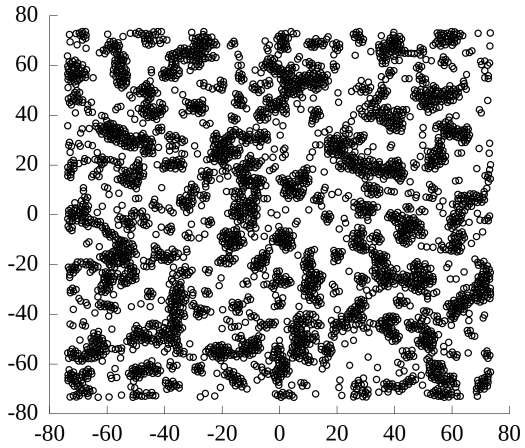

t = 9000, $\rho = 0.195$, *T* ≈ 0.39.

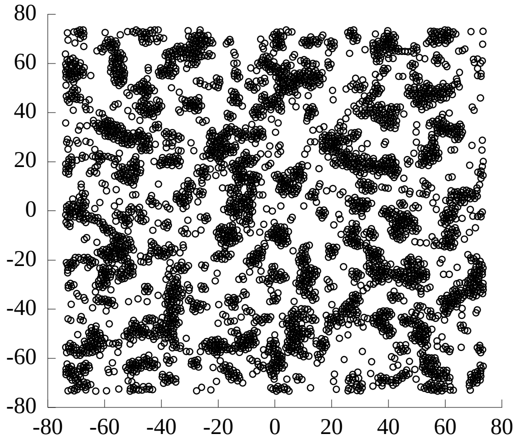

$\rho = 0.195$, $T = 0.39$. Equilibrium.

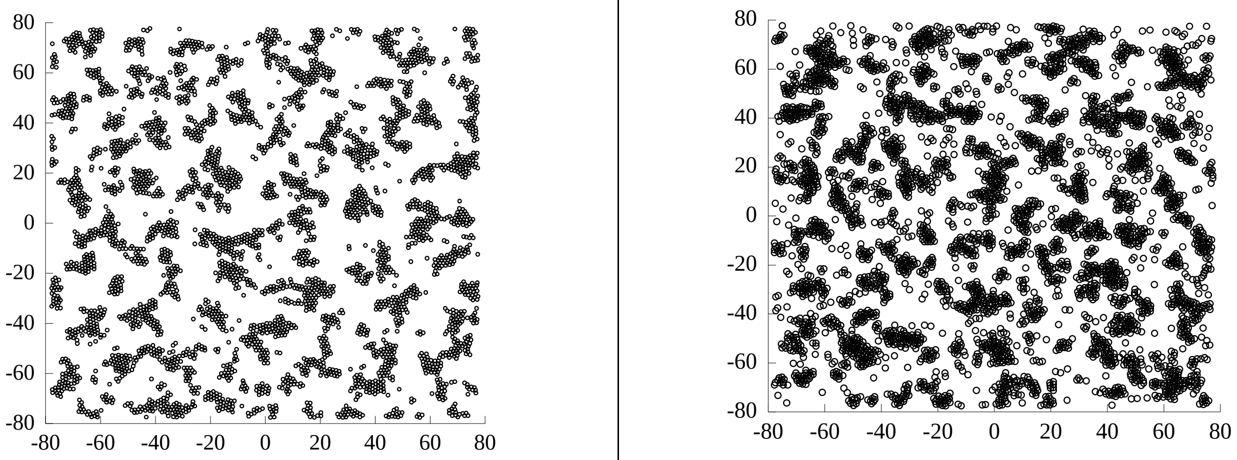

t = 10 000, $\rho = 0.175$, $T \approx 0.37$.

$\rho = 0.175$, $T = 0.37$. Equilibrium.

Figure 4.26. Particle positions along the expansion path in the Holian and Grady method (on the left) and in equilibrium at the same points of the expansion pathway (on the right). $N = 4225$, ρ_0 = 0.75 and $T_0 = 0.6$, and $\dot{\eta} = 0.107$.

One can see in Fig. 4.26 that a phase transition liquid – vapour occurs during the expansion by spinodal decomposition and by hydrodynamic fracture. Quenching into unstable region of the phase diagram happens during the expansion and the resulting snapshots resemble highly-connected regular patterns in spinodal decomposition until $t \approx 4000$ (Abraham 1986). Then their break up into clusters happens.

To examine snapshots in Fig. 4.26 quantitatively we examine the dependence of the cumulative number of clusters on the fragment mass, Fig. 4.27. One can see that at the initial state, $\rho = 0.612$, the equilibrium and non-equilibrium distributions resemble each other quite well, then due to rapid destruction of the expanding system, at $\rho = 0.509$ and $\rho = 0.368$, there is a significant difference in the distributions, but after that the distributions begin to converge. Particles in the non-equilibrium case are much smaller till $\rho = 0.278$. It is interesting to notice that the fragment sizes in the equilibrium system begin quickly to decrease at $\rho = 0.278$. At the endpoint of the expansion, the distributions differ insignificantly. One can conclude that at $\rho = 0.612 - 0.509$, the equilibrium system is coexisting solid and vapour, then, at $\rho = 0.368$, it consists of many fragments and the biggest part of them are liquid like, some are solid like, and the gas phase increases; at $\rho = 0.278$, all fragments turn to liquid, and then the system gradually moves to vapour.

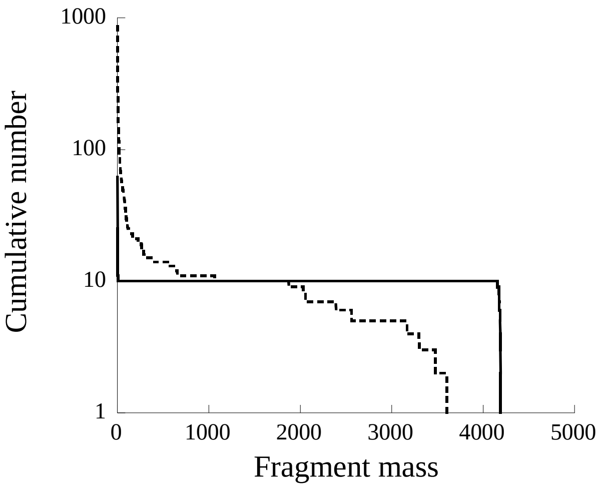

$\rho = 0.612$, $T \approx 0.38$.

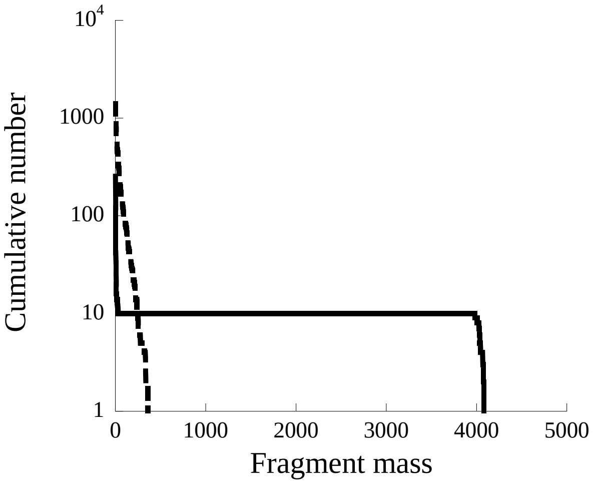

$\rho = 0.509$, $T \approx 0.40$.

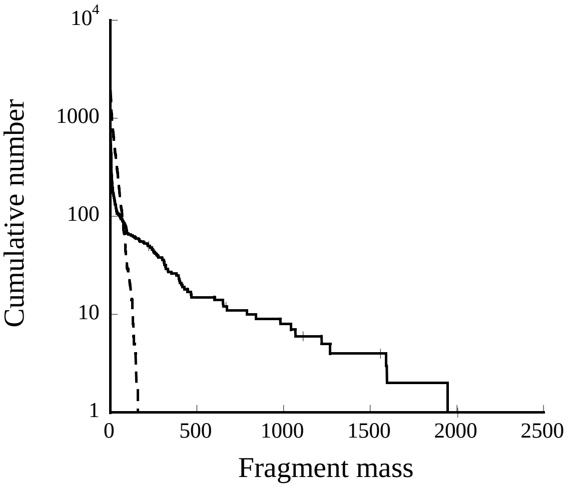

$\rho = 0.368$, $T \approx 0.41$.

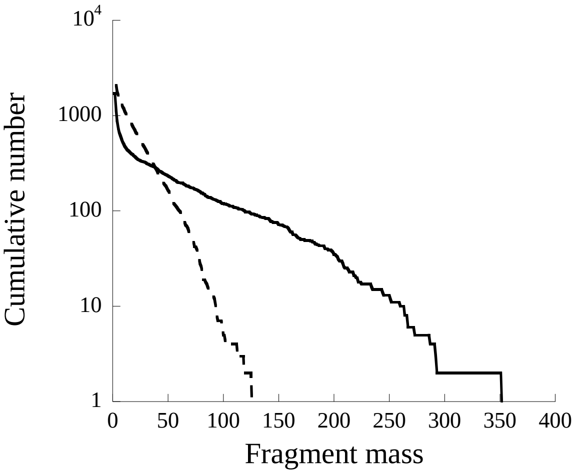

$\rho = 0.278$, $T \approx 0.41$.

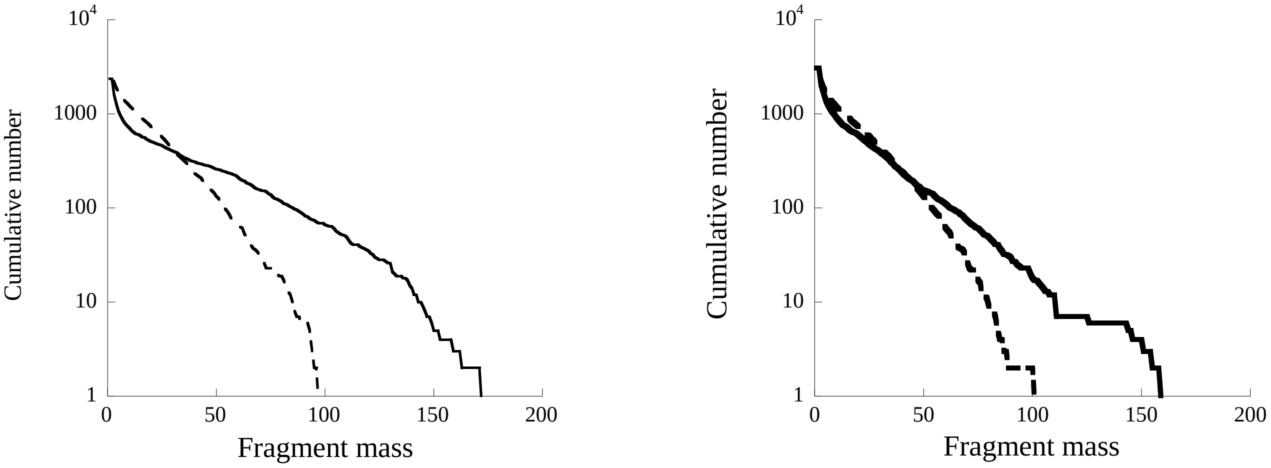

$\rho = 0.218$, $T \approx 0.39$.

$\rho = 0.195$, $T \approx 0.39$.

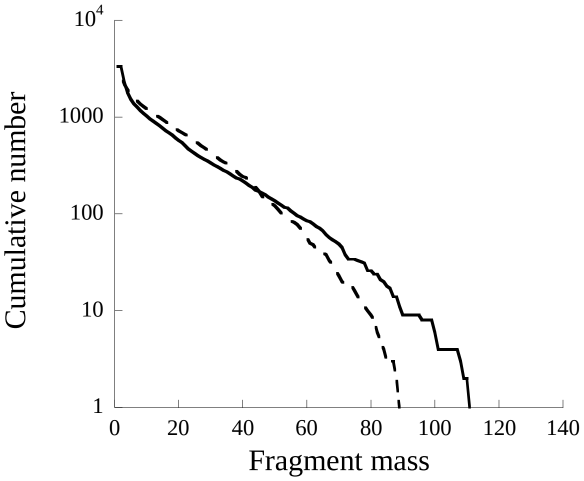

$\rho = 0.175$, $T \approx 0.37$.

Figure 4.27. Cumulative distribution of fragments along the expansion pathway for $\dot{\eta} = 0.107$. N = 4225, ρ_0 = 0.75 and T_0 = 0.6. Dashed line – non-equilibrium, solid line – equilibrium.

4.12 Holian-Grady Simulations with a 2.5 Cut LJ Potential

We also performed simulations with the Holian − Grady method but using a different potential. In this case we use a LJ potential truncated at 2.5 with no spline part. This potential was also used in a different form of expansion – the so-called Blink − Hoover method, which we investigated in Chapter 5. The system had the same size, N = 4225, and the initial state, ρ_0 = 0.75 and T_0 = 0.6, as before. The cluster bond length remained the same. Our results are presented in Fig. 4.28. The snapshots resemble very much those ones in Fig. 4.14. Again, the number of clusters increases with the expansion rate and their size decreases: $<\mu>$ = 27(2), 16(1), 8.8(2), 5.1(1) and 3.2(2). That average cluster size is only slightly larger than that for LJ-spline potential, and the average fragment size decreases proportionally to the expansion rate. The maximal cluster size also is practically the same in both cases: 233(67), 99(11), 46(3), 24(3) and 11(1). So, one can see that the change in the potential results only in a very small changes in the fragmentation. However, the slope on the plot of log$<\mu>$ versus log$\dot{\eta}$ for the average fragment is 0.78 which is far from that of the Grady's model. So this is not a universal scaling law. That plot for the maximum fragment has the slope −1.09(0.6) what agrees with this model.

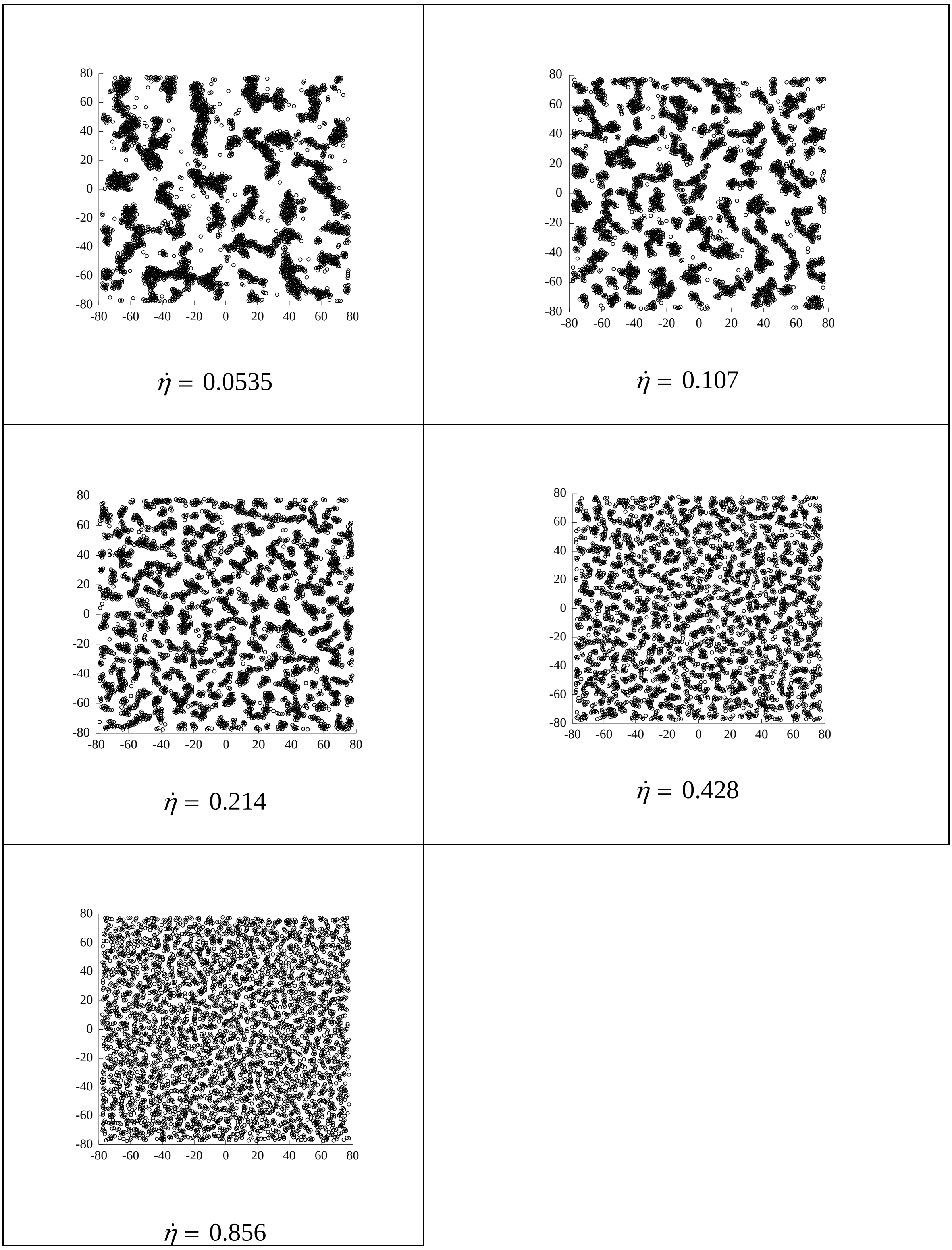

$\dot{\eta} = 0.0535$

$\dot{\eta} = 0.107$

$\dot{\eta} = 0.214$

$\dot{\eta} = 0.428$

$\dot{\eta} = 0.856$

Figure 4.28. Final positions of particles for the Holian-Grady expansion method with the LJ-cut 2.5 potential from Blink and Hoover (1985) for $N = 4225$ at various expansion rates; $\rho_0 = 0.75$ and $T_0 = 0.6$. The system was expanded approximately twofold.

4.13 Conclusions

We performed expansions by the Holian-Grady method for the systems from 1089 to 541 696 particles. Our predecessors used not more that 4225 particles. We averaged our result over 10 realisations (initial microscopic states of the system) while our predecessors used not more than 5, and therefore, our results are much more reliable because 5 and less realisations produce noticeably worse results. Our snapshots of the two-dimensional liquid reveal the presence of large vacancies within the fluid which agrees with the experiment. It is found that fragment sizes obey the bimodal distribution, this is in agreement with our predecessors. In these expansions, the relative shape anisotropy of the fragments is calculated in the course of expansion. It is found that it does not depend on the system size and in general increases with the expansion rate. Its dependence on the rate and on the time is small but at the rate 0.856 the shape anisotropy is much higher and exhibits a peak for systems of all sizes. About 15% of the fragments are almost round during the expansion for all rates. The thermal temperature of fragments in the laboratory frame has been calculated. It exhibits a peak at the initial stage of the expansion and then decreases. It grows proportionally to square root of the system size. It is shown that the thermal temperature of fragments in the expanding system frame does not depend on the time, expansion rate and the system size. The configurational temperature is calculated in our work and fruitfully employed. We investigated how the fragmentation depends on the initial temperature and pressure of the system. It is found that fragmentation depends rather weak on the initial temperature, but stronger on the initial density. It is interesting that the final temperature of the fragments is practically the same in both cases.

We performed a very extensive exploration on how the fragments size and shape depend on the expansion rate. An interesting result has been obtained: the average fragment size in the expansion by the Holian-Grady method depends weakly on the system size. One can even notice a trend: that size decreases slowly with the system size. It agrees with the Grady's model of fragmentation. The dependence of that size on the expansion rate also agrees well with the Grady's model: the scaling exponent does not depend on the system size and equals –1.22 (the Grady's model predicts −4/3). However, for the LJ potential with the cutoff 2.5, the scaling exponent equals 0.78, so Grady's model is not universal. Another interesting result is that the maximum fragment size does not depend much on the system size. According to the Grady's model, the largest fragment size in a two-dimensional system is proportional to the inverse expansion rate. Our simulations confirm that very well.

We have found out what phases on the phase diagram of LJ-spline fluid correspond to the density and temperature of the expanding system, and how they differ from the expanding system. We have come to conclusion that a phase transition liquid – vapour occurs during the expansion by spinodal decomposition and by hydrodynamic fracture. Quenching into unstable region of the phase diagram happens during the expansion and spinodal decomposition occurs: one can observe highly-connected regular patterns. Then a break up into clusters happens.

Our simulations with a different potential, a LJ potential truncated at 2.5, showed that the snapshots resemble very much the previous ones. The average cluster size is only slightly larger than that for LJ-spline potential, and the average fragment size decreases proportionally to the expansion rate. The maximal cluster size also is practically the same in both cases. However, the slope on the plot of $\log<\mu>$ versus $\log\dot{\eta}$ is far from that of the Grady's model. So this is not a universal scaling law. That plot for the maximum fragment versus $\log\dot{\eta}$ agrees with this model.

Chapter 5

Blink-Hoover Fragmentation

Blink and Hoover used a different approach to achieve essentially the same goal of MD simulation of fluid fragmentation as Holian and Grady. In their method, fragmentation of a two-dimensional Lennard-Jones fluid is initiated by removal of a confining wall, i.e. by expanding into vacuum (Blink and Hoover 1985). It is of interest to study this method and to compare it with that of Holian and Grady.

5.1 Basic Algorithm

In the Blink-Hoover method, the expansion is initiated by removing a confining boundary wall having first equilibrated a circular droplet. The expansion is then Newtonian and adiabatic because no more energy is added to the system, and the particles obey Newton's equations of motion.

In this method, the initial configuration comprised a regular hexagon lattice of atoms. The hexagon is contained within impenetrable boundaries (exact details not given in their paper). The crystal is melted by evolving thermostatted dynamics using initial random velocities. This generated an equilibrium configuration.

The Lennard-Jones equation truncated at $R_{\text{cut}} = 2.5\sigma$ was used. It has been found in the preceding chapter that the truncation had a negligible effect on the results of the simulations. The authors calculate the size of the largest fragment, the average of the ten largest fragments, and the average of the largest fragments comprising 30% of the system population for quantitative study of the fragmentation process. They found that their results agreed well with a simple Grady's model of fragmentation (Grady 1982) which balances the surface energy of the system with the kinetic energy of the fragments, §4.10.

5.2 Method of generating circular droplets

A convenient way to model the rigid boundary is to use a steep repulsive potential to prevent material from crossing an interface. In the works (Thompson et al 1984), (Shreve et al 1986) on liquid drops with surface tension the following form for this potential was adopted

$$\begin{aligned} \phi(\Delta r_i) &= \phi_{\mathrm{LJ}}(\Delta r_i) + \varepsilon, \quad && \Delta r_i < r_0 \\ &= 0, && \Delta r_i > r_0 \end{aligned} \qquad (5.1)$$

where Δr_i is the radial distance of molecule *i* from the wall, ε is the Lennard-Jones potential well depth and $r_o = 2^{1/6}\sigma$ is the separation at the minimum in the LJ potential. This potential is zero when the molecule-wall distance is greater than r_o.

In our work we have explored two different methods of confining the fluid to circle: a short ranged repulsive potential and elastic boundaries. We chose the following repulsive potential and force:

$$U^{\mathrm{rep}} = \varepsilon\left(1 - \frac{(\delta r)^2}{\sigma^2}\right)^4 \qquad (5.2)$$

where $\delta r = \left| R - \sqrt{x_i^2 + y_i^2} \right|$ and *R* is the radius of the system, hence

$$\begin{aligned} F_i^x &= -\frac{8\varepsilon}{\sigma^2} x_i \left(1 - \frac{(\delta r)^2}{\sigma^2}\right)^3 \frac{\delta r}{R} \\ F_i^y &= -\frac{8\varepsilon}{\sigma^2} y_i \left(1 - \frac{(\delta r)^2}{\sigma^2}\right)^3 \frac{\delta r}{R} \end{aligned} \qquad (5.3)$$

This potential turns on when $\delta r < \sigma$. The pressure exerted at the wall (only calculated in the repulsive-wall case) is

$$\frac{\sum_i F_i^{\text{boundary}}}{2\pi R} \qquad (5.4)$$

While straightforward in principle, this type of confining potential has some drawbacks:

1) There are now two adjustable parameters to be specified: σ and ε (these are not the LJ ones).
2) Particles can still penetrate the walls.

In the elastically reflecting boundary conditions, a particle is reflected from the wall at the same angle as that between the incident velocity and normal to the wall, see Fig. 5.1.

The elastic boundary conditions are simple to implement and have no adjustable parameters and in principle conserve energy. In practice, one observes spikes in the energy versus time plot. This is well known in hard sphere simulations. It can be corrected but it is not necessary to do so because it does not influence the results significantly. One could also use circular mirror boundary conditions though we have not explored that option in this work.

5.2.1. Equilibration results

It is convenient to begin a simulation from an ordered crystalline state. It is impossible to place the particles regularly inside the circle hence we position them into a polygon inscribed into the circle. A hexagonal array is simple and we, therefore, follow (Blink 1985) in starting our equilibration from a hexagonal lattice. The hexagon was placed into a circle of the size that results in the required density.

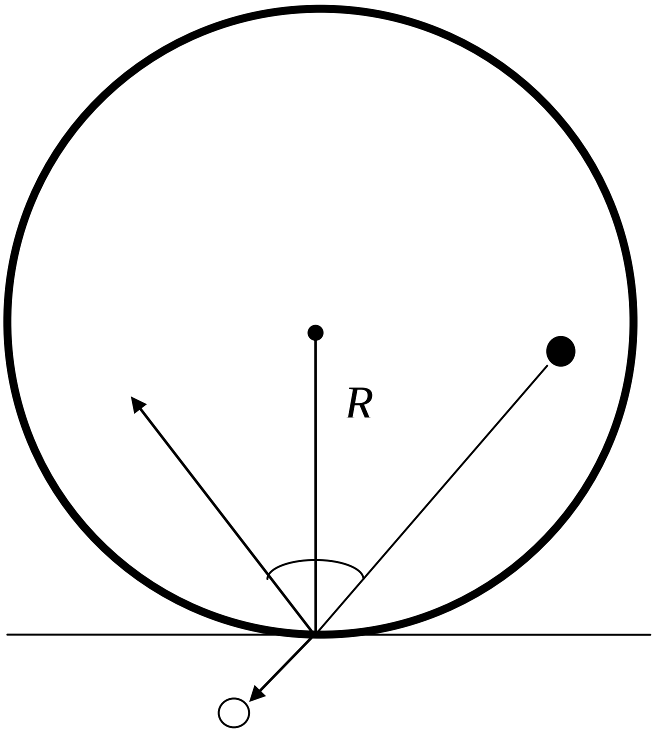

Figure 5.1. Elastically reflecting boundary. A particle (full blob) is reflected from the wall at the same angle as that between the incident velocity and normal to the wall. Light blob is a supposed position of the blob in the absence of reflection.

If N_x is the number of atoms along one side of a regular hexagon, then the total number of atoms N is given by

$$N = 3N_x^2 - 3N_x + 1 \tag{5.5}$$

Taking N_x = 8, 16, 30 and 70, for example, yields hexagons containing 169, 721, 2611 and

14 491 atoms, respectively, Fig. 5.2. These sizes were simulated by Blink and Hoover (Blink and Hoover 1985) and so for purpose of validation of our codes, we have also generated lattices with this number of atoms.

The bounding circle has a radius given by $\sqrt{\frac{N}{4\pi}}$ (assuming unit spacing between atoms). The aim is to produce a droplet with a given density. Its radius is $\sqrt{\frac{N}{\pi\rho}}$ hence it is necessary to adjust the spacing accordingly. Once the hexagon is created, particles were given velocities with zero mean, sampled from a Maxwell-Boltzmann distribution. Constant temperature MD was then performed using either of the two confining schemes (elastic boundary conditions and repulsive potential) until the crystal melted and a uniform droplet was obtained, Fig. 5.2. So, the system was equilibrated to the desired density and temperature within the confining circle. The equilibration lasted 100 000 steps with the step size 0.001. A plateau in the dependence of a physical value on the step number indicated equilibrium was achieved, for example, Fig. 5.3 illustrates how the pressure in the droplet varies with the number of steps.

The pressure in this method at the first stage was calculated by the same virial formula as in the Holian-Grady method, Eq. (4.6), although it may not be strictly applied because of the absence of periodic boundary conditions. Nevertheless, it produced reasonable results. These results appear in Table 5.1 along with those of (Blink and Hoover 1985) for comparison. Neither method is correct but they are reasonable. The agreement is not perfect because of the problems previously discussed (referring to calculating pressure in a non-periodic box) and because Blink and Hoover used an equation of state to estimate their initial pressure. Their pressures are not simulated values but calculated from the Henderson equation of state (Henderson 1977). Hoover and Blink used an equation of state developed from limited results obtained by Henderson for the cut Lennard-Jones potential. Because equations of state have improved since Hoover’s paper, we decided to use a more up to date one, namely, the Reddy-O’Shea equation of state (Reddy and O’Shea 1986).

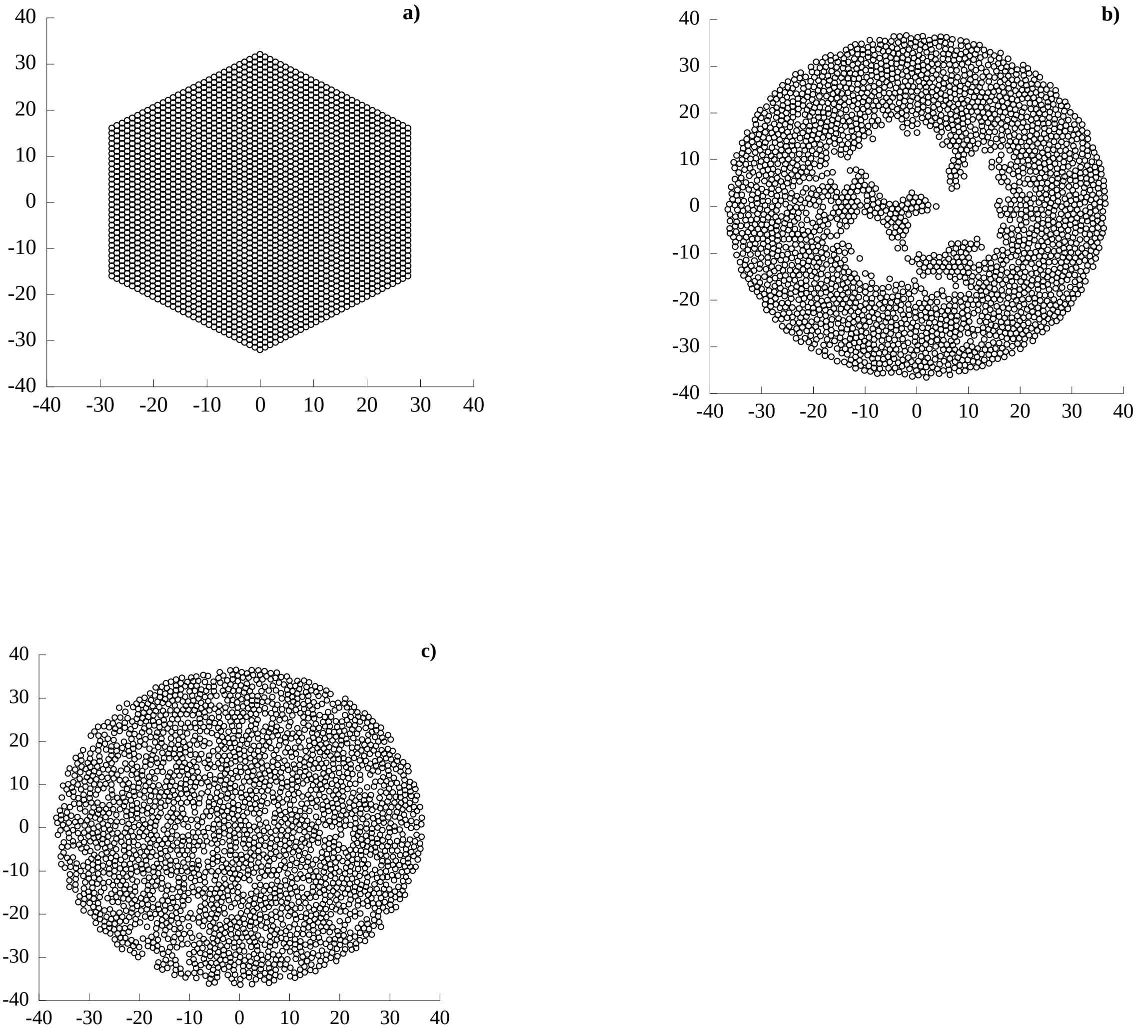

Figure 5.2. Snapshot of the particle positions during and after the equilibration in our MD simulation by the Blink-Hoover method. $N = 2611$, $\rho = 0.62$, $T = 0.76$. a) The initial system configuration, b) After 15 000 steps, c) After 100 000 steps.

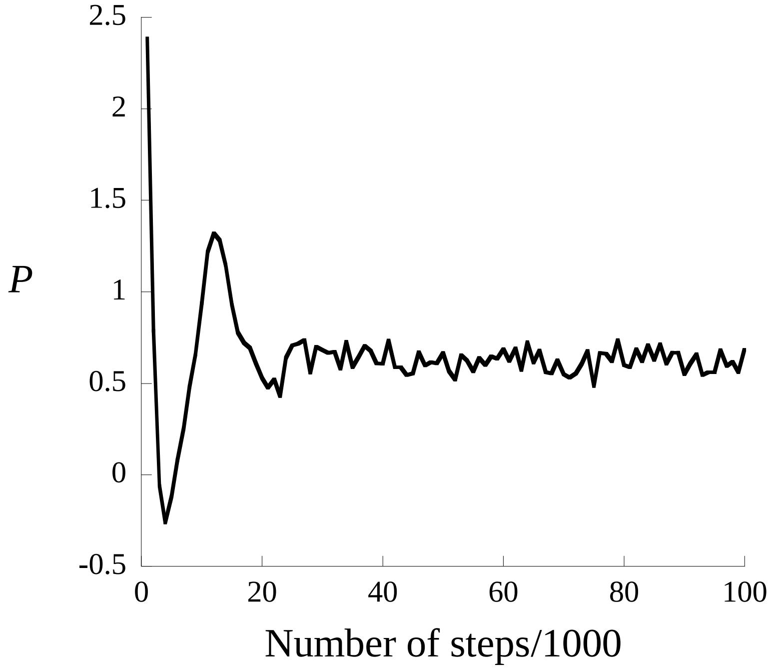

Figure 5.3. Dependence of the pressure in a spherical droplet with elastic wall on the number of steps. $N = 2611$, $\rho = 0.62$, $T = 0.76$.

An alternative to using the virial is to compute the force at the walls in the confining potential case. Our results are given in Table 5.2. There is a good agreement between virial and wall pressure. It can also be done with elastic boundary conditions, this is more effortful but it produces the best results and is used by us. The steep repulsive potential produces unphysical cavitation. Another alternative would be to use the method of planes (Todd et al 1995) adapted for circular symmetry, but again that involves tedious coding.

Table 5.1. The dimensionless values of pressure *P*, obtained in (Blink and Hoover 1985) and in this work by the Blink-Hoover method for LJ potential with R_{cut} = 2.5. In this work 100 000 equilibration steps were used and step size 0.001.

T	***ρ***	***P***	
		(Blink, Hoover 1985)	**This work**
1.01	0.61	1.02[a]	1.086(7)[a]
1.16	0.62	1.38	1.46(3)
0.76	0.62	0.53	0.66(3)
0.65	0.62	0.31	0.394(2)

Superscript a means obtained in simulations with 14491 particles. Other results are for *N* = 2611. In brackets, standard error.

The availability of an equation of state has many advantages, particularly in relation to studying fragmentation since the whole of thermodynamics is unlocked. One can easily compute internal energy, heat capacity, sound speed and in principle determine the phase diagram (see later). Reddy and O'Shea derived their equation of state for the two-dimensional Lennard-Jones fluid following the approach of (Nicolas *et al* 1979) for the three-dimensional fluid. They obtained a modified Benedict-Webb-Rubin equation (Reid *et al* 1977) by fitting the energy, pressure, and second virial coefficients, as Nicolas *et al* did, but they also fitted the third virial coefficients. They supplemented that with Monte Carlo data from their simulations and that resulted in a big improvement. The authors used Lennard-Jones reduced units.

Table 5.2. Pressure, *P*, obtained in this work by the Blink-Hoover method for LJ potential with R_{cut} = 2.5 by the virial method, and by Eq. (5.4). The number of equilibration steps: 100 000, and step size: 0.001.

T	**ρ**	**P**			
		Virial method	**$\sigma = 0.8$, $\varepsilon = 10$**	**$\sigma = 1.0$, $\varepsilon = 10$**	**$\sigma = 1.0$, $\varepsilon = 100$**
1.01	0.61	1.086(7)[a]	1.19(5)[a]	1.21(6)[a]	1.21(5)[a]
1.16	0.62	1.432(2)	1.55(2)	1.46(2)	1.61(2)
0.76	0.62	0.66(3)	0.71(3)	0.72(3)	0.74(3)
0.65	0.62	0.394(2)	0.48(4)	0.49(3)	0.50(3)

Superscript a means obtained in simulations with 14 491 particles. Other results are for $N = 2611$. In brackets, standard error. The values σ and ε are parameters of Eq. (5.2). Data for virial method are for $\sigma = 0.8$, $\varepsilon = 10$.

The Reddy-O'Shea equation is:

$$P = \rho T + \rho^2[c_1T + c_2T^{1/2} + c_3 + c_4T^{-1} + c_5T^{-2}] + \rho^3[c_6T + c_7 + c_8T^{-1} + c_9T^{-2}] +$$

$$\rho^3[c_{20}T^{-2} + c_{21}T^{-3}]\exp(-\gamma\rho^2) + \rho^4[c_{10}\mathrm{T} + c_{11} + c_{12}T^{-1}] + \rho^5 c_{13} +$$

$$\rho^5[c_{22}T^{-2} + c_{23}T^{-4}]\exp(-\gamma\rho^2) + \rho^6[c_{14}T^{-1} + c_{15}T^{-2}] + \rho^7 c_{16}T^{-1} +$$

$$\rho^7[c_{24}T^{-2} + c_{25}T^{-3}]\exp(-\gamma\rho^2) + \rho^8[c_{17}T^{-1} + c_{18}T^{-2}] + \rho^9 c_{19}T^{-2} +$$

$$\rho^9[c_{26}T^{-2} + c_{27}T^{-4}]\exp(-\gamma\rho^2) + \rho^{11}[c_{28}T^{-2} + c_{29}T^{-3}]\exp(-\gamma\rho^2) +$$

$$\rho^{13}[c_{30}T^{-2} + c_{31}T^{-3} + c_{32}T^{-4}]\exp(-\gamma\rho^2) \qquad (5.6)$$

The parameters C_n and γ of this equation are given in Table A1 in Appendix 2.

The internal energy may be obtained from the thermodynamic relationship:

$$U = \int_0^{\rho} \frac{1}{\rho^2}\left[P - T\frac{\partial P}{\partial T}\right]\mathrm{d}\rho \tag{5.7}$$

From which, the isochoric heat capacity may be obtained from (5.7) via

$$C_V = \left(\frac{\partial U}{\partial T}\right)_V \tag{5.8}$$

In fragmentation science, the speed of sound is very important because it is the speed by which information is transferred between particles. The fragmentation (or expansion) of an object needs to occur for several sound traversal times because we consider practically instant fragmentation in our work, not a long-term one. One can derive the speed of sound thermodynamically, and the expression is:

$$c^2 = \left(\frac{\partial P}{\partial \rho}\right)_T + \frac{T}{C_V \rho^2}\left(\frac{\partial P}{\partial T}\right)_{\rho}^2 \tag{5.9}$$

(ρ is the mass density and the dimension of the left and right parts of Eq. (5.9) is m^2/s^2.) This derivation is given in Appendix 3. Finally, we obtain the speed of sound by introducing this heat capacity and pressure from Eq. (5.6) into Eq. (5.9). Toxvaerd quotes the formula in his paper (Toxvaerd 1981). Note the different power on the second term on the right hand side. His equation is in error – a fact acknowledged by him to us in a private communication to K. Travis (Travis 2009).

Tables 5.3 and 5.4 show a range of pressures, internal energies, heat capacities and sound speeds computed using the Reddy-O'Shea equation of state: Eq. (5.6). Also included are results from periodic two-dimensional Monte Carlo simulations (our work). Sound speeds obtained by Blink and Hoover are included as well. One can see that there is a good agreement between the values except for C_V and c at $T = 0.55$ and 0.51. The heat capacity was calculated in MC by the formula $C_V = \frac{\langle U^2\rangle - \langle U\rangle^2}{kT^2}$. A possible reason could be that a 721 particle system is not big enough. In the Monte Carlo method we used a cut off potential and applied long range correction for the pressure and internal energy in two dimensions:

$$U_{LR} = 2\pi N\rho \int_{R_{\mathrm{cut}}}^{\infty} r^2 U(r)\mathrm{d}r \tag{5.10}$$

$$P_{LR} = -\frac{2\pi N\rho}{3V} \int_{R_{\mathrm{cut}}}^{\infty} r^2 w(r)\mathrm{d}r \tag{5.11}$$

(Allen and Tildesley 1987). We assumed the radial distribution function $g(r)$ tends to unity after R_{cut}. Here $w(r)$ is the intermolecular pair virial function

$$w(r) = r\frac{\mathrm{d}U(r)}{\mathrm{d}r} \tag{5.12}$$

For the Lennard-Jones potential these equations become

$$U_{LR} = \frac{2}{5}\pi N\rho R_{\mathrm{cut}}^{-10} - \pi N\rho R_{\mathrm{cut}}^{-4} \tag{5.13}$$

$$P_{LR} = \frac{12}{5}\pi\rho^2 R_{\mathrm{cut}}^{-10} - 3\pi\rho^2 R_{\mathrm{cut}}^{-4} \tag{5.14}$$

Table 5.3. The dimensionless values of the pressure *P* and internal energy *U*, obtained in this work using the Reddy-O'Shea equation of state, Eq. (5.6), and Monte Carlo simulations.

T	ρ	*P*		*U*	
		Reddy EoS	**Monte Carlo**	**From Reddy EoS**	**Monte Carlo**
1.01	0.61	0.99	0.98(8)	–1.659	–1.666(2)
1.16	0.62	1.36	1.354(3)	–1.642	–1.649(4)
0.76	0.62	0.51	0.51(2)	–1.779	–1.785(3)
0.65	0.62	0.28	0.28(2)	–1.835	–1.839(7)
1.17	0.61	1.31	1.31(1)	−1.611	−1.618(1)
0.77	0.63	0.56	0.56(2)	−1.803	–1.811(3)
0.65	0.65	0.35	0.35(1)	−1.918	–1.925(2)
0.55	0.66	0.13	0.12(1)	−2.013	–2.012(3)
0.51	0.68	0.07	0.06(2)	−2.102	–2.096(4)

In brackets, standard error.

Table 5.4. The dimensionless values of the isochoric heat capacity C_V and speed of sound *c* obtained in this work using the Reddy-O'Shea equation of state (5.6) and Monte Carlo simulations, and in (Blink and Hoover 1985).

T	***ρ***	***C_V***		***c***	
		From Reddy EoS	**Monte Carlo**	**(Blink, Hoover 1985)**	**From Reddy EoS**
1.01	0.61	1.32	1.32	3.7	3.73
1.16	0.62	1.30	1.29	4.1	4.20
0.76	0.62	1.44	1.43	3.1	3.05
0.65	0.62	1.61	1.58	2.7	2.50
1.17	0.61	1.29	1.29	4.0	4.1
0.77	0.63	1.42	1.42	3.2	3.2
0.65	0.65	1.55	1.51	3.2	2.95
0.55	0.66	1.82	1.70	2.9	2.41
0.51	0.68	1.95	1.79	2.9	2.42

In brackets, standard error.

5.3 Fragmentation results

We conducted a series of expansion runs using the same conditions as used in Hoover-Blink. Expansion begins with removal of the confining boundary. The thermostat is switched off and the expansion occurs adiabatically. The simulations used a 4th order Runge-Kutta integrator with Δt = 0.001. Blink and Hoover ran their simulations at multiples of the sound traversal time, R/c, where R is the radius of boundary circle, and c is the sound speed. If density $\rho = N/V$, V is πR^2 then

$R = \sqrt{\frac{N}{\pi\rho}}$. For example, for N = 2611, ρ = 0.62 and T = 1.16, R = 36.6. Now if the expansion time equals $4.2R/c$ and Δt = 0.001 the simulation is stopped after 37510 steps (Blink and Hoover found that for these values of N, ρ and T the expansion lasts $4.2R/c$).

Clusters were evaluated as in the previous Holian-Grady work except a cluster bond length of r_0 = 2.5 was used to define a cluster in keeping with the definition employed by Blink and Hoover. We calculated the number of monomers, N_m, cluster size, N_c, defined as the maximum cluster size and the ratio $N_c/(N - N_m)$ etc. The results produced with 10 realisations are in Table 5.5 together with the values of Blink and Hoover. The agreement is good.

We have plotted snapshots of the particle positions in the course of the fragmentation; such a sequence is shown in Fig. 5.4. They resemble well the corresponding plots in (Blink and Hoover 1985) done for 14 491 particles. Once can see that the main body of the system expands slowly and in it, crushing of the fragments occurs. The number of monomers is small. Significant expansion is due to a small portion of the particles. The largest cluster decreases from 2580 at reduced time t = 0.1 to 2044 at t = 0.5, then it quickly diminishes to 171 at t = 1.0. One can see that the fragmentation mechanism is hydrodynamic fracture (usual mechanical fracture) because regular patterns which occur in spinodal decomposition cannot be observed. This is because the expansion is non-homogeneous, spinodal decomposition occurs only in homogeneous systems.

Table 5.5. **Initial conditions and results from the two-dimensional MD simulations by Blink and Hoover (1985), and from this work using the method of Blink and Hoover. The system population N, temperature T and density ρ are given. N_c is the biggest cluster population, N_m is the number of monomers.**

N	T	ρ	P	N_c		N_m		$N_c/(N-N_m)$	
			Reddy EoS	**(Blink, Hoover 1985)**	**This work**	**(Blink, Hoover 1985)**	**This work**	**(Blink, Hoover 1985)**	**This work**
14491	1.01	0.61	0.99	375	369(12)	1183	1088(24)	0.028	0.028
2611	1.16	0.62	1.36	136	171(9)	200	196(14)	0.056	0.071
2611	0.76	0.62	0.51	270	236(8)	218	231(13)	0.11	0.10
2611	0.65	0.62	0.28	361	646(7)	170	152(14)	0.15	0.26
721	1.17	0.61	1.31	44	67(6)	82	80(6)	0.069	0.10
721	0.77	0.63	0.56	117	149(5)	85	94(6)	0.18	0.24
721	0.65	0.65	0.35	337	338(4)	66	64(7)	0.515	0.514
721	0.55	0.66	0.13	593	628(3)	64	44(3)	0.90	0.93
721	0.51	0.68	0.07	626	645(4)	53	43(5)	0.94	0.95

Blink and Hoover do not give errors. Standard error is given in brackets.

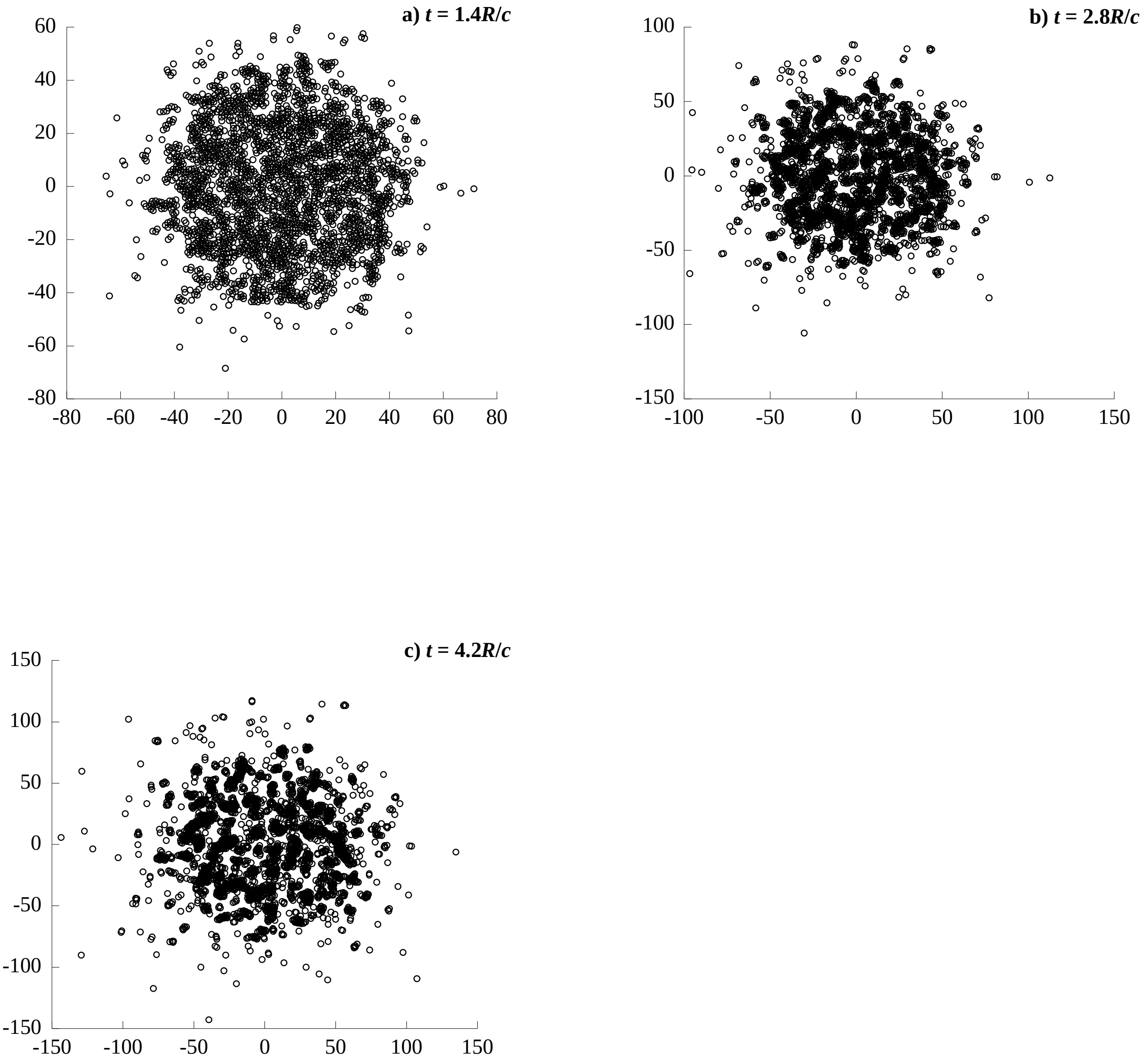

Figure 5.4. Snapshot of the particle configuration in our simulation by the Blink-Hoover method at a) $t = 1.4R/c$, b) $t = 2.8R/c$, and c) $t = 4.2R/c$. $N = 2611$. Initial state points $\rho_0 = 0.62$ and $T_0 = 1.16$.

5.4 System Size Dependence and Scaling Law

5.4.1 Dependence of the largest fragment size, *N*c, on the system size, *N*

The largest fragment size depends on the initial pressure in the system, and on the system size. Existing four fragmentation models predict different dependencies. It is necessary to compare the results of our simulations with those models. The first two models are very simple and given in (Blink and Hoover 1985). The third and the fourth models are developed by Grady (Grady 1982) and extended by Blink, Glenn and Hoover (Blink and Hoover 1985). They predict dependence of the fragment maximum size on the initial pressure and the number of particles in the system; model 1: $N_c \sim N^0P^{-D}$, model 2: $N_c \sim N^0P^{-2D}$, model 3: $N_c \sim N^{2/3}P^{-2D/3}$, and model 4: $N_c \sim NP^{-D}$, where D is the dimensionality. This dependence is summarised in Table 5.6.

Table 5.6. Dependence of the largest fragment size in the Blink-Hoover method on the number of particles, *N*, and the initial pressure, *P* for the 2-dimensional fluid.

Model	Dependence on the number of particles	Dependence on the pressure
1, (Blink and Hoover 1985)	N^0	P^{-2}
2, (Blink and Hoover 1985)	N^0	P^{-4}
3, (Grady 1982, Blink and Hoover 1985)	$N^{-2/3}$	$P^{-4/3}$
4 (Grady 1982, Blink and Hoover 1985)	N	P^{-2}

In the model 1, the initial pressure balances the surface tension. Model 2 is more realistic, it accounts for expansion pressure instead of static one. Description of model 3 was given in §4.10, it minimises the sum of the kinetic energy of expanding fragments per unit mass and the surface energy per unit mass. Model 4 is model 3 which takes only the dilational energy of fragments in an outer shell and does not account for the energy of the core.

Blink and Hoover (Blink and Hoover 1985) investigated the dependence of the largest fragment size on the system size for the systems with 169, 721, 2611 and 14 491 atoms. We performed simulations with larger systems, even with 202 021 and 500 617 atoms. Their systems had different pressures and temperatures and they adjusted their data to uniform starting conditions. We performed this investigation for many more systems, from 169 to 202 021 particles with 10 realisations, and for 500 617 particles with 7 realisations, and with *uniform* initial conditions ρ = 0.62, T = 1.16, and, therefore, our results should be more reliable. Our results are given in Table 5.7 and plotted in Fig. 5.5 as logN_c versus log$N$. Our results produce the slope 0.33 and the work of Blink and Hoover gives the value ≈ 0.7. The slope 0.33 agrees with neither of 4 above mentioned models, it is in the middle between the model 3 and models 1 and 2.

Table 5.7. Dependence of the largest cluster size, N_c, on the system size in the Hoover-Blink method, ρ = 0.62, T = 1.16.

N	P	N_c
169	1.36(1)	60.8(17.5)
721	1.41(1)	124(27.9)
2611	1.43(3)	169(29)
4219	1.437(2)	180(22.4)
14491	1.445(3)	295(58.8)
101017	1.48(4)	550(167)
202021	1.46(3)	738(116)
500617[a]	1.39(4)	897(107)

In brackets, standard error in pressure and standard deviation for N_c. [a]Obtained with 7 realisations.

In Table 5.8 and Fig. 5.6 the same dependence is given obtained with 10 realisations but for another state of the system: $\rho = 0.65$ and $T = 0.65$. The slope is equal to 0.63(1). This is close to the model 3.

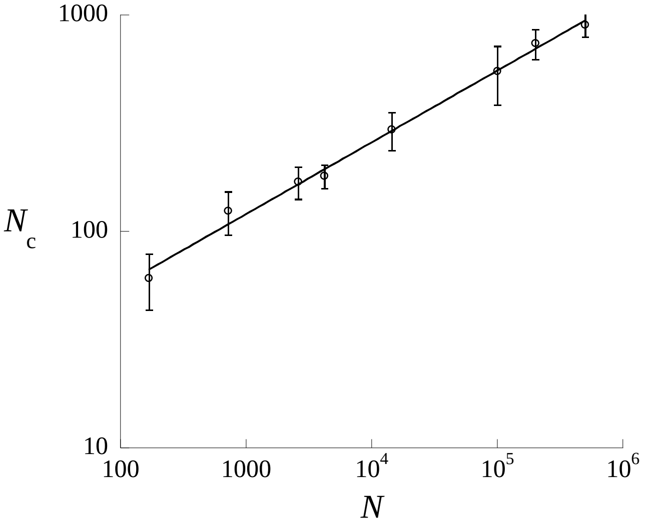

Figure 5.5. Dependence of the largest fragment, N_c, on the system size, N, Table 5.7. Parameters of the system are $\rho = 0.62$ and $T = 1.16$. Slope equals 0.33(1).

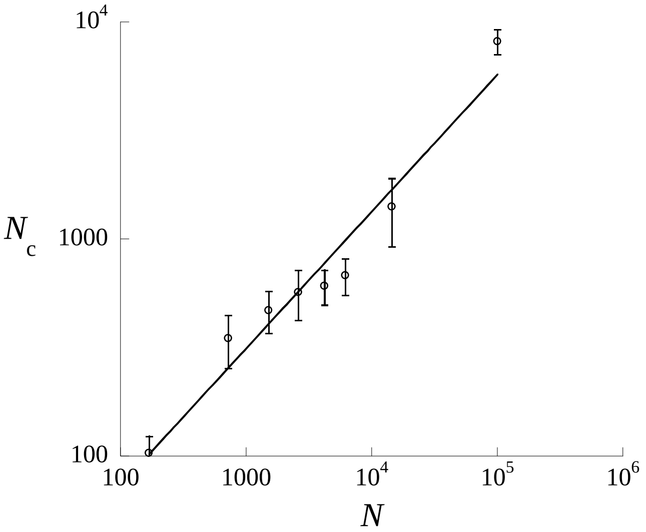

Figure 5.6. Dependence of the largest fragment, N_c, on the system size, N, Table 5.8. Parameters of the system are $\rho = 0.65$ and $T = 0.65$. Slope equals 0.63(1). The points from 2nd till 5th from the left have a slope 0.30(0.4).

Table 5.8. Dependence of the largest cluster size N_c on the system size in the Hoover-Blink method but for ρ = 0.65 and T = 0.65.

N	P	N_c
169	0.458(2)	103(20)
721	0.492(3)	348(95)
1519	0.489(3)	469(102)
2611	0.483(3)	568(148)
4219	0.475(1)	606(110)
6211	0.474(2)	679(130)
14491	0.480(3)	1407(489)
101017	0.54(5)	8131(1060)

In brackets, standard error in pressure and standard deviation for N_c.

5.4.2 Dependence on the initial pressure P_0

To test the fragmentation models, we examined the dependence of the largest fragment size on the pressure for systems with different sizes and pressures. For N = 2611, our result is given in Table 5.9 for 10 realisations. Again, 100 000 equilibration steps were used. Step size is 0.001.The slope obtained from the plot is –1.76(1) for all points, Fig. 5.7, (Hoover had –1.3 for only two points).

Table 5.9. Dependence of the largest fragment size N_c on the pressure in the simulation with the Blink-Hoover method for N = 2611 and ρ = 0.62.

T	P	N_c
1.16	1.43(3)	171(29)
1.0	1.14(3)	105(27)
0.90	0.94(3)	150(38)
0.76	0.74(3)	291(86)
0.65	0.50(3)	703(237)
0.55	0.26(3)	2155(333)

In brackets, standard error for P and standard deviation for N_c.

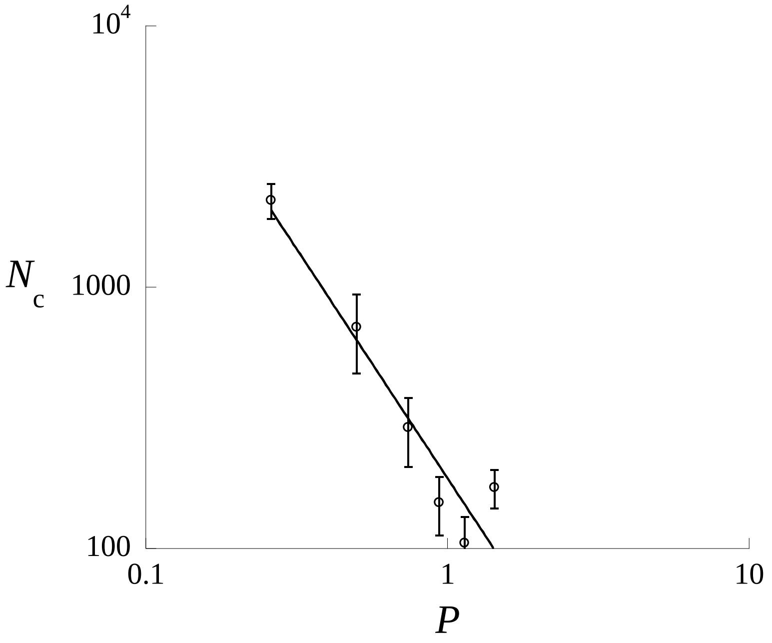

Figure 5.7. Dependence of the largest fragment, N_c, on the pressure, P, Table 5.9. Parameters of the system are N = 2611 and ρ = 0.62. Slope equals –1.76(1), the fit is not weighted.

In Table 5.10, the same dependence is presented but for $N = 4219$ and also for 10 realisations. The slope equals –1.53(1), Fig. 5.8.

Table 5.10. Dependence of the largest fragment size, N_c, on the pressure in the simulation with the Blink-Hoover method for $N = 4219$ and $\rho = 0.62$.

T	***P***	***N_c***
1.16	1.437(2)	180(22)
1.0	1.15(4)	292(58)
0.90	0.96(5)	211(42)
0.76	0.61(0)	313(49)
0.65	0.39(0)	727(262)
0.55	0.28(3)	3245(678)

100 000 equilibration steps were used. Step size is 0.001. In brackets, standard error for P and standard deviation for N_c.

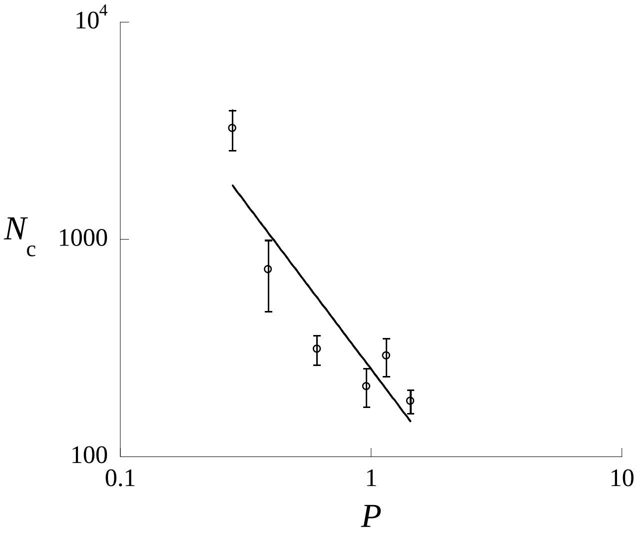

Figure 5.8. Dependence of the largest fragment, N_c, on the pressure, P, Table 5.10. Parameters of the system are $N = 4219$ and $\rho = 0.62$. Slope equals –1.53(1), not weighted fit.

In Table 5.11 our results are given for N = 14 491 and a constant density 0.61 for 10 realisations. The slope in this case is –1.31(1), Fig. 5.9. One can observe that the slope decreases with the number of particles and tends to –1.3 predicted by the model 3 (simulations for larger sizes are necessary, of course). Another important result is obtained – generally, the higher is the pressure, the smaller are the largest fragment sizes.

Table 5.11. Dependence of the largest fragment size, N_c, on the pressure in the simulation with the Blink-Hoover method for N = 14 491 and ρ = 0.61.

T	P	N_c
1.16	1.46(4)	270(70)
1.06	1.176(1)	273(64)
1.01	1.09(1)	369(120)
0.96	0.974(1)	381(74)
0.86	0.773(1)	403(101)
0.76	0.573(1)	596(172)
0.66	0.376(1)	1732(248)

100 000 equilibration steps were used. In brackets, standard error for P and standard deviation for N_c.

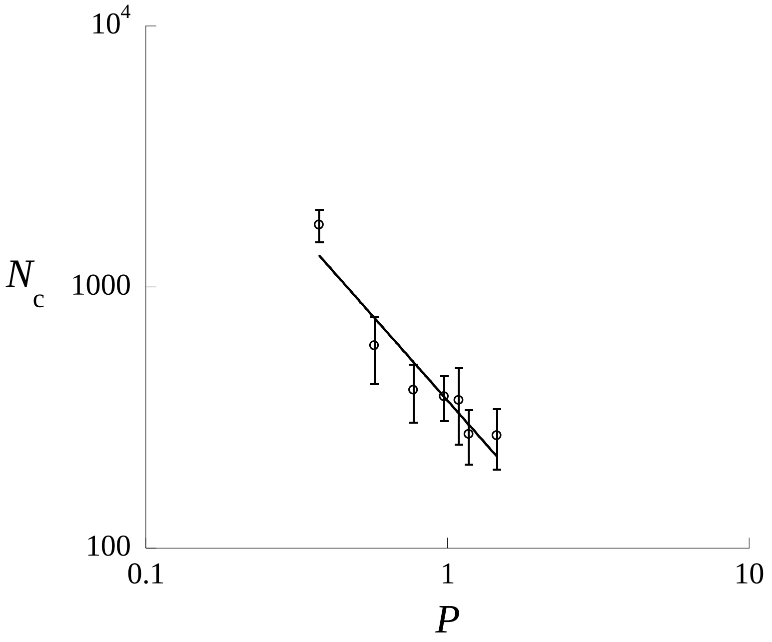

Figure 5.9. Dependence of the largest fragment, N_c, on the pressure, P, Table 5.11. Parameters of the system are $N = 14491$ and $\rho = 0.61$. Slope equals –1.31(1), not weighted fit.

5.5 Simulations with the Blink-Hoover method with the LJ-spline potential

We did simulations with the Blink-Hoover method but with the same potential as used by Holian and Grady – i.e. spline-aproximated Lennard-Jones potential, for a state point in common with Blink and Hoover. The system size was $N = 2611$, and the number of steps used for equilibration was 100 000, with the step size 0.001. The cluster bond length, r_0, was 2.5. The idea was to perform the simulations in the same circular system and with the same parameters but with a different potential and to compare the computed thermodynamic parameters of the system and properties of the fragments. The results of the simulations and the cluster statistics are given in Tables 5.12 − 5.14. The pressure obtained by this method differs not much from that of the traditional Blink-Hoover routine in our simulations, however, it is always a little higher. The potential energy with the LJ-spline potential is noticeably higher what should be expected. Increase in the potential energy leads to increase of the pressure, that should be expected. The final thermal temperatures of the fragments agree very well with each other except for $\rho = 0.68$. The biggest cluster size for the

LJ-spline potential usually is smaller than for the traditional case. For the points with $\rho = 0.62$ in Table 5.13, the dependence $\log N_c - \log P$ has the slope –2.5. In Table 5.14 additional simulations are given, and for them the slope is –2.1. This is close to the models 1 and 4.

Table 5.12. Simulations with the Blink - Hoover method, and with the Blink - Hoover method with the LJ-spline potential done in this work, *N* = 2611 (the same circular system but different potentials). Equilibrium values of pressure *P* and internal energy *U*.

T	***ρ***	***P***		***U***	
		LJ cut	**LJ-spline**	**LJ cut**	**LJ-spline**
1.16	0.62	1.46(3)	1.50(2)	–1.608(49)	–1.399(49)
0.76	0.62	0.66(3)	0.70(3)	–1.797(72)	–1.592(70)
0.65	0.62	0.394(2)	0.48(3)	–1.869(75)	–1.672(74)
1.17	0.61	1.41(2)	1.45(2)	–1.581(49)	–1.370(49)
0.51	0.68	0.32(6)	0.34(6)	–2.149(76)	–1.923(68)

Standard deviation is given in brackets.

Table 5.13. Simulations with the Blink - Hoover method, and with the Blink - Hoover method with the LJ-spline potential done in this work, $N = 2611$. Non-equilibrium value of the final thermal temperature of particles after the expansion, T_{final}, and the largest cluster population, N_{c}.

T	ρ	T_{final}		N_{c}	
		LJ cut	**LJ-spline**	**LJ cut**	**LJ-spline**
1.16	0.62	0.22(1)	0.21(1)	171(29)	117(26)
0.76	0.62	0.19(1)	0.19(1)	236(71)	157(32)
0.65	0.62	0.18(2)	0.19(3)	646(118)	1821(385)
1.17	0.61	0.19(1)	0.19(1)	113(27)	76(16)
0.51	0.68	0.12(2)	0.19(1)	2296(204)	295(61)

Standard deviation is given in brackets.

Table 5.14. Simulations with the Blink - Hoover method with the LJ-spline potential done in this work, $N = 2611$. Dependence of the largest cluster population, N_{c}, on the pressure.

T	ρ	P	N_{c}
1.16	0.62	1.50(2)	117(26)
1.0	0.62	1.18(2)	165(40)
0.90	0.62	0.98(2)	119(19)
0.76	0.62	0.70(3)	157(32)
0.65	0.62	0.48(3)	1821(385)
0.55	0.62	0.29(3)	2425(39)

5.6 Properties of Fragments

It is interesting to know what is the effect of system size on the fragment population and on the size of the largest fragment, their translational, thermal and rotational temperature, gyration radius and shape factor. We calculate these values obtained with 10 realizations. In Figs. 5.10 and 5.11 that dependence is plotted for the systems of 14 491, 101017, 202021 and 500 617 particles (in the latter case 7 realisations were done). The initial density and temperature are ρ = 0.62 and T = 1.16, respectively.

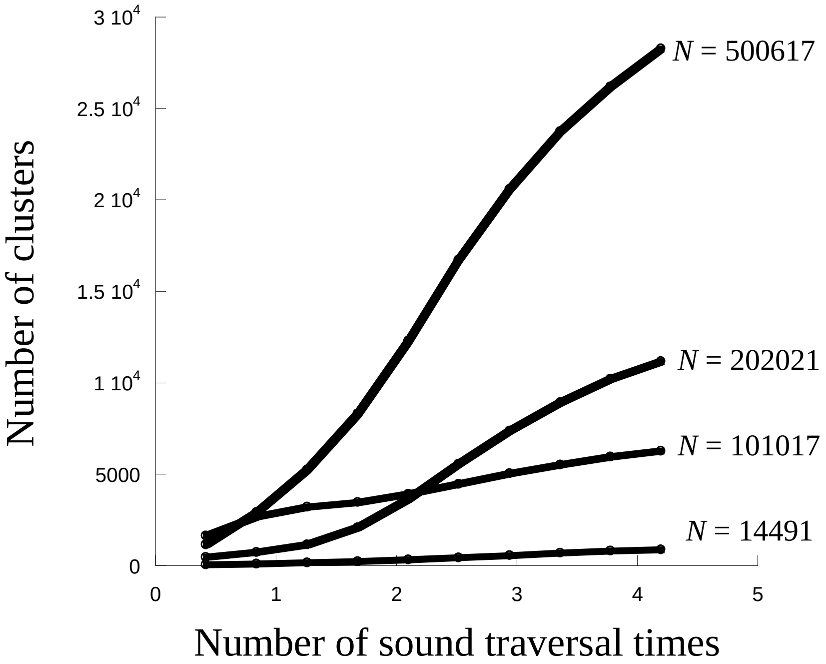

Figure 5.10. Dependence of the number of fragments on the time during Blink-Hoover expansion for 14 491, 101 017, 202 021 and 500 617 particles. Initial density and temperature are 0.62 and 1.16, respectively.

One can notice an interesting result in Fig. 5.10: the number of clusters does not depend strongly on the system size at the beginning of the expansion for all systems, then till the half of the expansion time this dependence is not strong for $N \leq 202021$. At the end of the expansion, the number of fragments is proportional to the system size. In Fig. 5.11 one can see that until N = 202 021 the largest fragment size is proportional to the system size during the first half of the expansion, and then it decreases drastically. For N = 500 617 the largest fragment size decreases faster with the expansion.

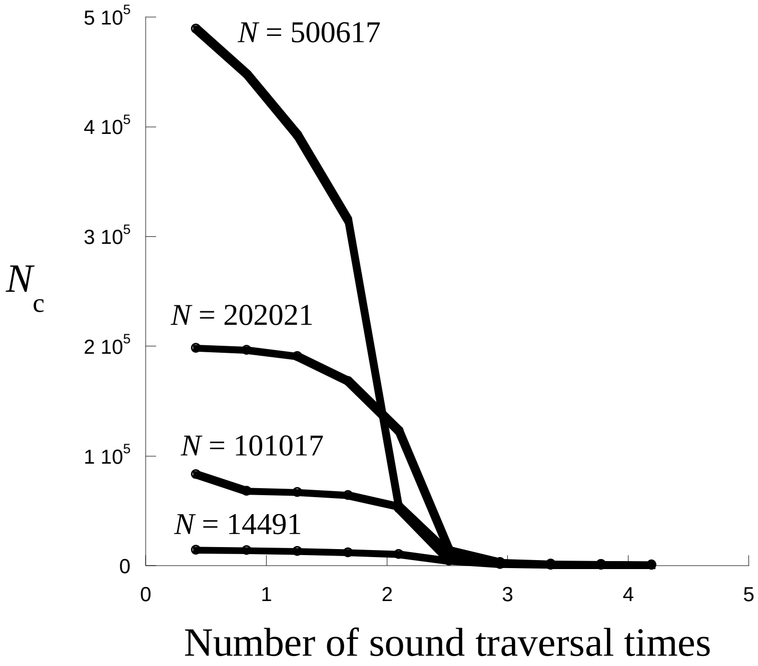

Figure 5.11. Dependence of the largest fragment size on the time during Blink-Hoover expansion for 14 491, 101 017, 202 021 and 500 617 particles. Initial density and temperature are 0.62 and 1.16, respectively.

In Fig. 5.12 the translational temperature of clusters is given for the systems with 14 491, 101 017, 202 021 and 500 617 particles and the initial density and temperature ρ = 0.62 and T = 1.16, respectively. It decreases with the expansion and increases with N, as in Blink and Hoover (1985). In Fig. 5.13 the translational temperature of the largest cluster is presented. It increases with the expansion and practically does not depend on the system size during the fragmentation run. The latter reaches the value ≈0.4 (same as thermal temperature) at the end of the expansion, the same one as that of Blink and Hoover (1985) for much smaller systems and it does not depend on the size for N = 100 – 500 thousands. However, For N = 14 491 this temperature is about 0.25. Also, the final temperature is reached after 4 sound traversal times and not after 3 as by Blink and Hoover.

Blink and Hoover found an increase with the size of this temperature in agreement with model 3, our data confirm that, but at *N* about 100 000 the saturation exists.

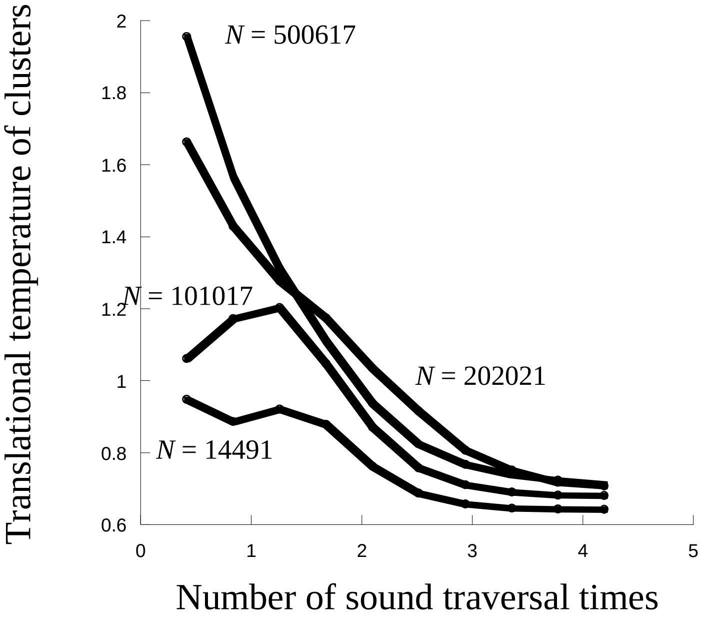

Figure 5.12. Translational temperature of fragments versus expansion time during Blink-Hoover expansion for 14 491, 101 017, 202 021 and 500 617 particles. Initial density and temperature are 0.62 and 1.16, respectively.

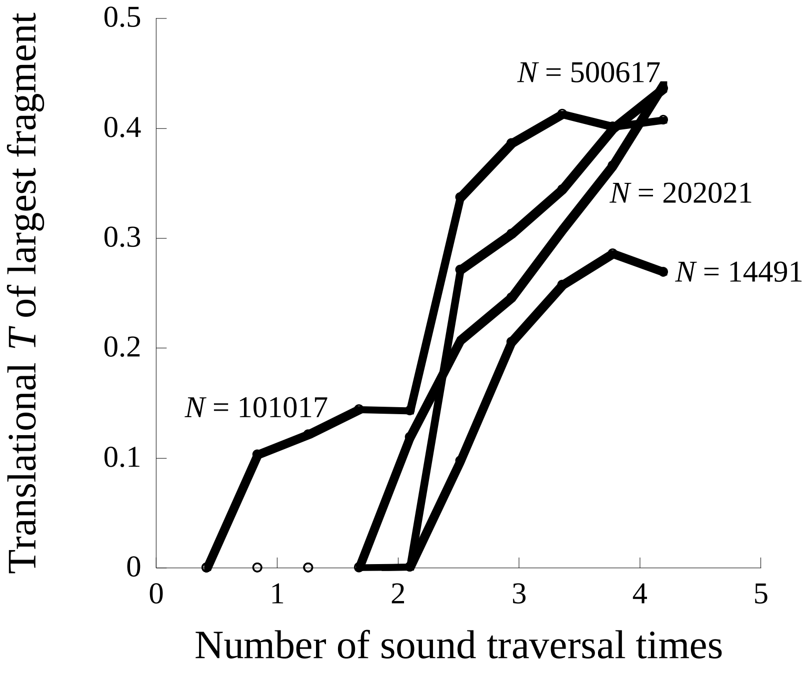

Figure 5.13. Translational temperature of the largest fragment versus expansion time during Blink-Hoover expansion for 14 491, 101 017, 202 021 and 500 617 particles. Initial density and temperature are 0.62 and 1.16, respectively.

In Fig. 5.14 the thermal temperature of clusters is given for the systems with N = 14 491, 101 017, 202 021 and 500 617 particles, and the initial density and temperature $\rho = 0.62$ and $T = 1.16$, respectively. In Fig. 5.15 the thermal temperature of the largest fragment is presented. It decreases with the expansion steadily. Behaviour of the temperature of all fragments is more complicated. One can notice an interesting result: the latter value for N = 101 017 differs noticeably from that for other sizes. For other system sizes it is practically the same. The temperature of the largest fragment practically does not depend on the system size. The final thermal temperature of the largest fragment is about 0.4 and it reaches this value after 3 − 4 sound traversal times, both in agreement with Blink and Hoover (1985). The parameters of the largest fragment are of particular importance to us because Grady’s model in the Blink-Hoover expansion predicts only the size of the largest fragment. In general, the thermal temperatures of all fragments are similar, in agreement with Blink and Hoover (1985) and Vicentini et al (1985). Their final value obtained by us is about 0.22. The monomer temperature is always higher than the fragment temperature in the papers of these authors and in our case. Also, the sum of the final thermal and translational temperatures in their case and our case is always less than the initial temperature of the system.

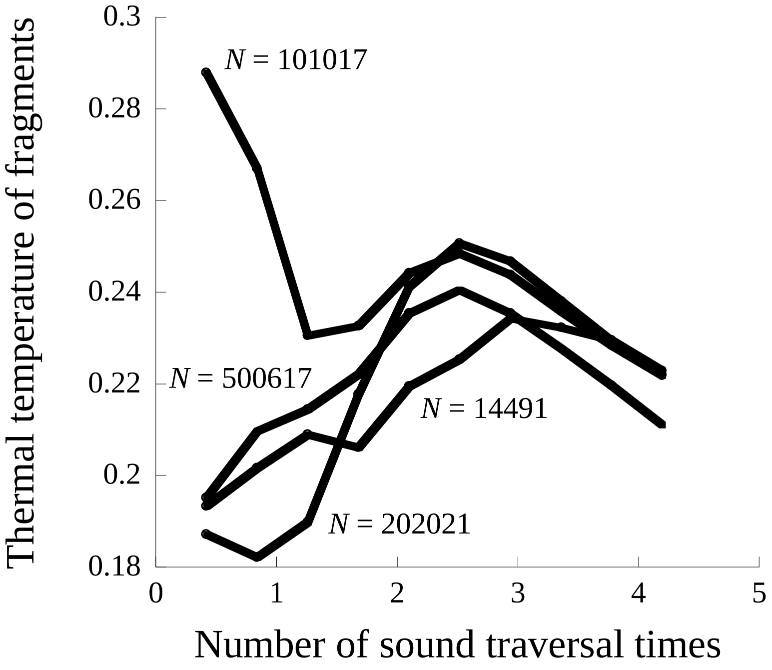

Figure 5.14. Thermal temperature of the fragments versus expansion time during Blink-Hoover expansion for 14 491, 101 017, 202 021 and 500 617 particles. Initial density and temperature are 0.62 and 1.16, respectively.

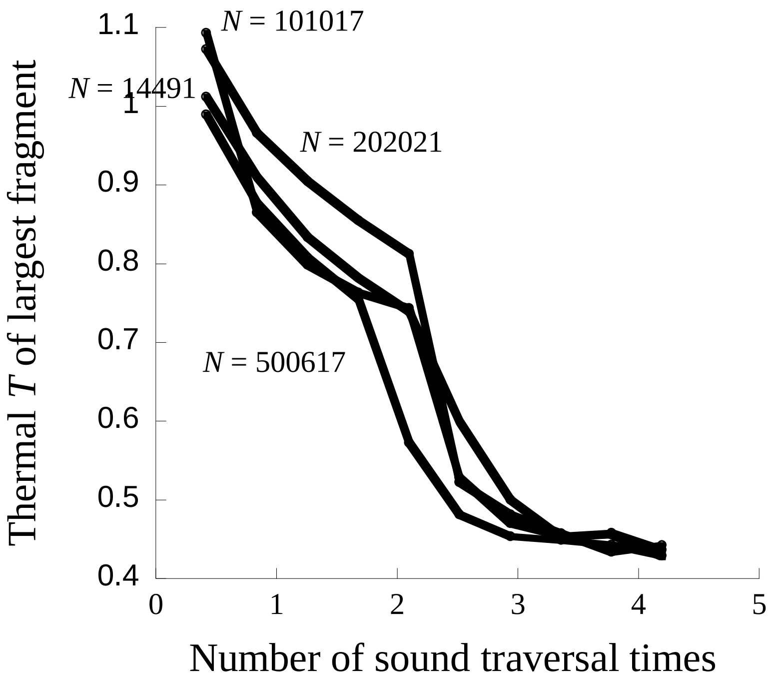

Figure 5.15. Thermal temperature of the largest fragment versus expansion time during Blink-Hoover expansion for 14 491, 101 017, 202 021 and 500 617 particles. Initial density and temperature are 0.62 and 1.16, respectively.

In Fig. 5.16 the rotational temperature of the largest cluster is given for the systems with N = 14491, 101 017, 202 021 and 500 617 particles and the initial density and temperature ρ = 0.62 and T = 1.16, respectively. This temperature is negligibly small, as in Blink and Hoover (1985). From the beginning till the half of the expansion time, this temperature strongly depends on N: it decreases with N till N = 202 021 and then it remains constant. Starting from the half of the expansion time, this temperature becomes practically equal for all N.

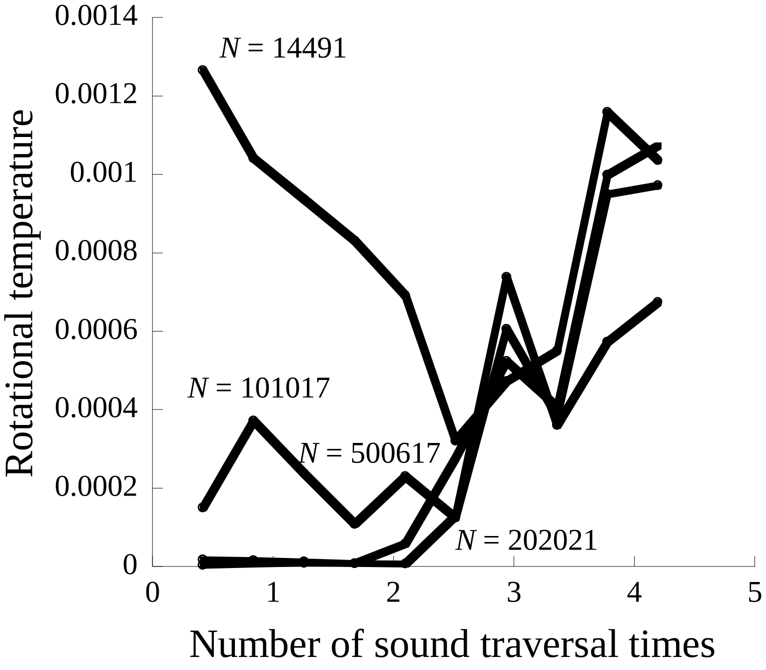

Figure 5.16. Dependence of the rotational temperature of the largest fragment on the expansion time during Blink-Hoover expansion for 14 491, 101 017, 202 021 and 500 617 particles. Initial density and temperature are 0.62 and 1.16, respectively.

In Figs. 5.17 and 5.18 the mean square radius of gyration of the largest cluster, and of an average fragment are given for the systems with N = 14 491, 101 017, 202 021 and 500 617 particles and the initial density and temperature $\rho = 0.62$ and $T = 1.16$, respectively. The former initially is proportional to the system size and becomes independent on it from a half of the expansion time. The latter is practically independent on the system size.

In Figs. 5.19 and 5.20 the shape factor of the largest cluster, and that of an average fragment are given for the same systems and initial conditions. The shape factor of the largest cluster does not differ significantly on the system size during the expansion but it increases with the time and this means that the fragments become more asymmetric. However, that of an average fragment is practically independent on the system size and the expansion time.

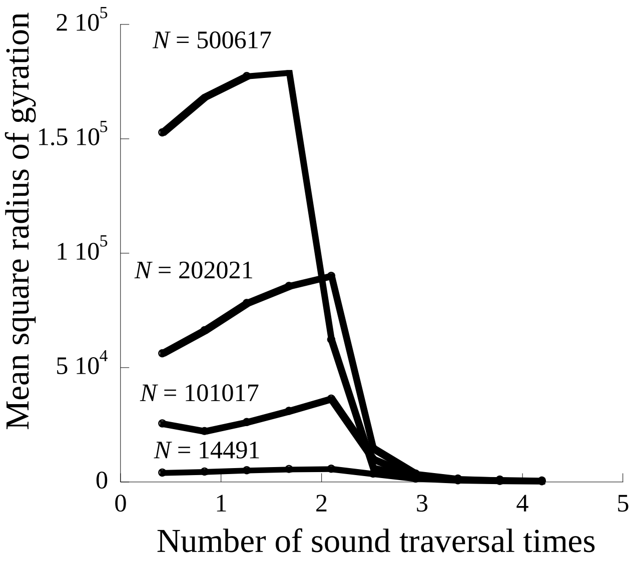

Figure 5.17. Dependence of the mean square radius of gyration of the largest fragment on the expansion time during Blink-Hoover expansion for 14 491, 101 017, 202 021 and 500 617 particles. Initial density and temperature are 0.62 and 1.16, respectively.

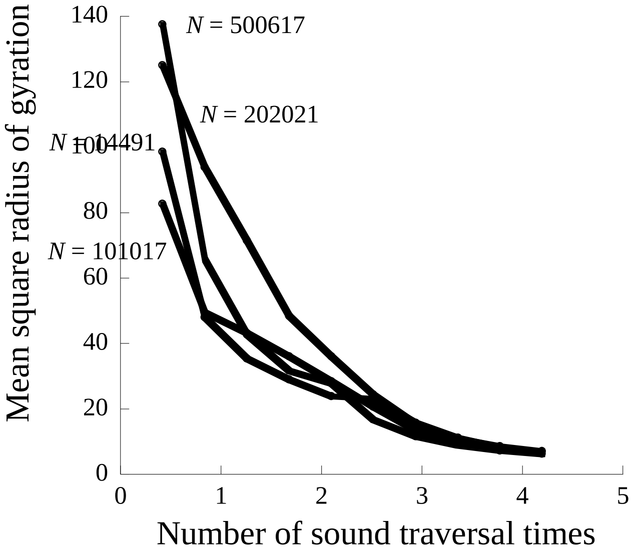

Figure 5.18. Dependence of the mean square radius of gyration of the fragments on the expansion time during Blink-Hoover expansion for 14 491, 101 017, 202 021 and 500 617 particles. Initial density and temperature are 0.62 and 1.16, respectively.

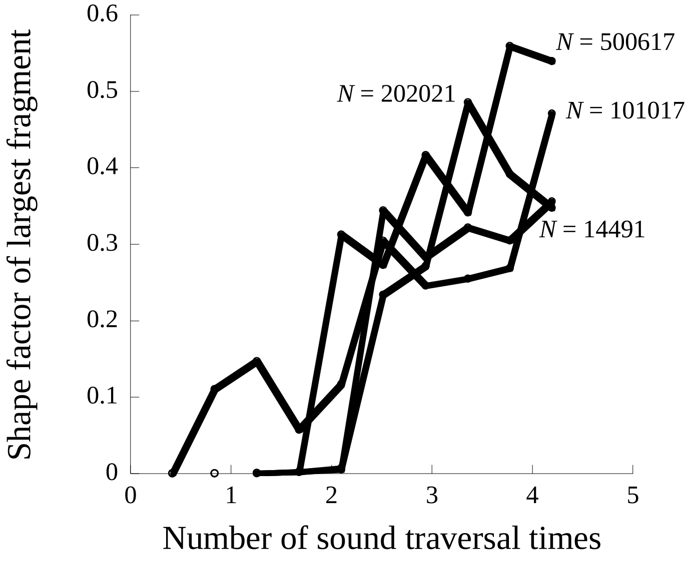

Figure 5.19. Dependence of the shape factor of the largest fragment on the expansion time during Blink-Hoover expansion for 14 491, 101 017, 202 021 and 500 617 particles. Initial density and temperature are 0.62 and 1.16, respectively.

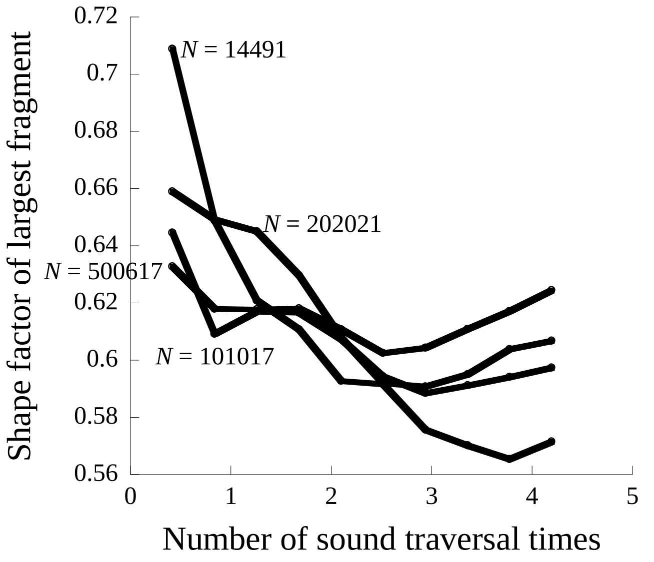

Figure 5.20. Dependence of the shape factor of the fragments on the expansion time during Blink-Hoover expansion for 14 491, 101 017, 202 021 and 500 617 particles. Initial density and temperature are 0.62 and 1.16, respectively.

5.7 Conclusions

In this Chapter simulations by the Hoover-Blink method for the systems from 721 to 500 617 particles are performed. Other researchers used not more that 14 491 particles. We compared two methods to prevent material from crossing an interface: a steep repulsive potential and elastic boundary conditions and found that the latter is much better. For example, the former one produces unphysical cavitation. The latter one is used in our work. Some authors used the repulsion potential, therefore, our results are much more reliable. Blink and Hoover did not report on their method. They used and old equation of state to calculate the pressure but we calculated the pressure exerted at the wall. We also calculated the pressure at the first stage by the virial formula, although it may not be strictly applied because of the absence of periodic boundary conditions, and showed that it produced reasonable results. Nevertheless, it produced reasonable results. We averaged our result over 10 realisations while our predecessors used not more than 3, we showed that it is far not enough and, therefore, our results are much more reliable. In our studies, an effective Reddy and O'Shea equation of state for the two-dimensional Lennard-Jones fluid which is much better that the equations of state used by the previous authors. It is shown that the fragmentation mechanism is mechanical fracture, not spinodal decomposition. Four simple models of fragmentation were tested. They predict dependence of the fragment maximum size on the pressure and the number of particles in the system. Our results for the dependence on the size for ρ = 0.62 and T = 1.16 disagree with all four models, they are in the middle between the model 3 and models 1 and 2. The results of Blink and Hoover for this density and temperature agree well with the model 3. It is necessary to say that their systems had different initial pressures and temperatures and they adjusted their data to the same starting conditions. This leads to an error and our results are more exact. One must notice that Hoover used only two or three points for interpolation but we used many points. However, for ρ = 0.65 and T = 0.65 our results are close to the model 3.

The dependence on the pressure is examined for systems with up to 14 491 particles. The scaling exponent decreases with the system size and tends to that predicted by the model 3. For 14 491 particles the agreement is beautiful but simulations for larger systems are necessary to confirm the result. An interesting result is obtained: generally, the higher is the pressure – the smaller are the largest fragment sizes. It can be explained taking into account the fact that entropy of the system increases with the pressure. Simulations with the Blink-Hoover method with the LJ-spline potential are performed for a state point in common with Blink and Hoover. The equilibrium pressures and the final thermal temperatures of the fragments obtained with this potential are almost always the same as those of the traditional Blink-Hoover routine. The dependence of the largest fragment size on the pressure for this potential is close to that of the models 1 and 4.

In these simulations, the number of fragments is proportional to the system size. The largest fragment size is proportional to the system size during the first half of the expansion, but at the end of expansion it does not depend on that size. Another interesting result is: the translational temperature of fragments decreases with the expansion, however, that of the largest cluster increases. The latter is zero initially till 0.5 – 2 sound traversal times. This temperature increases with the size till N = 100 000, then the saturation occurs. Both temperatures are approximately equal at the end of expansion. The thermal temperature of fragments initially decreases, then increases, and then again decreases. That temperature of the largest fragment always decreases. The final thermal temperature of the largest fragment is about 0.4 for all system sizes and reaches this value after 4 sound traversal times, in agreement with the result of Blink and Hoover for much smaller systems. The final thermal temperature of the other fragment is about 0.22 for all system sizes. The rotational temperature is small as expected. Till the half of the expansion time this temperature strongly depends on N: it decreases with N and then it becomes practically equal for all N. The mean square radius of gyration of the largest cluster becomes independent on the system size from a half of the expansion time. This factor for an average fragment is practically independent on the system size, which is an interesting result. The relative shape anisotropy increases with the expansion and does not depend significantly on the system size. This means that the fragments become more asymmetric for all systems. However, it is interesting to note the anisotropy of an average fragment is practically independent on the system size and the expansion time.

Chapter 6

Results, Conclusions and Recommendations for Future Work

In this work, the binodal of the two-dimensional LJ-spline fluid is obtained. Nobody succeeded to obtain it earlier. Due to very large uncertainties, presence of the solid phase at $T < 0.4$ and instability in the simulations of this liquid, only the top of this curve ($T > 0.4$) is more or less reliable. Two points on the liquid - solid branches of the phase diagram of this fluid were obtained for $T = 0.7$ and 1.0, and the curves were extrapolated along them. This is also a new and interesting result because nobody tried to obtain them earlier.

We also calculated the 2nd and 3rd virial coefficient for the two-dimensional LJ-spline fluid. It was not done earlier. The pressure of the two-dimensional LJ-spline fluid obtained with the virial coefficients is compared with that obtained from MD simulation for $T = 0.7$ and 1.2. There is a good agreement till $\rho \approx 0.2 – 0.3$.

We performed expansions by the Holian-Grady method for the systems from 1089 to 541 696 particles. Our predecessors used not more that 4225 particles. We averaged our result over 10 realisations while our predecessors used not more than 5, and therefore, our results are much more reliable. In these expansions, the relative shape anisotropy of the fragments is calculated in the course of expansion. It is found that it does not depend on the system size and in general increases with the expansion rate. Its dependence on the rate and on the time is small but becomes large for the high rates. At the rate 0.856 that dependence exhibits a peak. About 15% of the fragments are almost round during the expansion. Thermal temperature of fragments in the laboratory frame has been calculated. It exhibits a peak at the initial stage of the expansion and then decreases. It grows proportionally to square root of the system size. It is shown that the thermal temperature of fragments in the expanding system frame does not depend on the time, expansion rate and the system size. We showed that the results of the simulations depend noticeably on the number of realisations (initial configurations of the system). It is investigated how the fragmentation depends on the initial temperature and pressure of the system. It is found that fragmentation depends rather weak on the initial temperature, but stronger on the initial density. The aim of the future work is to analyse the fragmentation patterns quantitatively with the radial distribution functions $g(r)$ and the structure factor $S(q)$.

An interesting result has been obtained: the average fragment size in the expansion by the Holian-Grady method depends weakly on the system size. One can even notice a trend: that size decreases slowly with the system size. It agrees with Grady's model of fragmentation. The dependence of that size on the expansion rate also agrees well with the Grady's model: the scaling exponent does not depend on the system size and equals –1.22 (the Grady's model predicts −4/3). However, for the LJ potential with the cutoff 2.5, the scaling exponent equals 0.78. Another interesting result is that the maximum fragment size does not depend much on the system size. According to the Grady's model, the largest fragment size in a two-dimensional system is proportional to the inverse expansion rate. Our simulations confirm that very well.

We have found out what phases on the phase diagram of LJ-spline fluid correspond to the density and temperature of the expanding system, and how they differ from the expanding system. We have come to conclusion that a phase transition liquid – vapour occurs during the expansion by spinodal decomposition and by hydrodynamic fracture. Quenching into unstable region of the phase diagram happens during the expansion and spinodal decomposition occurs. Then a break up into clusters happens.

We performed simulations by the Hoover-Blink method for the systems from 721 to 500 617 particles. Our predecessors used not more that 14 491 particles. We averaged our result over 10 realisations while our predecessors used not more than 3, hence our results are much more reliable. In fragmentation studies, an equation of state is of big importance since one can compute all relevant thermodynamics and determine the phase diagram. We applied a progressive Reddy and O'Shea equation of state for the two-dimensional Lennard-Jones fluid which is much better that the equations of state used by the previous authors. It is shown that the fragmentation mechanism is hydrodynamic fracture, not spinodal decomposition. Four simple models of fragmentation were tested. They predict dependence of the fragment maximum size on the pressure and the number of particles in the system. Our results for the dependence on the size for $\rho = 0.62$ and $T = 1.16$ disagree with all four models; they are in the middle between the model 3 and models 1 and 2, namely, we got the power of N equal to 0.33, the model 3 predicts this power to be 0.7, and the models 1 and 2 predict it to be 0 and 1, respectively. The results of Blink and Hoover for this density and temperature agree well with the model 3. However, for $\rho = 0.65$ and $T = 0.65$ our results are close to the model 3.

The dependence on the pressure is examined for systems with up to 14 491 particles. The scaling exponent decreases with the system size and tends to that predicted by the model 3 (Table 5.6). For 14 491 particles the agreement is very good. An interesting result is obtained: generally, the higher is the pressure – the smaller are the largest fragment sizes. Simulations with the Blink-Hoover method with the LJ-spline potential are performed for a state point in common with Blink and Hoover. The equilibrium pressures and the final thermal temperatures of the fragments obtained by this method are almost always the same as those of the traditional Blink-Hoover routine. The dependence of the largest fragment size on the pressure is close to that of the models 1 and 4.

In these simulations, the number of fragments is proportional to the system size. The largest fragment size is proportional to the system size during the first half of the expansion, but at the end of expansion it does not depend on that size. Another interesting result is: the translational temperature of fragments decreases with the expansion, however, that of the largest cluster increases. The latter is zero initially till 0.5 – 2 sound traversal times. This temperature increases with the size till $N = 100\ 000$, then the saturation occurs. The thermal temperature of fragments initially decreases, then increases, and then again decreases. That temperature of the largest fragment always decreases. It is interesting that the former temperature depends on the system size non-monotonically. The final thermal temperature of the largest fragment is about 0.4 and it reaches this value after 4 sound traversal times, in agreement with the result of Blink and Hoover for much smaller systems. The rotational temperature initially strongly depends on the system size: it decreases with the system size and then it becomes practically equal for all system sizes. The relative shape anisotropy increases with the expansion and does not depend much on the system size. This means that the fragments become more asymmetric for all systems.

The future work is to obtain the binodal of the two-dimensional LJ-spline fluid with a higher accuracy, (may be, with the histogram reweighting method) and to obtain many points on the liquid – solid branch of the phase diagram. It is necessary to calculate the 4th coefficient of this fluid. Nobody has calculated this coefficient earlier for this fluid and it is of interest to see what parts of the phase diagram can be described using it. It is important to perform many simulations for large systems and different potentials, and for different starting conditions. It is essential to revise and develop the existing simple models of fragmentation, for that reason a lot of theoretical work must be carried out.

References

Abraham, F. F., 1980, “Melting in 2 Dimensions Is 1st Order - Isothermal-Isobaric Monte-Carlo Study”, Physical Review Letters, 44, 463-466

Abraham, F. F., 1986, “Computational Statistical Mechanics. Methodology, Applications and Supercomputing”, Advances in Physics, 35, 1-111

Allen, M. P. and Tildesley, D. J., 1987 “Computer Simulation of Liquids”, Clarendon Press, Oxford

Ashurst, W. T. and Holian, B. L., 1999a, “Droplet Formation by Rapid expansion of a Liquid”, Physical Review E, 59, 6742-6752

Ashurst, W. T. and Holian, B. L., 1999b, “Droplet Size Dependence upon Volume Expansion Rate”, Journal of Chemical Physics, 111, 2842-2843

Barker, J. A. and Henderson, D., 1967, “Perturbation Theory and Equation of State for Fluids. 2. A Successful Theory of Liquids”, Journal of Chemical Physics, 47, 4714-4721

Barker, J. A., Henderson, D. and Abraham, F. F., 1981, “Phase Diagram of the Two-Dimensional Lennard-Jones System; Evidence for First-Order Transitions”, Physica A, 106, 226-238

Berendsen, H.J.C., Postma, J.P.M., van Gunsteren, W. F., DiNola A. and Haak, J. R., 1984, “Molecular Dynamics with Coupling to an External Bath”, Journal of Chemical Physics, 81, 3684-3690

Binder, K., Sengupta, S. and Nielaba, P., 2002, “The Liquid–Solid Transition of Hard Discs: First-Order Transition or Kosterlitz–Thouless–Halperin–Nelson–Young Scenario?”, Journal of Physics: Condensed Matter, 14, 2323-2333

Blink, J., “Fragmentation of Suddenly Heated Liquids”, 1985, PhD thesis. University of California, Davis

Blink, J. A. and Hoover, W. G., 1985, “Fragmentation of Suddenly Heated Liquids”, Physical Review A, 32, No 2, 1027-1035

Braga, C. and Travis, K.P., 2005, “A Configurational Temperature Nose-Hoover Thermostat”, Journal of Chemical Physics, 123, 134101

Brown, W.K., Karpp, R.R. and Grady, D.E., 1983, “Fragmentation of the Universe”, Astrophysics and Space Science, 94, 401-412

Butler, B. D., Ayton, G., Jepps, O. G. and Evans, D. J., 1998, “Configurational Temperature: Verification of Monte Carlo Simulations”, Journal of Chemical Physics, 109, No 16, 6519 – 6522

Chen, B., Siepmann, J. I. and Klein, M. L., 2001, “Direct Gibbs Ensemble Monte Carlo Simulations for Solid-Vapor Phase Equilibria: Applications to Lennard-Jonesium and Carbon Dioxide”, Journal of Physical Chemistry B, 105, 9840-9848

Debenedetti, P. G., 1996, “Metastable Liquids: Concepts and Principles”, Princeton University Press

Delhommelle, J. and Evans, D. J., 2001, “Configurational Temperature Profile in Confined Fluids. II. Molecular fluids”, Journal of Chemical Physics, 114, No 14, 6236-6241

Elek, P. and Jaramaz, S., 2008, “Fragment Size Distribution in Dynamic Fragmentation: geometric Probability Approach”, FME Transactions, 36, 59-65

Ellerby, H. M., Weakliem, C. L. and Reiss, H., 1991, “Journal of Chemical Physics”, 95, 9209-9218

Eppenga, R. and Frenkel, D., 1984, “Monte Carlo Study of the Isotropic and Nematic Phases of Infinitely Thin Hard Platelets”, Molecular Physics, 52, 1303- 334

Escobedo, F.A., 2000, “Simulation and Extrapolation of Coexistence Properties with Single-Phase and Two-Phase Ensembles”, Journal of Chemical Physics, 113, 8444–8456

Evans, D. J., 1983, “Computer Experiment for Nonlinear Thermodynamics of Couette Flow”, Journal of Chemical Physics, 78, 3297-3302

Evans, D. J., Hoover, W. G., Failor, B. H., Moran, B. and Ladd, A. J. C., 1983, Nonequilibrium Molecular Dynamics Via Gauss's Principle of Least Constraint”, Physical Review A, 28, 1016-1021

Fehder, P., 1969, “Molecular Dynamics Studies of Microscopic Properties of Dense Fluids”, Journal of Chemical Physics, 50, 2617-2629

Frenkel, D., 1999, “Entropy-Driven Phase Transitions”, Physica A, 263, 26-38

Frenkel, D. and McTague, J. P., 1979, "Evidence for an Orientationally Ordered 2-Dimensional Fluid Phase from Molecular-Dynamics Calculations", Physical Review Letters, 42, 1632-1635

Frenkel, D. and Ladd, A. J. C., 1984, "New Monte Carlo Method to Compute the Free Energy of Arbitrary Solids. Application to the FCC and HCP Phases of Hard Spheres", Journal of Chemical Physics, 81, 3188-3193

Frenkel, D. and Smit, B. 2002, "Understanding Molecular Simulation: from Algorithms to Applications", Academic Press, San Diego, London

Gasser, U., Eisenmann, C., Maret, G. and Keim P., 2010, "Melting of Crystals in Two Dimensions", ChemPhysChem, 11, 963-970

Gelb, L.D. and Muller E.A., 2002, " Location of Phase Equilibria by Temperature-Quench Molecular Dynamics Simulations", Fluid Phase Equilibria, 203, 1-14

Gladden, J.R., Handzy, N.Z., Belmonte, A. and Villermaux, E., 2005, "Dynamic Buckling and Fragmentation in Brittle Rods", Phys. Rev. Lett., 94, 35503

Glenn, L.A. and Chudnovsky, A., 1986, "Strain-Energy Effects on Dynamic Fragmentation", J. Appl. Phys., 59, 1379-1380

Glenn, L.A., Gommerstadt, B.Y. and Chudnovsky, A., 1986, "A Fracture Mechanics Model of Fragmentation", J. Appl. Phys., 60, 1224-1226

Gold, V.M. and Baker, E.L., 2008, "A Model for Fracture of Explosively Driven Metal Shells", Engineering Fracture Mechanics 75, 275-289

Grady, D.E., 1982, "Local Inertial Effects in Dynamic Fragmentation", Journal of Applied Physics, 53, 322-325

Grady, D., 1990, "Particle Size Statistics in Dynamic Fragmentation", J. Appl. Phys., 68, 6099-6105

Grady, D.E., 2008, "Fragment Size Distributions from the Dynamic Fragmentation of Brittle Solids", International Journal of Impact Engineering, 35, 1557-1562

Grady, D.E. and Kipp, M.E., 1980, "Continuum Modelling of Explosive Fracture in Oil Shale", International Journal of Rock Mechanics and Mining Sciences, 147-157

Grady, D.E. and Kipp, M.E., 1985, “Geometric Statistics and Dynamic Fragmentaton”, J. Appl. Phys., 58, 1210-1222

Grady, D.E. and Kipp, M.E., 1987, “Dynamic Rock Fragmentation”, in “Fracture Mechanics of Rock”, Academic Press, London

Griffith, A.A., 1921, "The Phenomena of Rupture and Flow in Solids", Phil. Trans. Royal Soc. London, A 221, 163-198.

Griffiths, D.V. and Smith, I.M., 1991, “Numerical Methods for Engineers: a Programming Approach”, Blackwell Scientific, Oxford, pp. 315-316

Guicheret-Retel, V., Trivaudey, F., Boubakar, M.L. and Thevenin, P., 2004, “Elastic and Viscoplastic Pellets fragmentation Modeling Using an Axisymmetrical 1D Finite Element Code”, Nuclear Engineering and Design, 232, 249-262

Hagen, M.H.J., Meijer, E.J., Mooij, G.C.A.M., Frenkel, D. and Lekkerkerker, H.N.W., 1993, “Does C-60 Have a Liquid Phase?”, Nature, 365, 425-426

Halperin, B.I. and Nelson, D.R., 1978, “Theory of Two-Dimensional Melting”, Physical Review Letters, 41, 121-124

Hansen, J.-P. and Verlet, L., 1969, “Phase Transitions of Lennard-Jones System”, Physical Review, 184, 151-161

Harris, J.G. and Yung, K.H., 1995, “Carbon Dioxides Liquid-Vapor Coexistence Curve and Critical Properties as Predicted by a Simple Molecular-Model”, Journal of Physical Chemistry, 99, 12021-12024

Henderson, D. and Barker J. A., 1968, “On Solidification of Argon”, Molecular Physics, 14, 587

Henderson, D., 1977, “Monte-Carlo and Perturbation-Theory Studies of Equation of State of 2-Dimensional Lennard-Jones Fluid”, Molecular Physics, 34, No 2, 301-315

Herrmann, H.J., 1995, “Some New Results on Fracture”, Physica A, 221, 125-133

Higley, M. and Belmonte, A., 2008, “Fragment Distribution for Brittle Rods with Patterned Breaking Probabilities”, Physica A 387, 6897-6912

Holian, B. L. and Grady, D. E., 1988, “Fragmentation by Molecular Dynamics: The Microscopic “Big Bang”. Physical Review Letters, 60, No 14, 1355-1358

Holian, B. L., 2009, Private communication

Hoover, W. G., 1985, “Canonical Dynamics: Equilibrium Phase-Space Distributions”, 31, 1695-1697

Hoover, W. G., 1986, “Constant-Pressure Equations of Motion”, Physical Review A, 34, 2499-2500

Hoover, W. G., 1991, “Computational Statistical Mechanics”, Elsevier, Essex, UK, 1991, 313 p.

Hoover, W. G. 2006 “Smooth Particle Applied Mechanics”, World Scientific, Singapore, 300 p.

Hoover, W. G. and Ree, F. H., 1967, “Use of Computer Experiments to Locate Melting Transition and Calculate Entropy in Solid Phase”, Journal of Chemical Physics, 47, 4873-4878

Hoover, W. G., Gray, S. C. and Johnson, K., 1971, “Thermodynamic Properties of the Fluid and Solid Phases for Inverse Power Potentials”, Journal of Chemical Physics, 55, 1128-1136

Hoover, W. G., Ladd, A. J. C. and Moran, B., 1982, “High Strain Rate Plastic Flow Studied Via Nonequilibrium Molecular Dynamics”, Physical Review Letters, 48, 1818-1820

Jiang, S. and Gubbins, K. E., 1995, “Vapor-Liquid-Equilibria in 2-Dimensional Lennard-Jones Fluids − Unperturbed and Substrate-Mediated Films”, Molecular Physics, 86, 599-612

Kipp, M.E. and Grady, D.E., 1985, “Dynamic Fracture Growth and Interaction in One Dimension”, Journal of Mechanics and Physics of Solids, 33, 399-415

Kofke, D A., 1993, “Gibbs-Duhem Integration - A New Method for Direct Evaluation of Phase Coexistence by Molecular Simulation”, Molecular Physics, 78, 1331-1336. a

Kofke. D A., 1993, “Direct Evaluation of Phase Coexistence by Molecular Simulation Via Integration Along the Saturation Line”, Journal of Chemical Physics**,** 98, 4149-4162. b

Kosterlitz, J.M. and Thouless, D.J., 1972, “Long Range Order and Metastability in Two–Dimensional Solids and Superfluids”, Journal of Physics C, 5, L124

Kosterlitz, J.M. and Thouless, D.J., 1973, “Ordering Metastability, and Phase Transitions in Two–Dimensional Systems”, Journal of Physics C, 6, 1181-1203

Kosterlitz, J.M., 1974, “The critical properties of the two-dimensional XY model”, Journal of Physics C, 7, 1046-1060

Ladd, A.J.C. and Woodcock, L-V., 1977, “Triple-Point Coexistence Properties of the Lennard-Jones System”, Chemical Physics Letters, 51, 155-159

Ladd, A.J.C. and Woodcock, L-V., 1978, “Interfacial and Coexistence Properties of Lennard-Jones System at Triple Point”, Molecular Physics, 36, 611-619

Landau, L. D., Lifshitz, E. M., 1960, “Mechanics, Course of Theoretical Physics”, Vol.1, Pergamon Press, Oxford

Landau, L. D., 1981, “Statistical Physics”, Pergamon Press, Oxford

Lankford, J. and Blanchard C.R., 1991, “Fragmentation of Brittle Materials at High Rates of Loading”, Journal of Material Science, 26, 3067-3072

Lee, J. K., Barker, J. A. and Abraham, F. F., 1973, “Theory and Monte Carlo Simulation of Physical Clusters in the Imperfect Vapor”, Journal of Chemical Physics, 58, 3166-3180

Lekkerkerker, H. N. W., Poon, W. C-K., Pusey, P. N., Stroobants, A. and Warren, P.B., 1992,

“Phase-Behavior of Colloid Plus Polymer Mixtures”, Europhysics Letters, 20, 559-564

Lienau, C. C., 1936, “Random Fracture of a Brittle Solid”, J. Franklin Inst., 221, 485-494

Lisal, M. and Vacek, V., 1996, “Direct Evaluation of Vapour-Liquid Using Gibbs-Duhem Integration Equilibria by Molecular Dynamics”, Molecular Simulation, 17, 21-39

Mock, W., Jr. and Holt, W. H., 1983, “Fragmentation Behavior of Armco Iron and HF-1-Steel Explosive-Filled Cylinders”, Journal of Applied Physics, 54, 2344-2351

Mott, N.F. and Linfoot, E.H, 1943, “A Theory of Fragmentation”, British Ministry of Supply Report, AC 3348

Mott, N.F., 1947, “Fragmentation of Shell Cases”, Proc. Roy. Soc. A, London, 189, 300-308

Nelson, D.R. and Kosterlitz, J.M., 1977, “Universal Jump in the Superfluid Density of Two-Dimensional Superfluids”, Physical Review Letters, 39, 1201-1205

Nelson, D.R. and Halperin B.I., 1979, “Dislocation-mediated melting in two dimensions”, Physical Review B, 19, 2457-2484

Nicolas, J. J., Gubbins, K. E., Streett, W. B. and Tildesley, D. J., 1979, “Equation of State for the Lennard-Jones Fluid”, Molecular Physics, 37, No 5, 1429-1454

Panagiotopoulos, A. Z., 1987, “Direct Determination of Phase Coexistence Properties of Fluids by Monte-Carlo Simulation in a New Ensemble” Molecular Physics, 61, 813-826

Panagiotopoulos, A. Z., 1994, “Molecular Simulation of Phase Coexistence - Finite-Size Effects and Determination of Critical Parameters for 2-Dimensional and 3-Dimensional Lennard-Jones Fluids”, International Journal of Thermophysics, 15, 1057-1072

Panagiotopoulos, A.Z., 2000, “Monte Carlo Methods for Phase Equilibria of Fluids”, Journal of Physics: Condensed Matter, 12, R25–R52

Panagiotopoulos, A. Z., Quirke, N., Stapleton, M. and Tildesley, D. J., 1988, “Phase-Equilibria by Simulation in the Gibbs Ensemble - Alternative Derivation, Generalization and Application to Mixture and Membrane Equilibria”, Molecular Physics, 63, 527-545

Phillips, J. M., Bruch, L. W. and Murphy, R. D., 1981, “The Two-Dimensional Lennard-Jones System - Sublimation, Vaporization, and Melting”, Journal of Chemical Physics, 75, 5097-5109

Potoff, J. J. and Panagiotopoulos, A. Z., 1998, “Critical Point and Phase Behavior of the Pure Fluid and a Lennard-Jones Mixture”, Journal of Chemical Physics, 109, 10914-10920

Ramakrishnan, T. V., 1982, “Density-Wave Theory of First-Order Freezing in Two Dimensions”, Physical Review Letters, 58, 541-545

Ree, F. H. and Holt, A. C., 1973, “Thermodynamic Properties of the Alkali-Halide Crystals”, Physical Review B, 8, 826 - 842

Reid, R. C., Prausnitz, J. M. and Sherwood, T. K. 1977 “The Properties of Gases and Liquids”, 3rd ed., McGraw-Hill Book Company, New York, NY

Reddy, M. R. and O’Shea, F., 1986, “The Equation of State of the Two-Dimensional Lennard-Jones Liquid”, Canadian Journal of Physics, 64, No 6, 677-684

Reitz, R. D. and Bracco, F. V., 1982, “Mechanism of Atomization of a Liquid Jet”, The Physics of Fluids, 25, 1730-1742

Rovere, M., Nielaba, P. and Binder, K., 1993, “Simulation Studies of Gas-Liquid Transitions in 2 Dimensions Via a Subsystem-Block-Density Distribution Analysis”, Zeitschrift fur Physik B-Condensed Matter, 90, 215-228

Rowlinson, J. S. 1959 “Liquids and Liquid Mixtures”, Butterworths Scientific Publications, London

Schulz, H., Kämpfer, B., Barz, H. W., Röpke, G., and Bondorf, J., 1984, “On the Time-Development of the Liquid-Vapor Phase Transition in an Expanding Nuclear System”, Physics Letters B, 147, 17-22

Senger, B., Schaaf, P., Corti, D. S., Bowles, R., Voegel J.-C., Reiss, H., 1999, Journal of Chemical Physics, 110, 6421-6437

Shih, C.J., Meyers, M.A., Nesterenko, V.F. and Chen, S.J., 2000, “Damage Evolution in Dynamic Deformation of Silicon Carbide”, Acta Materialia, 48, 2399-2420

Shreve, A.P., Walton, J.P.R.B. and Gubbins, K.E., 1986, “Liquid-Drops of Polar-Molecules”, Journal of Chemical Physics, 85, 2178-2186

Silva Fernandes, F.M.S., Fartaria, R.P.S., Freitas, F.F.M., 2001, “The Starting State in Simulations of the Fluid–Solid Coexistence by Gibbs–Duhem Integration”, Computer Physics Communications, 141, 403–411

Singh, R. R., Pitzer, K. S., de Pablo, J. J. and Prausnitz, J. M., 1990, “Monte Carlo Simulation of Phase Equilibria for the Two-Dimensional LennardJones Fluid in the Gibbs Ensemble”, Journal of Chemical Physics, 1990, 92, 5463-5466

Smit, B. and Frenkel, D., 1991, “Equilibria in a Two-Dimensional Lennard-Jones Fluid(s)”, Journal of Chemical Physics, 94, 5663-5668

Sotolongo-Costa, O., Moreno-Vega, Y., Lloveras-González, J. J. and Antoranz J. C., 1996, “Criticality in Droplet Fragmentation”, Physical Review Letters, 76, 42-45

Stepanov, I. A., 1995, “The Scale Effect Is a Consequence of the Cellular Structure of Solid Bodies. Thermofluctuation Nature of Spread in the Values of Strength”, Materials Science, 31, 441-447

Stillinger, F. H., 1963, “Rigorous Basis of the Frenkel-Band Theory of Association Equilibrium”, Journal of Chemical Physics, 38, 1486-1494

Strandburg, K. J., 1988, “Two-Dimensional Melting”, Reviews of Modern Physics, 60, 161- 207.

Tejero, C.F., Daanoun, A., Lekkerkerker, H.N.W. and Baus, M., 1994, “Phase-Diagrams of Simple Fluids with Extreme Pair Potentials”, Physical Review Letters, 1994, 73, 752-758

Thompson, S.M., Gubbins, K.E., Walton, J.P.R.B., et al., 1984, “A Molecular-Dynamics Study of Liquid-Drops”, Journal of Chemical Physics, 81, 530-542

Tipton, R.E., 1991, “CALE Users Manual, Version 910201”, Lawrence Livermore National Laboratory

Todd, B. D., Evans, D. J. and Daivis, P. J., 1995, “Pressure Tensor for Inhomogeneous Fluids”, Physical Review E, 52, 1627-1638

Toxvaerd, S., 1980, “Phase-Transitions in a Two-Dimensional System”, Physical Review Letters, 44, 1002-1004

Toxvaerd, S., 1981, “Computer-Simulation of Melting in a Two-Dimensional Lennard-Jones System”, Physical Review A, 24, 2735-2742

Toxvaerd, S., 1998, “Fragmentation of Fluids by Molecular Dynamics”, Physical Review E, 58, 704-712

Travis, K., 2009, private communication

Udink, C. and Frenkel, D., 1987, “Orientational Order and Solid-Liquid Coexistence in the Two-Dimensional Lennard-Jones System”, Physical Review B, 35, 6933-6939

Vanswol, F., Woodcock, L. V. and Cape, J. N., 1980, “Melting in 2 Dimensions − Determination of Phase-Transition Boundaries”, Journal of Chemical Physics, 73, 913-922

Verlet, L., 1967, "Computer Experiments on Classical Fluids. I. Thermodynamical Properties of Lennard-Jones Molecules", Physical Review, 159, 98-103

Vicentini, A., Jacucci, G. and Pandharipande, V. R., 1985, “Fragmentation of Hot Classical Drops”, Physical Review C, 31, 1783-1793

Voller, V.R. and Cross, M., 1981, “Accurate Solutions of Moving Boundary-Problems Using the Enthalpy Method”, International Journal of Heat and Mass Transfer, 24, 545-556

Wang, H. and Ramesh, K.T., 2004, “Dynamic Strength and Fragmentation of Hotpressed Silicon Carbide under Uniaxial Compression”, Acta Materialia, 52, 355-367

Wedekind, J. and Reguera, D., 2007, “What is the Best Definition of a Liquid Cluster at the Molecular Scale?”, Journal of Chemical Physics, 127, 154516

Wilding, N. B., 1995, “Critical-Point and Coexistence-Curve Properties of the Lennard-Jones Fluid - A Finite-Size-Scaling Study”, Physical Review E, 52, 602-611

Wilding, N. B., 2001, “Computer Simulation of Fluid Phase Transitions”, American Journal of Physics, 69, 1147-1155

ten Wolde, P. R. and Frenkel, D., 1998, “Computer Simulation Study of Gas–Liquid Nucleation in a Lennard-Jones System”, Journal of Chemical Physics, 109, 9901-9918

Young, A.P., 1979, “Melting and the Vector Coulomb Gas in Two Dimensions”, Physical Review B, 19, 1855-1866

Zhang, L., Jin, X. and He, H., 1999, “Prediction of Fragment Number and Size Distribution in Dynamic Fracture”, J. Phys. D., 32, 612-615

Zhou, F., Molinari, J.-F. and Ramesh K.T., 2005, “A Cohesive Model Based Fragmentation Analysis: Effects of Strain Rates and Initial Defects Distribution”, International Journal of Solids and Structures, 42, 5181-5207

Zhou, F., Molinari, J.-F. and Ramesh K.T., 2006a, “Characteristic Fragment Size Distribution in Dynamic Fragmentation”, Appl. Phys. Lett., 88, 261918

Zhou, F., Molinari, J.-F. and Ramesh K.T., 2006b, “Analysis of the Brittle Fragmentation of an Expanding Ring”, Comp. Mater. Sci., 37, 74-85

Appendix 1

The Matlab program for solving the equations for pressures and Helmholtz free energies to determine solid – liquid coexistence curves (Written by I. Stepanov)

The Matlab program is called FSOLVE. It solves systems of nonlinear equations of several variables. The program is started by the command [X, FVAL] = FSOLVE(@MYPROGRAM,X0). Here X0 is the vector of the initial values of the solid and liquid densities. This command tries to solve the equations in MYPROGRAM. MYPROGRAM returns a vector of solutions X and equation values FVAL evaluated at X. FSOLVE implements three different algorithms: trust region dogleg, trust region reflective, and Levenberg-Marquardt. It needs to give the chemical potentials as well as pressures and coexisting densities.

```
function F = myprogram(x)

T = 1.4

% F0 is the reference helmholtz free energy

F0 = 2.6718*T

% B2 is 2nd virial coefficient

B2 = 0.2136

% values a are coeffiecients for solids

a1 = 256.58

a2 = -591.61

a3 = 353.36

% values c are coefficients for fluid

c1 = 2.6284
```

```
c2 = -13.261
c3 = 52.31
c4 = -82.335
c5 = 55.328
% PS is solid pressure
PS = a1*x(1) + a2*x(1)^2 + a3*x(1)^3
%PL is liquid pressure
PL = T*x(2)*(1 + B2*x(2) + c1*x(2)^2 + c2*x(2)^3+ c3*x(2)^4 + c4*x(2)^5 + c5*x(2)^6)
% FS is solid excess energy
FS = F0 + a1*log(x(1)) + a2*(x(1) - 1) + a3*(x(1)^2 - 1)/2 + T*(log(x(1)) - 1)
%FL is liuid excess free energy
FL = T*(B2*x(2) + c1*x(2)^2/2 + c2*x(2)^3/3 + c3*x(2)^4/4 + c4*x(2)^5/5 +c5*x(2)^6/6) +
        T*(log(x(2)) - 1)
PS2 = a1 + a2*x(1) + a3*x(1)^2
PL2 = T*(1 + B2*x(2) + c1*x(2)^2 + c2*x(2)^3 + c3*x(2)^4 + c4*x(2)^5 +c5*x(2)^6)
F = [PS - PL; FS + PS2 - FL - PL2];
End
```

Appendix 2

The parameters of the Reddy equation of state

Table A1

N	C_n	*n*	C_n	*N*	C_n
1	0.7465941518D00	12	-0.4654184040D00	23	0.7948290821D-01
2	0.2170202387D01	13	0.2060578013D02	24	0.8494574507D03
3	-0.3867162453D01	14	0.2778370707D01	25	-0.4038923642D01
4	0.1955514819D00	15	-0.3788766473D03	26	-0.1388504769D04
5	-0.3080792027D00	16	-0.1227538308D03	27	0.1001438224D01
6	0.7254286978D00	17	0.1276939405D03	28	-0.1962817948D02
7	-0.8449806323D00	18	-0.3730636670D03	29	-0.1844924653D02
8	0.1312097237D01	19	0.1354795604D04	30	-0.7164817351D03
9	0.1270817291D00	20	-0.6993741337D-01	31	0.2630515216D02
10	0.2906037677D01	21	-0.4066552651D-01	32	0.4773207984D00
11	-0.6390601256D01	22	0.6531068158D02	γ	0.6682623864D00

Appendix 3

Derivation of the speed of sound

The formula for the adiabatic velocity of sound is (Rowlinson 1959):

$$c^2 = \frac{v}{\mu\beta_S} \tag{A1}$$

Here v is the molar volume, μ is the molecular weight and β_S is the adiabatic bulk compressibility:

$$\beta_S = -\frac{1}{V}\left(\frac{\partial V}{\partial P}\right)_S \tag{A2}$$

where V is the volume, P is the pressure and S is the entropy. Now we derive the ratio of isothermal bulk compressibility $\beta_T = -\frac{1}{V}\left(\frac{\partial V}{\partial P}\right)_T$ to the adiabatic bulk compressibility, β_S. There is a Maxwell relation:

$$\mathrm{d}S = \left(\frac{\partial S}{\partial V}\right)_P \mathrm{d}V + \left(\frac{\partial S}{\partial P}\right)_\mathrm{V} \mathrm{d}P \tag{A3}$$

At constant S, $\left(\frac{\partial S}{\partial V}\right)_P \mathrm{d}V = -\left(\frac{\partial S}{\partial P}\right)_\mathrm{V} \mathrm{d}P$, from which

$$\left(\frac{\partial V}{\partial P}\right)_S = -\frac{(\partial S/\partial P)_V}{(\partial S/\partial V)_P} = -\frac{(\partial S/\partial T)_V(\partial T/\partial P)_V}{(\partial S/\partial T)_P(\partial T/\partial V)_P} = \frac{C_V}{C_P}\left(\frac{\partial V}{\partial P}\right)_T \tag{A4}$$

or

$$\frac{\beta_T}{\beta_S} = \frac{C_P}{C_V} \tag{A5}$$

Here C_P and C_V are the isobaric and isochoric heat capacities, respectively.

In thermodynamics there is a well-known result:

$$C_P - C_V = T\left(\frac{\partial P}{\partial T}\right)_V \left(\frac{\partial V}{\partial T}\right)_P \tag{A6}$$

Introducing Eqs. (A5) and (A6) into Eq. (A1) one obtains

$$\begin{aligned} c^2 &= \frac{v}{\mu}\frac{C_P}{C_V}\frac{1}{\beta_T} = \frac{v}{\mu}\frac{C_V + T(\partial P/\partial T)_V(\partial V/\partial T)_P}{C_V\beta_T} = \\ &-\frac{vV}{\mu}\frac{C_V + T(\partial P/\partial T)_V(\partial V/\partial T)_P}{C_V}\left(\frac{\partial P}{\partial V}\right)_T \end{aligned} \tag{A7}$$

There is a thermodynamic relation (Rowlinson 1959):

$$\left(\frac{\partial V}{\partial P}\right)_T \left(\frac{\partial T}{\partial V}\right)_P \left(\frac{\partial P}{\partial T}\right)_V = -1 \tag{A8}$$

Applying it to Eq. (A7) one obtains

$$c^2 = -\frac{vV}{\mu}\left(\frac{\partial P}{\partial V}\right)_T + \frac{vVT}{\mu C_V}\left(\frac{\partial P}{\partial T}\right)_V^2 \tag{A9}$$

Using the relation

$$\left(\frac{\partial P}{\partial \rho}\right)_T = \left(\frac{\partial P}{\partial (M/V)}\right)_T = -\frac{V^2}{M}\left(\frac{\partial P}{\partial V}\right)_{T,M} \tag{A10}$$

where M is the mass of the system assumed to be constant, $\rho = M/V = \mu/v$ is density, the first term on the right hand side of Eq. (A9) can be written as $\left(\frac{\partial P}{\partial \rho}\right)_T$. In Eq. (A9) C_V is the heat capacity of the system. If to denote the specific capacity by C_v, the second term on the right hand side of Eq. (A9) will look like $\frac{T}{C_v\rho^2}\left(\frac{\partial P}{\partial T}\right)_\rho^2$ and the speed of sound now becomes

$$c^2 = \left(\frac{\partial P}{\partial \rho}\right)_T + \frac{T}{C_v\rho^2}\left(\frac{\partial P}{\partial T}\right)_\rho^2 \tag{A11}$$